Design and Development of New Tactile Softness Displays For Minimally Invasive Surgery

Mohammadreza Ramezanifard

A Thesis

In

The Department

Of

Mechanical and Industrial Engineering

Presented in Partial Fulfillment of the Requirements

For the Degree of Master of Applied Science at

Concordia University

Montreal, Quebec, Canada.

April 2008

Your file Votre référence
ISBN: 978-0-494-40921-3
Our file Notre référence
ISBN: 978-0-494-40921-3

ABSTRACT

Design and Development of New Tactile Softness Displays for Minimally Invasive Surgery

Mohammadreza Ramezanifard

Despite an influential shortcoming of minimally invasive sugary (MIS), which is the lack of tactile feedback to the surgeon, MIS has increasingly been used in various types of surgeries. Restoring the missing tactile feedback, especially information which can be obtained by the palpation of tissue, such as detection of embedded lump and softness characterization is important in MIS. The present study aims to develop tactile feedback systems both graphically and physically.

In graphical rendering approach, the proposed system receives signals from the previously fabricated piezoelectric softness sensors which are integrated with an MIS grasper. After processing the signals, the tactile information is displayed by means of a color coding method. Using the graphical images, the softness of the grasped objects can visually be differentiated.

A physical tactile display system is also designed and fabricated. This system simulates non-linear material properties of different soft objects. The system consists of a linear actuator, force and position sensors and processing software. A PID controller is used to control the motion of a linear actuator according to the properties of the simulated material and applied force.

Graphical method was also examined to render the tactile information of embedded lumps within a soft tissue/object. The necessary information on the size and location of the hidden features are collected using sensorized MIS graspers. The information is then processed and graphically rendered to the surgeon. Using the proposed system surgeons can identify presence, location and approximate size of hidden lumps by grasping the target object with a reasonable accuracy.

Finally, in order to determine the softness of the grasped object, another novel approach is taken by the design and fabrication of a smart endoscopic tool equipped with sensors for measuring the applied force and the angle of the grasper jaws. Using this method, the softness/compliance of the grasped object can be estimated and presented to the surgeon.

ACKNOWLEDGEMENT

While my master's work is supposed to represent an individual contribution, I would not have been able to complete any of it without the support of my colleagues, friends, and family. I owe a large debt of gratitude to all those that have helped me along the way.

First, I would like to thank my advisors, Javad Dargahi and Wenfang Xie. Their easygoing and gentle nature has an amazing ability to inspire their students to work harder than they ever have before and seek their own path. Yet, I could always count on them to provide direction and support whenever I felt lost, stressed, or lacked the confidence to continue.

A very important thanks goes to Saeed, who provided invaluable assistance in developing and completing the experiments needed for my thesis. I could not have asked for a better colleague and friend to work with.

I'd like to thank my friend Madhi Shahrestani, who has been a surrogate family to me.

And last, but certainly not least, I would like to thank my family; my parents. Words simply can not express my gratitude for my family's love and support. They have been with me every step of the way and I could not have done it without them.

Table of Contents

LIST OF FIGURES

LIST OF TABLES

LIST OF ACRONYMS AND SYMBOLS

1-D, 2-D	One Dimensional, Two Dimensional
A/D	Analog to digital
C	Capacitance
DAQ	Data Acquisition system
DC	Direct current
E	Modulus of Elasticity
E1	Young's modulus of object under investigation
E2	Young's modulus of compliant cylinder
F1	Force carried by the inner rigid cylinder
F2	Force carried by the outer compliant cylinder
FSR	Force sensitive resistor
GPa	Gigapascal
Hz	Hertz
IC	Integrated Circuit
MEMS	Micro Electro Mechanical Systems
MIS	Minimal Invasive Surgery
MR	Magnetoresistive
PVDF	Polyvinylidene Fluoride
PVDF-1	PVDF under the inner rigid cylinder
PVDF-2	PVDF under the outer soft cylinder

R	Radius of rigid Cylinder
R1	Inner Radius of Compliant cylinder
R2	Outer Radius of Compliant Cylinder
T1	Thickness of sensed object
T2	Rigid and compliant cylinder height
V	Voltage
V1	Voltage output of PVDF under Inner cylinder
V1	Voltage output of PVDF under the outer cylinder
μm	Micrometer
Ω	Ohms

CHAPTER 1

INTRODUCTION

Humans have a remarkable ability to grasp and manipulate objects with their hands. We sense and interpret tactile stimuli from our environment and perform tasks with our hands in a nearly instinctual manner. The high level of dexterity is achieved through complex sensorimotor mechanisms utilizing visual and tactile information and the physical structure of the hand. Utilizing these abilities, humans can modulate grasp forces, precisely position objects, and detect fine surface features. Consider how easily one can screw in a light bulb. This action requires a delicate grasp to prevent breakage, in addition to careful control over insertion force and position to engage the threads. Humans are also capable of readily dealing with environmental uncertainty or adapting to environmental changes. Despite the obvious importance of tactile cues in our daily lives, the subject of tactile display for teleoperators, virtual reality, and more generally, human/machine interfaces, has only recently received significant attention.

This thesis presents new methods of tactile sensing and display. The goal of this research is to bring the level of tactile sensitivity and acuity that humans possess to telemanipulators and other human/machine interfaces. A new method for measuring local object softness is presented based on a sensorized minimally invasive surgery (MIS) grasper. Such information is indispensable for coordinating finger motions for object manipulation.

Devising a device to display the full sensation of contact continues to attract researchers. Most commonly, researchers present an abstraction of contact geometry and

pressure with a pin array tactile display. These devices recreate a reasonable reproduction of shape at the contact, but their large package size makes them impractical for use outside the laboratory. Rather than presenting the shape of the contact which is not useful in minimally invasive surgery (MIS), a more realistic approach of displaying its softness for MIS is proposed in this thesis. Results of experiments with human subjects demonstrate that it provides them with the cues necessary to ascertain object softness capabilities.

1.1 Motivation

To date, telemanipulation systems have relied heavily on vision feedback and have required experienced operators. It has been shown, however, that adding the sense of touch to these systems connects the operator to the remote environment, making the system more intuitive [1, 2].

Similarly, for virtual reality, when advanced graphics and sound are augmented by force and vibration feedback, one's perception is altered and one becomes immersed in an artificial reality [3].

Last but not the least, is the influence of tactile feedback on minimally invasive surgery. Restoring the missing tactile information, especially the tissue palpation, will be a significant enhancement in MIS capabilities.

1.2 Contributions

The major contributions of this thesis are:

- A new sensor and mathematical framework for measuring local object softness via a force sensing resistor and a potentiometer are presented. The sensorized grasper is tested and its accuracy is determined in experiments.
- A new approach to tactile display based on color coded graphical displaying the softness of objects for telesurgery and MIS operation is developed and tested.
- An algorithm for one and two dimensional localizing and displaying the embedded lumps within the tissue using graphical display is presented.
- A novel electromechanical tactile display for reproducing the softness of objects is developed and tested.

1.3 Thesis outline

This thesis is organized into five chapters. This chapter provides an introduction to and motivation for my research in tactile sensing and display and lists the contributions of this work.

Chapter 2 provides relevant background in human tactile sensing and perception. The physical parameters and role of human mechanoreception are outlined. This chapter also provides an overview of the research works that have been done so far on haptic devices. The performance and effectiveness of these projects are briefly expressed. Specific attention is given to the methods employed in tactile displays.

Chapter 3 introduces an approach for displaying the tactile information gathered from a pre-constructed softness sensor. The graphical tactile display employs the color coding technique in order to display different softness values on the monitor of computer. A prototype incorporating pre-constructed softness sensor into an MIS grasper was fabricated to experimentally validate the designed graphical display. In the second part of

this chapter, the graphical display is changed to adapt to another sensor in order to find and locate the embedded lumps within the soft tissue. Additional background on sensor design is provided in Appendix A.

Chapter 4 reviews the design of current tactile displays and introduces the idea of displaying the material property of a series of elastomers to the users of telemanipulation and virtual reality systems. A prototype that renders the softness was designed and fabricated to verify the approach. Human subject testing was conducted with virtual environments to evaluate the device and the user's relevant perception. Additional details of the device design can be found in Appendix B. An in-depth derivation of the kinematics used in the curvature discrimination experiments can be found in Appendix C.

Chapter 5 presents a softness sensor constructed by modifying an MIS grasper. The force applied by the hand to the grasper and the angle of the grasper tip were measured and plotted. Having the force-angle curve for a material, it was shown that the softness of the grasped material can be determined by defining a criterion. The proposed grasper was tested using different materials and the results showed that the proposed grasper was capable of determining the softness of the grasped object.

Finally, Chapter 6 summarizes the results of this research and suggests future extensions of this work.

CHAPTER 2

BACKGROUND AND RELEVANT WORKS

Touch is one of the five human senses. However, when listing them, touch is usually the last one on the list. It is not surprising given the fact that sight and hearing are usually considered to be more important in our everyday lives. Nevertheless, touch and smell have always been very important to our existence since we have had to distinguish edible substances from those which are harmful and touch has enabled us to use tools with great dexterity. Therefore, from the point-of-view of touch, new applications should be studied and developed. Among those applications is the transmission of the actual sense of touch. Designing hardware in order to transmit the sense of touch to the human hand is a significant challenge. The primary reason is that our hands are extremely sensitive to even the smallest vibrations over a range from 10-100 Hz. To help define the design requirements of such hardware, it is important to understand the fundamentals of tactile sensing mechanisms. This will serve as a source of inspiration for improving tactile sensor designs. In addition, it will help to understand which signals are important to communicate and the extent to which they should be communicated. Although this knowledge is requisite, there is more to consider than simply the neurophysiology of touch. Our sense of touch is, in reality, a combination of tactile and kinesthetic information. The combination of cutaneous and kinesthetic sensing is referred to as haptic perception. At a higher level, it is the perception or interpretation of these signals that ultimately interests us.

2.1 Haptic Sense

Two groups of physiological sensations are involved in the wide meaning of haptic sense. The first is the tactile sense where the receptors are located under the dermis. Tactile sense detects the information from the skin surface such as contact pressure or vibration. Another is the proprioceptive sense where the receptors exist in the muscle or in the tendon.

2.1.1 Tactile Sensing and Human Mechanoreception

The human hand contains a complex array of specialized receptors that are rugged enough to survive repeated impacts, while retaining the ability to detect faint vibrations and the softest touch.

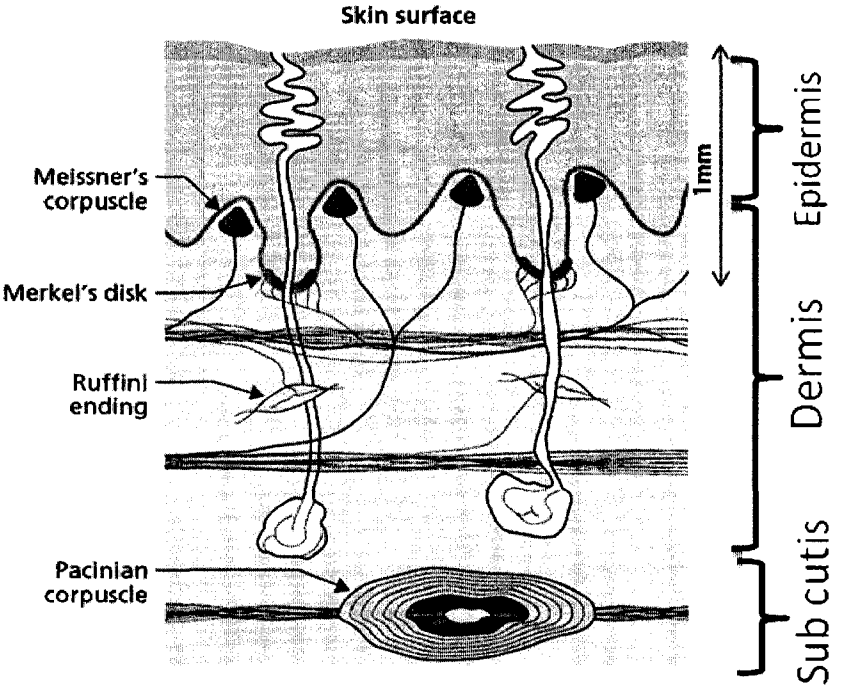

Figure 2.1. Mechanoreceptors [4, 5].

Four main types of tactile mechanoreceptors have been identified [6,7]. Each type is specialized to separate specific feelings such as pressure, shear, vibration, or texture [7]. The sensing element of each of these mechanoreceptors is very similar in that they possess physical packaging and position within the skin that is exclusively adapted to its purpose. Figure 2-1 shows a cross-sectional view of the skin on a human fingertip and the position of specialized touch receptors underneath the skin surface [4, 5]. The distribution of the mechanoreceptors on the palm is shown in Figure 2-2 [8-10].

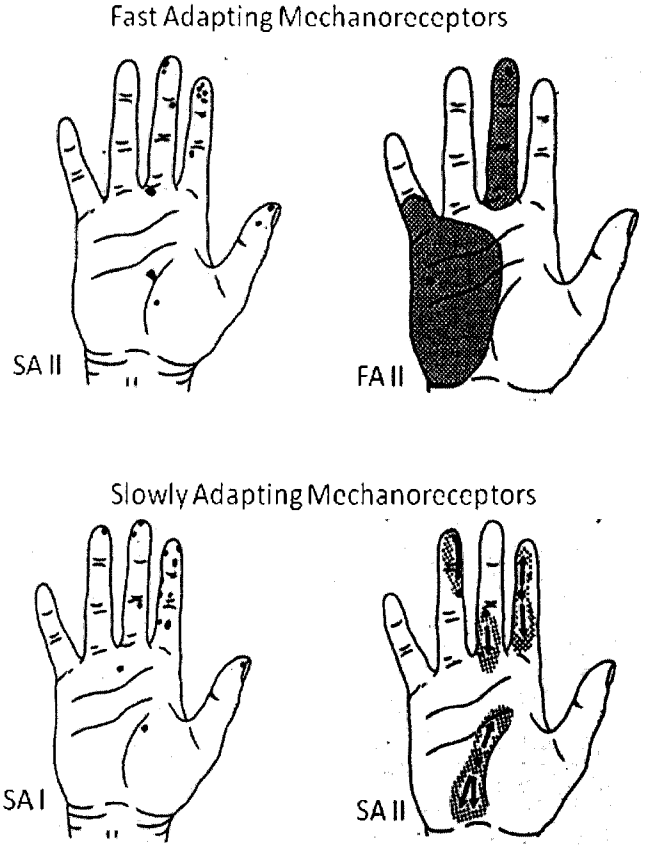

Figure 2-2. Distribution of the Mechanoreceptors.

Mechanoreceptor types are divided into two categories based on their placement beneath the surface of the skin [5, 11]. Type I receptors (Merkel & Meissner) are located

near the surface of the skin between the epidermis and the dermis on the papillary ridges. Type II receptors (Ruffini & Pacinian) are located deeper beneath the skin in the dermis. Receptors that lie deeper beneath the skin have larger receptive fields. Correspondingly, fewer type II receptors are observed per unit area of skin. Receptors are further divided into fast adapting (FA) types and slow adapting (SA) types. FA types do not respond to static stimulus but only to skin indentation while the stimulus is changing. SA types exhibit a sustained discharge while a steady indentation is maintained. These two types are analogous to the difference between piezoelectric and piezoresistive sensing elements, respectively [10, 12]. However, unlike man-made piezoelectric and piezoresistive sensors which provide analog signals, biological mechanoreceptors encode their signals as a series of pulses, as shown in Figure 2-3, which are similar to digital serial communication.

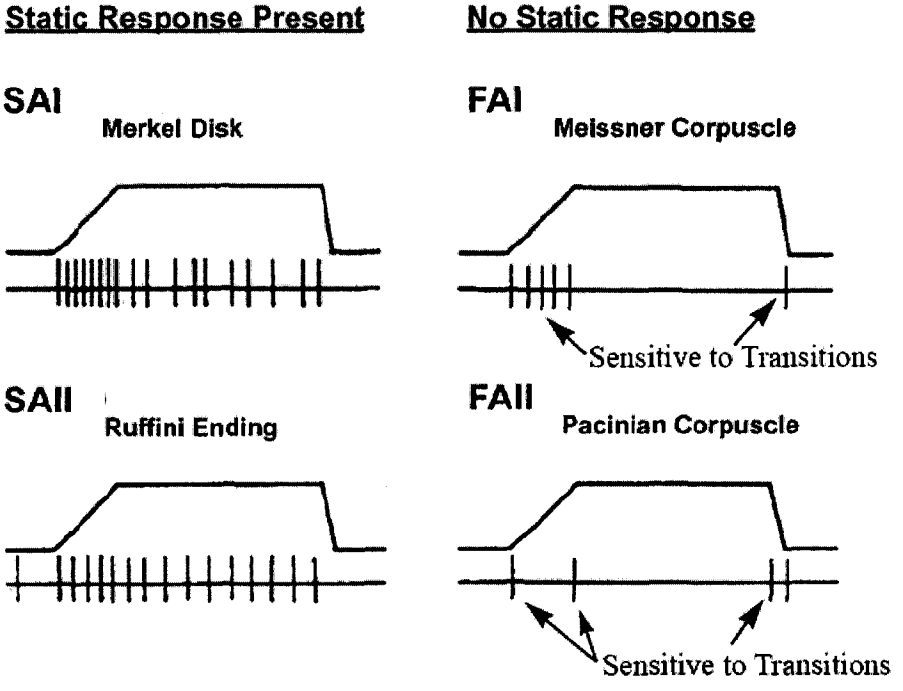

Figure 2-3. Responses of the four types of mechanoreceptors to normal indentation of the skin [5, 9, 10, 12].

Table 2-1 summarizes the characteristics of each mechanoreceptor and the physical parameters they measure [13].

Table 2-1. Characteristics of mechanoreceptors found in human fingertip skin [13].

RECEPTOR	*RECEPTOR* TYPE	*FIELD* DIAMETER	*FREQUENCY* RANGE	*SENSED PARAMETER*
Merkel Disks	*SAI*	*3-4 mm*	*DC-30 Hz*	*Local skin curvature*
Ruffini Endings	*SAII*	*>10 mm*	*DC- 15 Hz*	*Directional Skin Stretch*
Meissner Corpuscles	*FAI*	*3-4 mm*	*10-60 Hz*	*Skin stretch*
Pacinian Corpuscles	*FAII*	*>20mm*	*50-1000 Hz*	*Unlocalized vibration*

2.1.2 Proprioceptive sense

Proprioceptive sense provides the inner information of the body, such as joint angle or muscle contractile force. Proprioception (from Latin proprius) means "one's own" and perception proprioceptive senses. It keeps track of primarily internal information about body position and movement through the combination of inputs from the Kinesthetic and Vestibular senses [14-17]. Kinesthesia informs about the position of body parts with respect to each other while the vestibular sense details the position of the body part to the world through sensing gravity and acceleration.

2.1.3 Requirements on Tactile Displays

According to the high sensitivity of the human tactile sense at the fingertips, tactile displays must match different requirements concerning, for example, the distance of the stimulator elements, their displacement and exerted forces [18]. The most important capabilities of the tactile sense based on psycho-physiological investigations are summarized below. The two-point discrimination threshold describes the minimum distance of two stimulation points that a human can still distinguish.

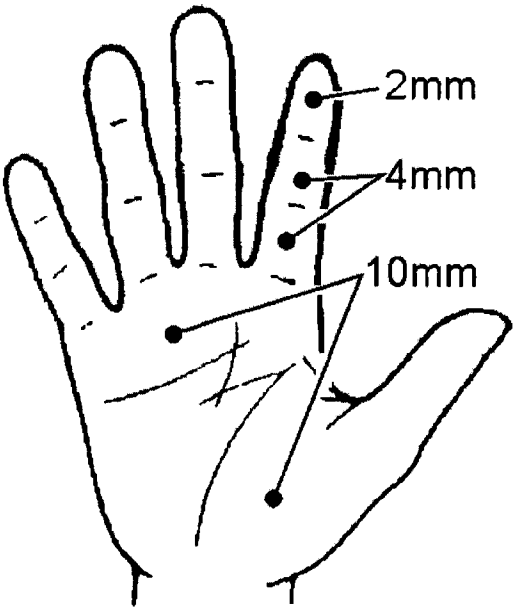

Figure 2.4. Values for the two-point discrimination threshold at different regions of the hand [19].

Its value at the fingertips is between 1 mm [20] and 2 mm [21] at vibrational stimulation. Figure 2.4 shows the two-point discrimination threshold at different regions of the hand given in [19]. For stimulation of the whole area of an average sized hand, including the palm and the fingers, a tactile display needs to have more than 1000 stimulator elements. The maximum frequency of perceptible vibrations is 1000 Hz [22] in which the maximum sensitivity is at 250 Hz [21]. The maximum deformation of the

skin at the fingertips is 3-5 mm [23]. The pain threshold is at 3.2 N at a pin diameter of 1.75 mm that corresponds to a pressure of 1.3 MPa [23]. The minimum perceptible deformation is between 0.07 mm [19] when the finger is allowed to move across a pattern and 2 mm [19] without relative motion. Moy et al. specifies the requirements on an ideal device for realistic tactile feedback [20] and that a tactile display should have 500 mN/mm^2 peak pressure, 4 mm stroke, 50 Hz bandwidth with an actuator density of 1 per mm^2.

An important requirement on tactile displays concerning a realistic feedback in haptic devices is the combination of kinesthetic and tactile feedback. The tactile sensation in real manipulation tasks depends on the current position of the human fingers and is always accompanied by kinesthetic sensations. For kinesthetic feedback there exist force feedback gloves that measure the finger positions for calculating the appropriate forces. A tactile display incorporated into a data-/force feedback glove would complete the haptic sensation. This demands a thin, flexible and lightweight tactile display that allows free movement of the hand and fingers.

2.2 Minimally Invasive Surgery

Minimally Invasive Surgery (MIS) is the practice of performing surgery through small incisions or "ports" using specialized surgical instruments in order to reduce the size of incisions required to gain access to internal tissues during surgery (see Figure 2.5). During conventional "open" surgery, significant trauma is created at the incision site which results in post operational pain and discomfort [24-26]. By contrast, MIS procedures result in reduced bleeding, discomfort, improved patient recovery time, and reduced cost.

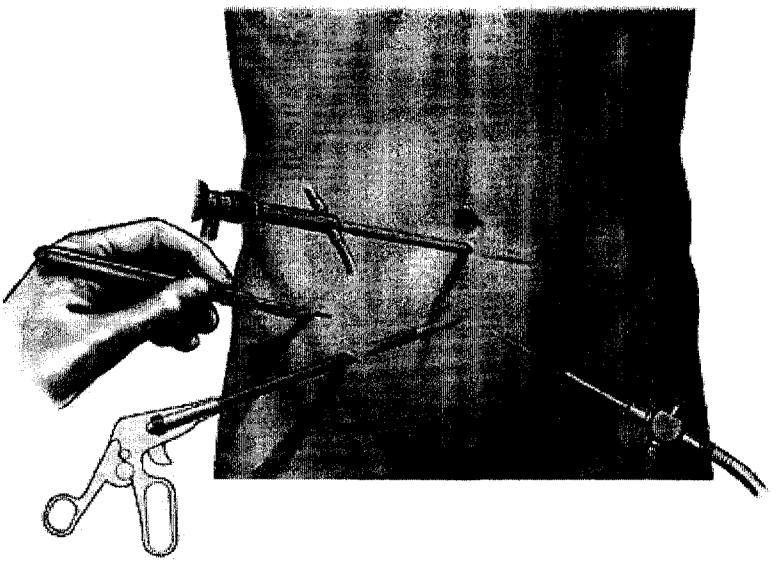

Figure 2.5. Access to internal tissues during surgery

However, MIS is more of a difficult technical procedure for the surgeon for which they are required to train extensively due to the lack of advanced tools and instruments. MIS is, therefore, limited to a number of relatively simple procedures such as cholecystecomy [27] (gall bladder removal) for which there is actually a consensus within the medical fraternity that such practice is in fact beneficial. Due in part to the changing landscape of medical reimbursement in the United States, there is a substantial push from medical subscribers, and their allied organizations, to introduce MIS to other procedures in order to reduce hospital confinement and incumbent cost. Recoveries are typically quicker and less painful by virtue of which more patients are demanding them.

Perhaps the most common form of MIS is laparoscopy [28-30], which is minimally invasive surgery within the abdominal cavity. A rapidly emerging field is MIS cardiac surgery for coronary artery bypass graft surgery. During laparoscopy, a patient's abdomen is insufflated with CO2, and cannulas (essentially metal tubes) in which

pneumatic check valves are passed through small (approximately 1-2 cm) incisions to provide entry ports for laparoscopic surgical instruments. The instruments include an endoscope for viewing the surgical site (a CCD camera/lens combination with slender shaft), and tools such as needle driver, graspers, scissors, clamps, staplers, and electrocauteries. The instruments differ from conventional instruments in that the working end is separated from its handle by an approximately 30cm long, 4-13 mm diameter shaft (Figure 2.6) [31].

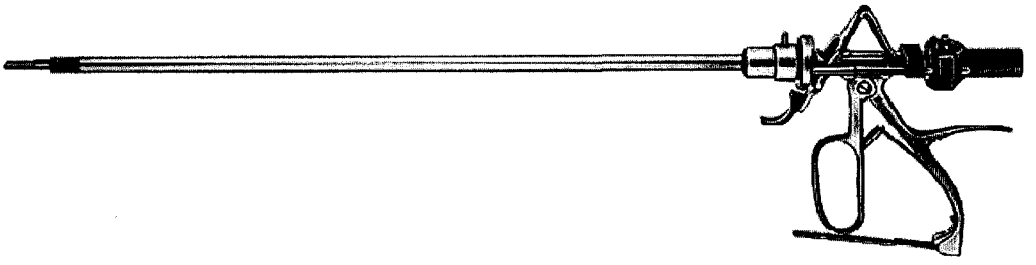

FIGURE 2.6. Commonly used needle driver for minimally invasive surgery

The surgeon passes these instruments through the cannula and manipulates them inside the abdomen by sliding them in and out, rotating them about their long axis and pivoting them about centers of rotation defined roughly by their incision site in the abdominal wall. Typically, a one-degree-of-freedom device (gripper, scissors, etc.) can be actuated with a handle via a tension rod running the length of the instrument. As shown in Figure 2.7, the surgeon monitors the procedure by means of a television monitor which displays the abdominal worksite image provided by the laparoscopic camera.

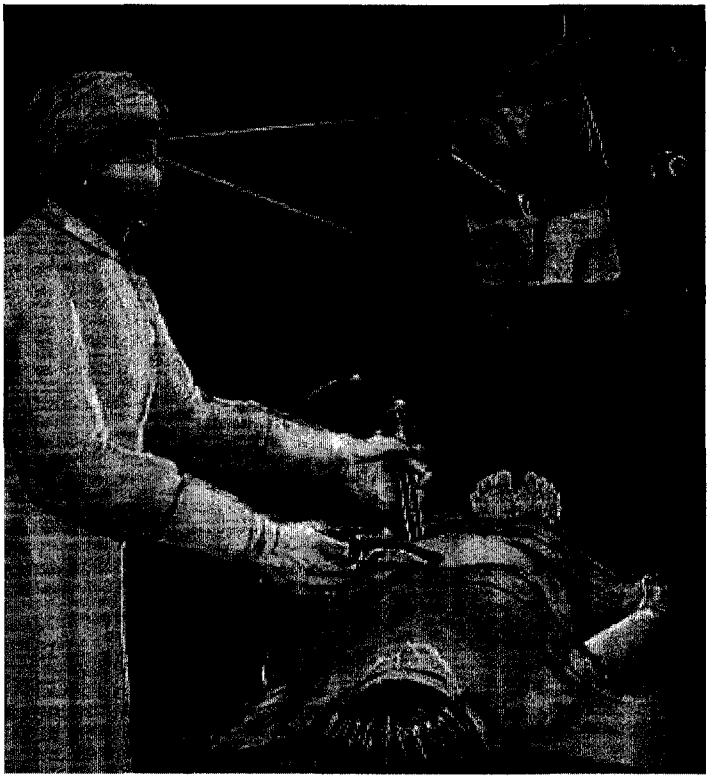

Figure 2.7. The surgeon monitors the procedure by means of a television monitor

There are several disadvantages to the current MIS technology [24,25, 32,33, 34].

1. Visualization of the surgical site is reduced. The operating site is viewed on an upright, two-dimensional video monitor placed somewhere in the operating room. The surgeon is deprived of three-dimensional depth cues and must learn the appropriate geometric transformations to properly correlate hand motions to the tool tip motions.

2. The surgeon's ability to orient the instrument tip is reduced. The incision point/cannula restricts the motions of the instrument from six DOF to four. As a result, the surgeon can no longer approach tissue from an arbitrary angle and is often forced to use secondary instruments to manipulate the tissue in order to access it properly or to use additional incision sites. Suturing becomes particularly difficult.

3. The surgeon's ability to feel the instrument/tissue interaction is virtually eliminated. The instruments are somewhat constrained from rotating and sliding within

the cannula due to sliding friction from the air seal, and the body wall constrains pivoting motions of the instrument shaft. The mechanical advantage designed into MIS instruments reduces the ability to feel grasping/cutting forces at the handle [34-38]. Despite the surgeon's considerable skill and ability to work within the constraints of the current MIS technology, the expansion of minimally invasive medical practice remains limited by the lack of dexterity with which surgeons can operate while using current MIS instruments.

2.3 Tactile Displays

A tactile device is a man-machine interface that can reproduce as accurately as possible tactile parameters such as the texture, roughness, temperature, and shape. Such systems find applications in virtual environments (applications based on the virtual reality technology) and teleoperation applications [39,40].

This chapter aims to overview what has been achieved so far in this field and to summarize the different specifications that may help in the consideration of tactile interface development.

A classification in terms of application domains has been defined in order to present the different tactile interfaces. The different applications are listed below:

- Teleoperation and telepresence;
- Laboratory prototypes to study the different tactile parameters;
- Sensory substitution;
- 3D surface generation;
- Braille systems;
- Games.

From the technological point-of-view, tactile stimulation can be accomplished in different ways. Technologies used for virtual environment (VE) systems were inspired from matrix pin-printers technologies and Braille systems for the blind. Solutions based on mechanical needles actuated by electromagnetic technologies (solenoids, voice coils), piezoelectric crystals, shape memory alloys, pneumatic systems, and heat pump systems based on Peltier modules have been proposed.

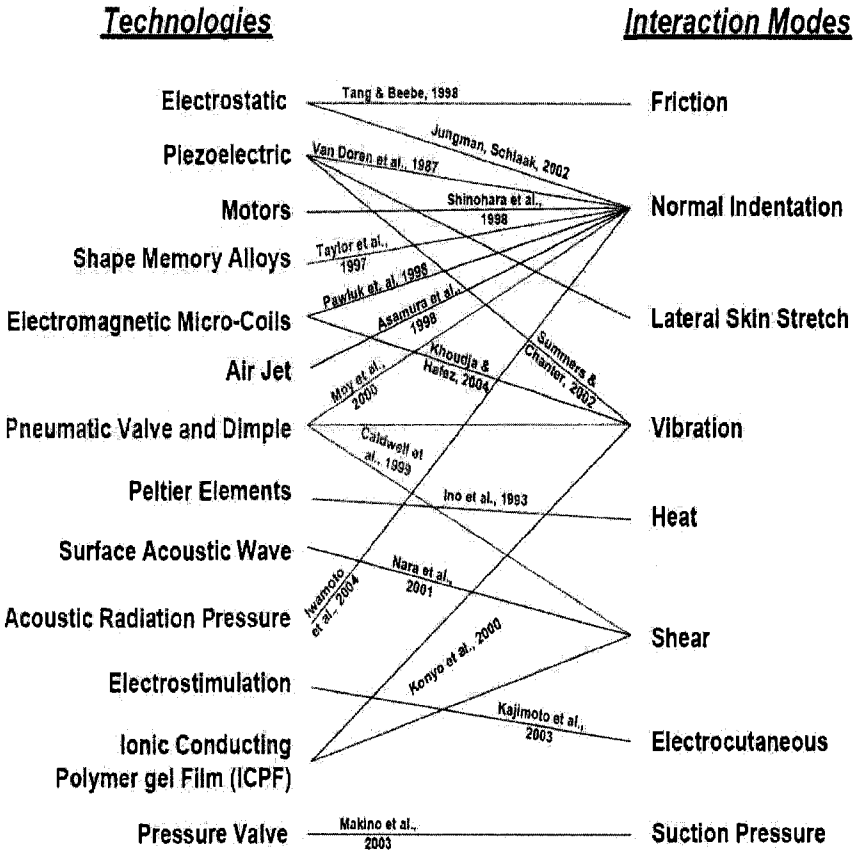

Figure 2.8. Examples of combinations of modes of interaction and actuator technologies for the design of tactile displays [41].

Other technologies, such as electro rheological fluids which change the viscosity and therefore the rigidity under the application of an electric field, are still under investigation. These technologies can be used to stimulate different tactile sensing such

as: vibration, shear, heat, pressure, friction, scratch, indentation. Figure 2.8 shows how the tactile feelings relate to these technologies [41].

2.3.1 Electrostatic Tactile Displays for Roughness

Pelrine et al. reported about an electrostatic actuator composed of a polymeric elastic dielectric that is sandwiched between compliant electrodes [42]. By applying a voltage difference between the electrodes, the dielectric contracts in thickness and expands its area due to the attracting charges on the electrodes [18] (see Figure 2.9). By reducing the voltage, the dielectric returns to its initial shape and can produce forces due to the stored elastic energy.

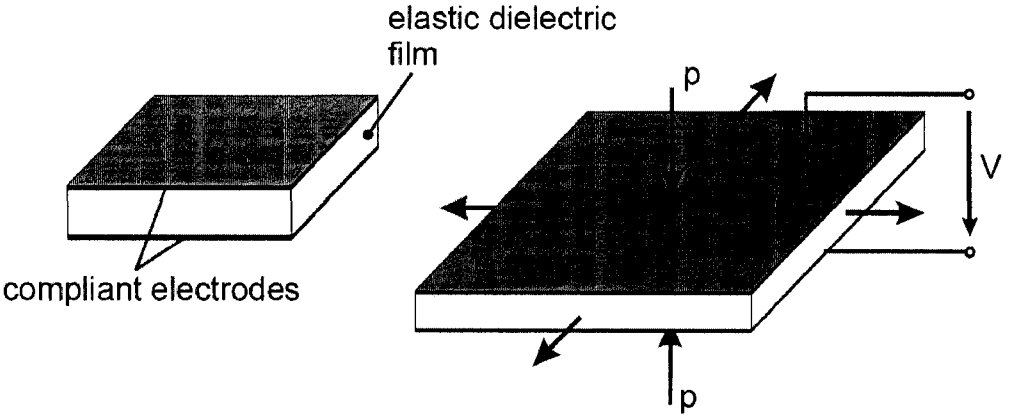

Figure 2.9. Deformation of an elastic dielectric film under electrostatic pressure [18].

To realize an effect with applicable voltages, the thickness of the dielectric has to be in the range of a few microns. The electrodes must be very compliant to prevent constraining the deformation. Pelrine et al. showed more than 30 % relative strain in thickness at electrostatic pressures of over 1 MPa [42] with a silicone elastomer dielectric

between carbon electrodes. Jungmann used a stack of many layers of dielectric films and electrodes to realize large absolute displacements [18] as depicted in Figure 2.10.

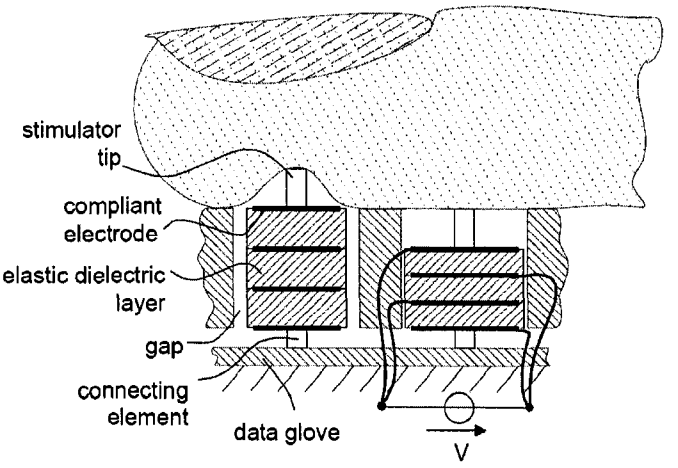

Figure 2.10. Structure and function of an electrostatic tactile stimulator with elastic dielectric [18].

If a voltage is applied between the neighboring electrode layers, the actuator stack will contract and the stimulator tip will disappear below the surface of the device. To ensure the area expansion there has to be a gap around the actuator stack. By reducing the voltage, the electrodes are discharged beyond the voltage source causing a relaxation of the actuator stack. As a result, the stimulator tip is pressed against the skin on top of the device because of the stored elastic energy.

A stimulator with a relative strain of 30 % at an absolute value of 4 mm would require more than 1000 dielectric layers with 10 mm in thickness. This shows the necessity of automating the actuator processing [18]. In Figure 2.11, a possible stimulator arrangement for a tactile display with elastomeric actuators is shown.

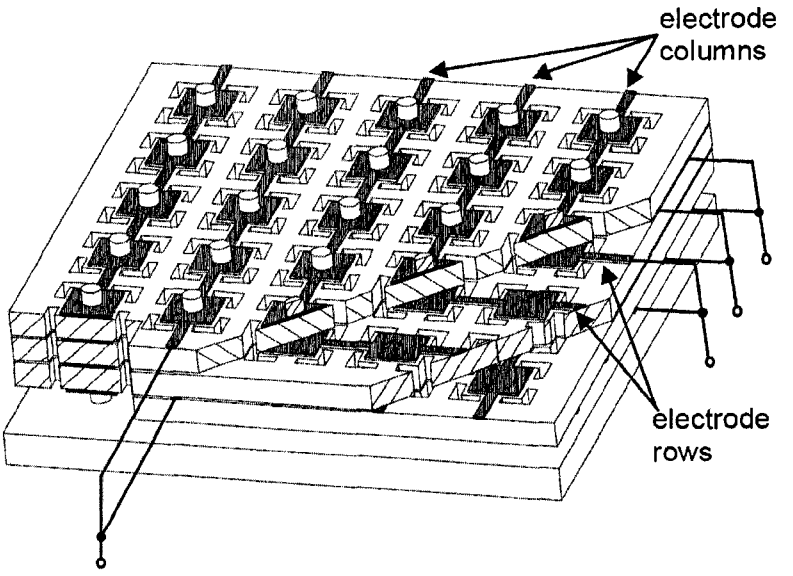

Figure 2.11. Planar stimulator arrangement for a tactile display [18]

Yamamoto worked on a tactile display in which electrostatic force and friction control has been developed for presenting surface roughness sensation [43-45]. The device consists of stator electrodes and a thin film slider on which aluminum conductive layer is deposited. The user puts his index finger on the slider and moves it horizontally to obtain certain tactile sensation. By applying various voltage patterns to stator electrodes, various friction distributions can be generated on the slider, which are transferred to the fingertip so as to generate surface roughness sensation.

2.3.2 Rheological Tactile Displays for Softness

Electro-rheological fluids are those that experience dramatic changes in rheological properties, such as viscosity, in the presence of an electric field. Winslow first explained this effect in the 1940s using oil dispersions of fine powders [46]. The fluids are made from suspensions of an insulating base and particles in the order of one tenth to

one hundred microns (in size). The volume fraction of the particles are between 20% and 60%. The electro-rheological effect, sometimes called the Winslow effect, is thought to arise from the difference in the dielectric constants of the fluid and particles. In the presence of an electric field, the particles, due to an induced dipole moment, will form chains along the field lines as shown in Figure 2.12.

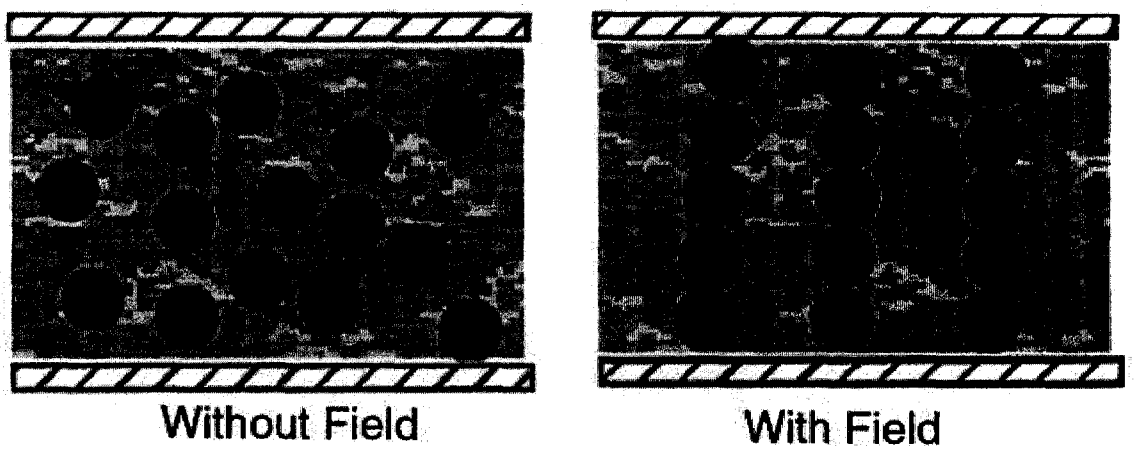

Figure 2.12. Particle suspension forms chains when an electric field is applied [47].

These chains alter the ERF viscosity, yield stress, and other properties, allowing the ERF to change consistency from that of a liquid to something that is viscoelastic, such as a gel, with response times to changes in electric fields in the order of milliseconds. Figure 2.13 shows the fluid state of an ERF without an applied electric field and the solid-like state (i.e. when an electric field is applied). Good reviews of the ERF phenomenon and the theoretical basis for ERF behavior can be found in [48-51].

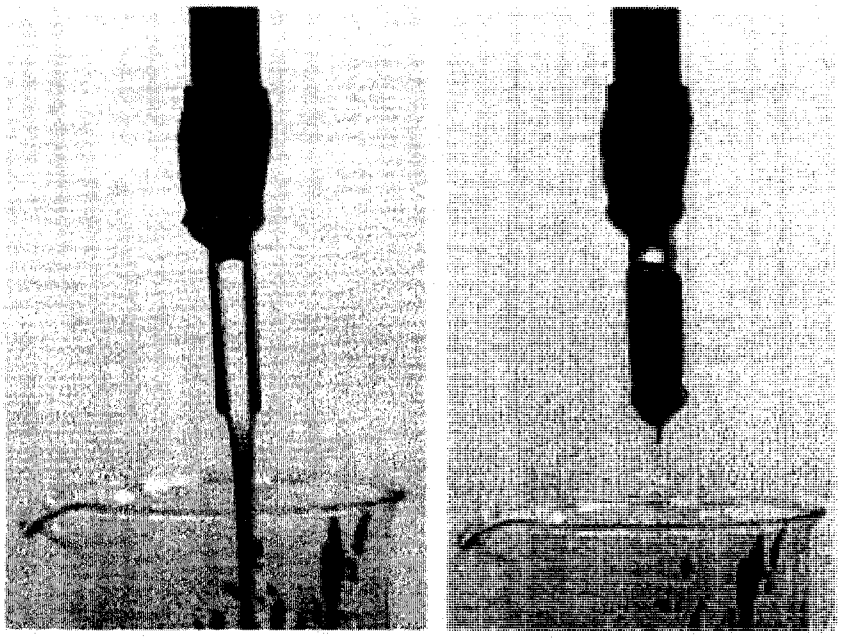

Figure 2.13. Electro-rheological fluid at reference (left) and activated states (right) [47].

Using the rheological fluids does have some disadvantages however. For example, the user must avoid direct contact with the fluid. Problems, such as liquid accumulation, can also arise. Finally, it is very difficult to get a good spatial resolution of the actuators

2.3.4 Electromagnetic Tactile Displays: (Shape Display)

This type of tactile display uses linear movements of an electromotor to simulate the shape. A good example of this category is the work achieved by Wagner et al. [52] in which they used an array of 36 (6x6) servomotors as a shape display. Figure 2.14 shows the pin array and the servomotors which are arranged in such a way that, as shown in Figure 2.14, their rotational movement are converted to linear movements of the pins.

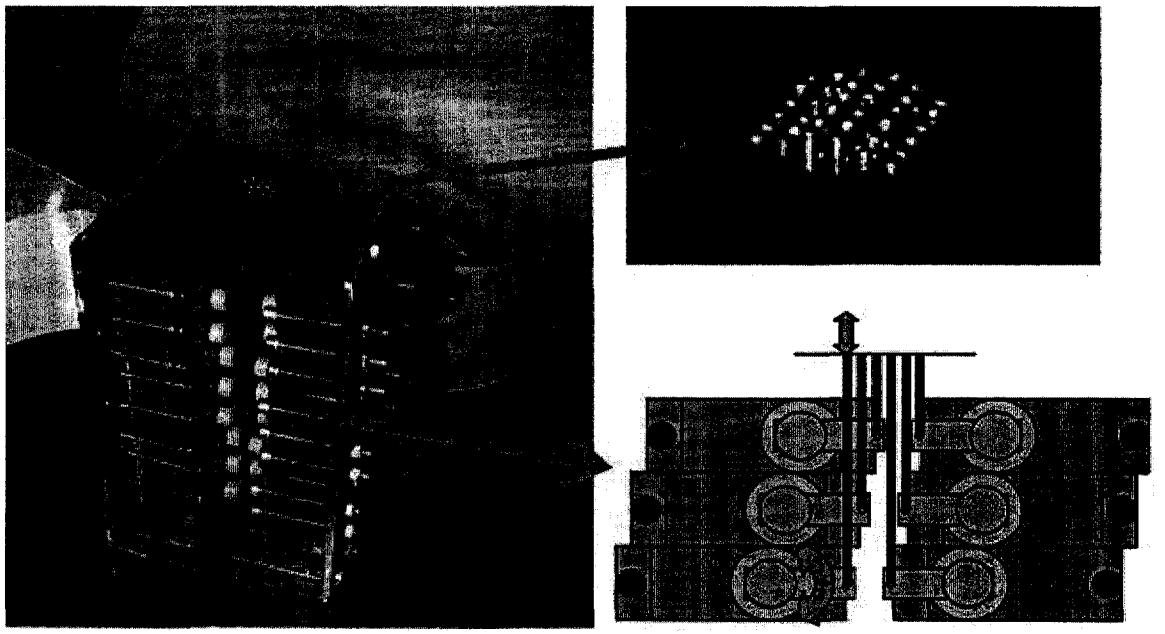

Figure 2.14. A tactile shape display using servomotros, [52].

Ottermo et al. worked on fabricating a shape display using micromotors on the handle of an endoscopic grasper. The sensor array is 24 x 8 mm and consists of 30 piezoelectric sensors, while the tactile display constitutes of 30 micro motors adding up to a total size of 32 mm x 18 mm x 45 mm [53, 54].

2.3.5 Shape Memory Alloys (SMA) Tactile Display (Shape)

Shape memory alloy shortens when it undergoes a phase transition from the Martensitic to the Austenitic phase. This reversible phase transition can be produced by heating the wire above its transition temperature using electric current. It is well known that SMA exhibits hysteresis when cycled through this transition [55]. It is also a relatively slow process because it can take a long time for the wire to cool and lengthen. Some researchers have suggested that it is possible to increase the bandwidth and account

for the hysteresis by developing a model of the process and incorporating this in the controller [56, 57].

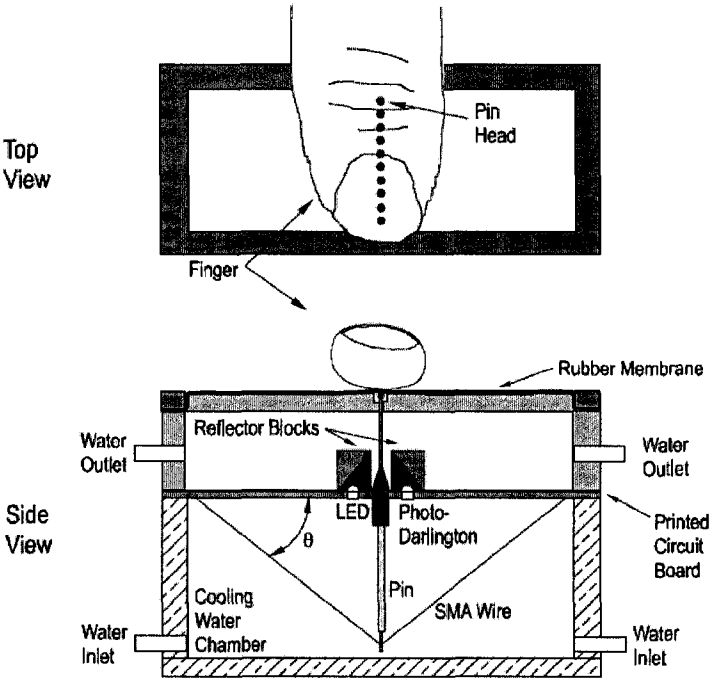

Figure 2.15. Tactile display with SMA in a V shape configuration [58]

While this undoubtedly will work to some degree, Wellman et al. have chosen to increase the bandwidth through careful thermal design and have minimized the hysteresis through position feedback control of the display [58]. Figure 2.15 shows how a single pin is actuated by the SMA. 3D shape display using an array of bars actuated by SMA are presented in [59-61]. Figure 2.16 shows a 3D shape display actuated by SMA.

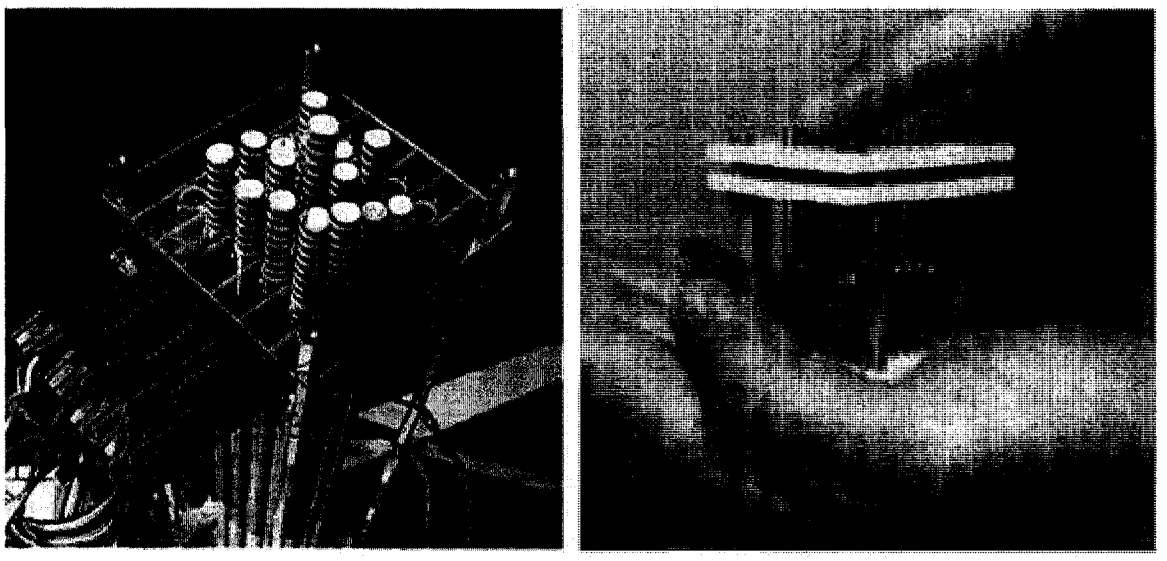

Figure 2.16 - 3D shape displays [59,60]

2.3.6 Piezoelectric tactile display (Lateral skin stretch)

Piezoceramic actuators constitute a practical choice to build an actuator array. They are based on the phenomenon of deformation of a quartz crystal caused by an electrical field. They can be operated over a large bandwidth and are relatively easy to form in a desired miniature structure. Moreover, they are widely available from a variety of sources at reasonable price. Unfortunately, piezoceramic actuators still require high operating voltages although with the advent of technology, they became more mature and piezoceramic properties continue to improve steadily each year. Hayward et al. worked on a tactile display using an array of piezoceramics [62-65]. The objective was to create a deformable structure capable of causing programmable strain fields in a patch of skin with which it was in contact. The exposed side of this structure should thus be made from an array of contactors each of which is moveable tangentially. Among the different piezoelectric elements available, bimorphs can achieve substantial displacement by bending a cantilever (Figure 2.17-a). This bending motion can directly be used to stretch

the skin without the need for extra motion amplification mechanisms. Figure 2.17-b shows the manner in which a collection of bending elements can be arranged to create a two-dimensional array of contactors. One advantage of this design is the creation of a strong, yet modular, structural configuration made of the same part replicated ten times. Of course, all the actuators bend around the same axis, and hence, all contactors move along the same direction. Nevertheless, this was not found to be a limitation since at such a small scale, the resulting sensations seem to be indifferent to the details of skin stretch/shear orientation.

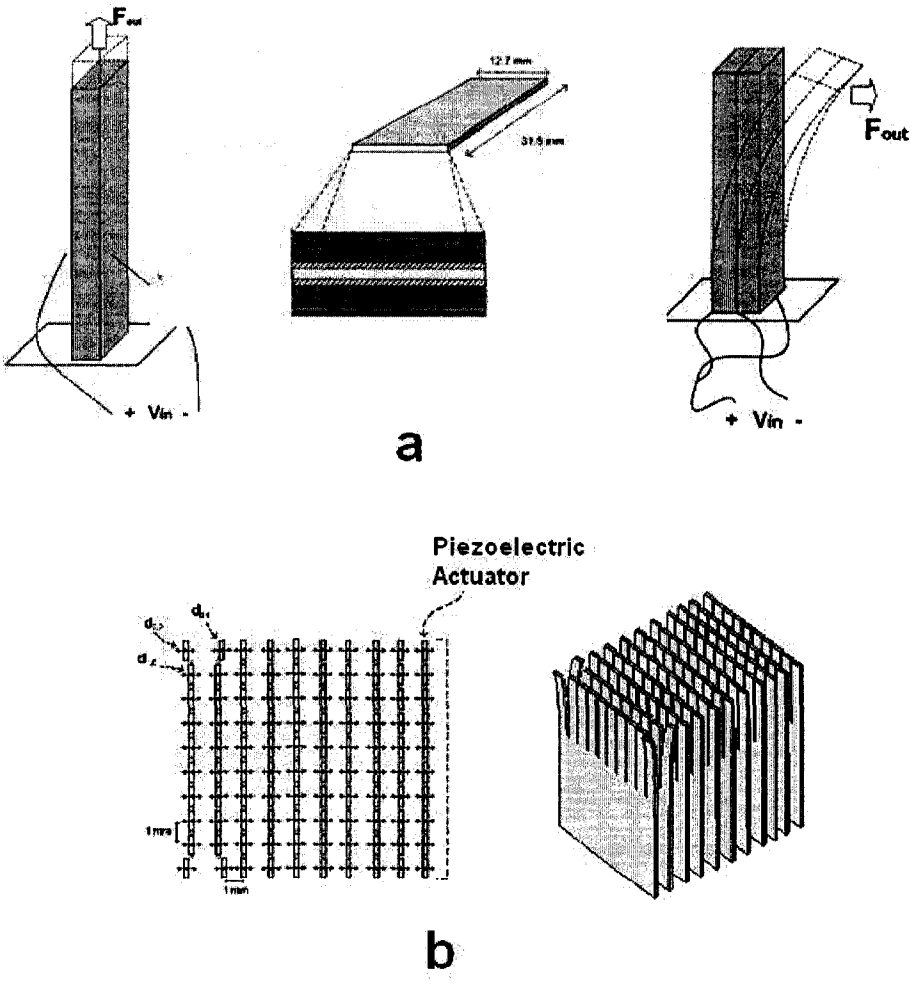

Figure 2.17. a) Bending of a biomorph b) Bending elements arranged into an array [62-64]

In another research work, Kwon et al. described the development of a piezoelectric based planar distributed tactile display capable of displaying textures [65, 66]. The tactile display is composed of a 6 × 5 pin array actuated by 30 piezoelectric bimorphs.

2.3.7 Air Jet Tactile Displays (Surface Indentation)

A new tactile stimulation method is proposed in [67-69] by controlling the suction pressure. This method is based on our discovery of a tactile illusion that we feel as if something like a stick pushes up into the skin surface when we pull skin through a hole by lowering the air pressure.

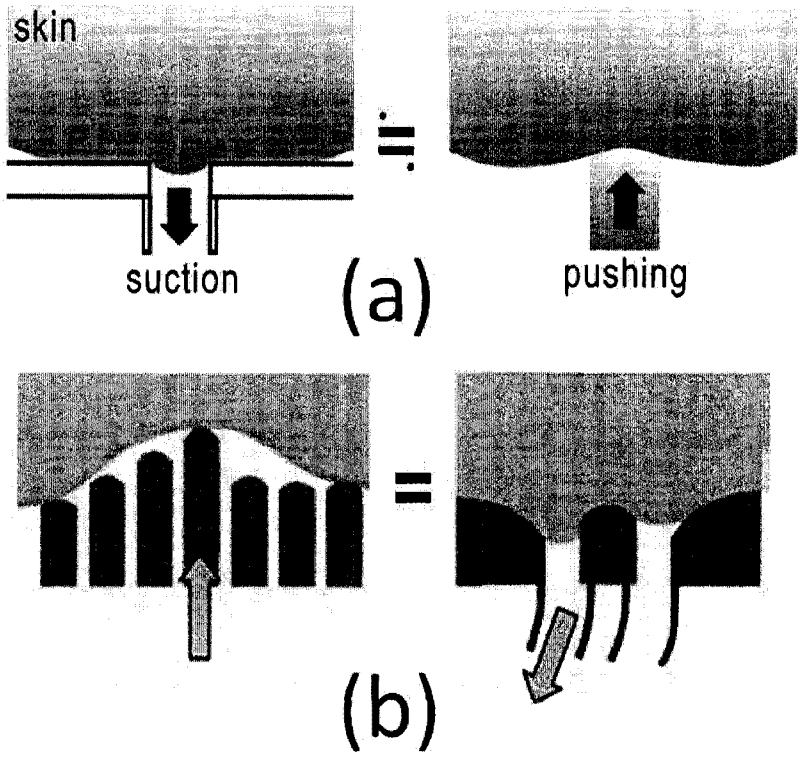

Figure 2.18. - As shown in the figure, we feel pushed sensation by suction pressure [67].

This illustration shows how our tactile mechanoreceptors detects strain energy but cannot differentiate between positive or negative of stress. Therefore we unable to discriminate suction from compression (see Figure 2.18-a and Figure 2.18-b).

2.3.8 Thermal Tactile Displays

Thermomechanical actuators provide good performance in terms of displacement, force and work per cycle. Thermoneumatic micropumps and microvalves are based on sealed cavities that have a flexible side [70]. The cavities are filled with a low boiling point liquid (for instance methyl chloride) and a resistive heater is built inside.

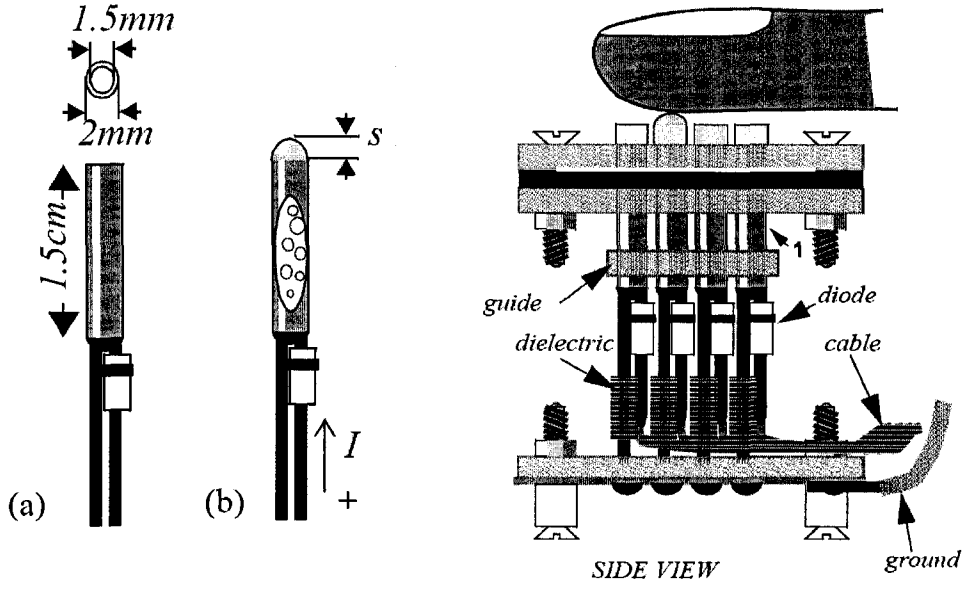

Figure 2.19. - Thermomechanical actuator

When the heater increases the temperature in the cavity, the pressure grows because of the gas resulting from the liquid-gas phase transition and the flexible side of the cavity is displaced. Figure 2.19 shows the actuator proposed in [71]. It consists of a small cylinder made of copper with an end sealed with tin and the other with a flexible

diaphragm. A signal diode has been chosen as heater due to its small size, although it can be replaced by a resistor or another semiconductor device. The main application of the thermal tactile display is in Braille cells [72].

2.3.9 Pneumatic Tactile Displays (Shape)

To provide local shape information, an array of force generators can create a pressure distribution on a fingertip thereby synthesizing an approximate true contact. Researchers at the University of Berkley [73, 74] have developed a prototype of 5 × 5 tactile interface actuated by pneumatic technology with 3 bits of resolution. The pneumatic prototype interface delivers up to 0.3N/actuator. This tactile display, which is similar to servomotor tactile display, has some advantages such as ease of fabrication and no pin friction. Figure 2.20 shows the pin array and the molding which covers the pins.

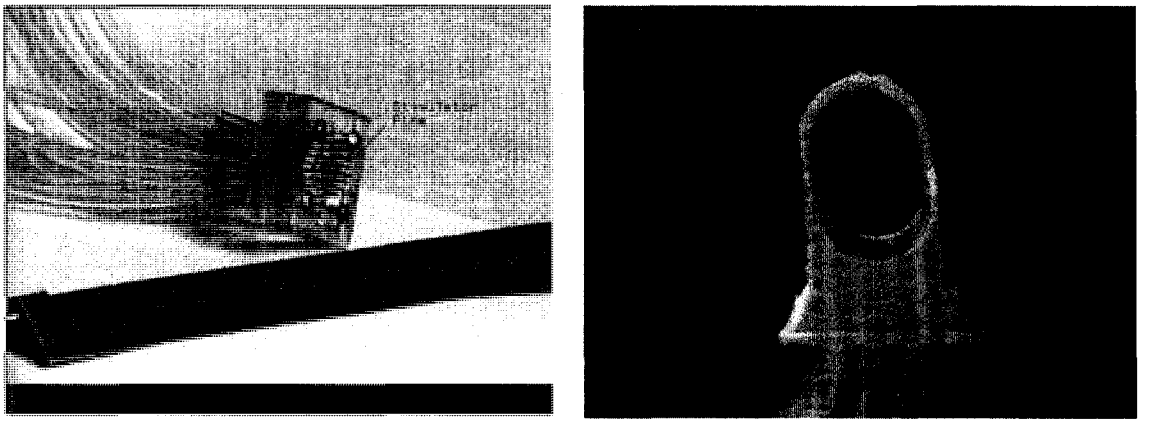

Figure 2.20. - Pneumatic tactile display [73]

2.3.10 Electrocutaneous Tactile Displays

An electrocutaneous display is a tactile device that directly activates nerve fibers within the skin with electrical current from surface electrodes (Figure 2.21) thereby

generating sensations of pressure or vibration without the use of any mechanical actuator [75-78]. It is known that the nerves connected to the tactile receptors can be stimulated selectively by electrostimulation to some extent. The Meissner's corpuscles, which detect dynamic deformation of a finger, can be stimulated by anode current, while the Merkel's disks, which detect static deformation, can be stimulated by cathode current [79-80].

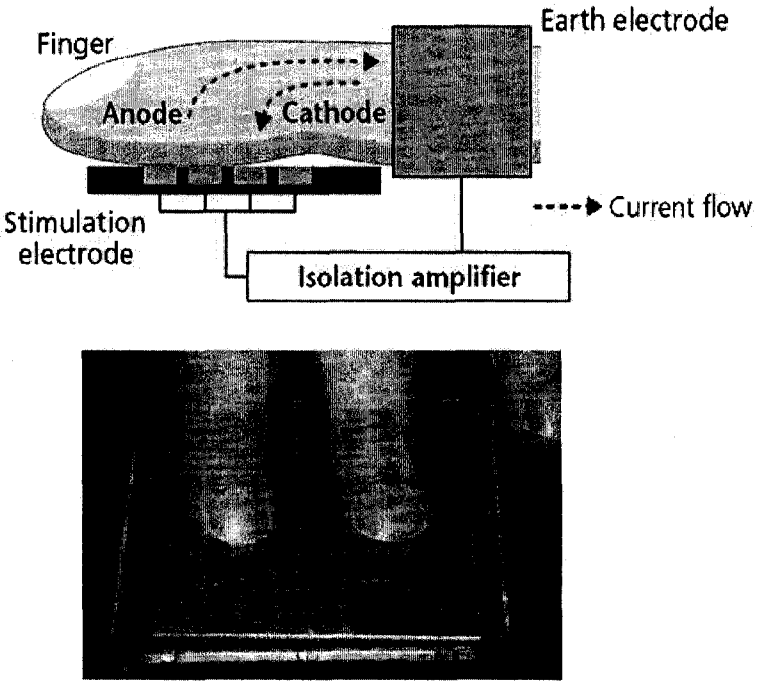

Figure 2.21. a) - Electric current through the finger stimulates nerves b) An electrocutaneous tactile display

2.3.11 Other Tactile Displays

Other technologies have been used to develop tactile displays, including:

- Producing tactile sensation with acoustic radiation pressure [81].
- Tactile glove, that exhibits pressure and temperature feedback, called Teletact[82].
- Effect of linear combination of magnets on the skin [83].
- Array of vibrating pixels unig mirco-clutch MEMS technology [84].

- Using surface acoustic wave (SAW) [85].
- Fusion of visual and tactile feedback [86].
- Composite polymeric known as IPMC or ICPF [87]
- Digital Clay using MEMS technology [88].

2.4 Conclusion

This chapter introduced a brief background in human tactile sensing and perception. The physical parameters and role of human mechanoreception were outlined. This chapter also provided an overview of the research works that have been done so far on tactile displays. The performance and effectiveness of these projects were briefly expressed.

Although many tactile sensing systems based on different technologies were designed and tested, very little work has been done in the field of softness display. In this regard, the objectives of the research in this thesis are summarized below as:

1. Design and development of tactile display capable of demonstrating softness information both graphically and physically.
2. Devising a method for investigating the presence and locating the embedded lumps within tissue during the minimally invasive surgery.
3. Modifying existing laparoscopic graspers in order to measure the softness of grasped objects and demonstrating them to the surgeon.

CHAPTER 3

GRAPHICAL SOFTNESS DISPLAY AND LUMP DETECTION

Following the progresses mentioned in the literature survey, the need for the design of novel display systems is greatly emphasized. The research work presented in this chapter focuses on a novel type of display system, which can be used to convert the sense of touch into images readily recognizable by the surgeon. Using the proposed system, the surgeons can visually determine the softness of the grasped tissue and detect the presence or absence of unusual lumps (such as tumor) by simply grasping the suspicious organ by a smart endoscopic grasper. This chapter is organized in two parts. In the first part the graphical display for representing the softness of the objects grasped by the MIS grasper is presented. The second parts is devoted to detection and localizing the lumps embedded inside the tissues.

3.1 Graphical softness display

The proposed system used for this study consists of an endoscopic grasper integrated with an array of tactile sensors, data acquisition interface (DAQ), and the necessary signal processing algorithms that process the information from the sensor to the display. The complete system is shown schematically in Figure 3.1. When the surgeon uses the endoscopic grasper to grasp a tissue, the sensor array measures the softness of the grasped tissue under each sensing element. The electrical outputs of the piezoelectric sensing elements are then conditioned and transmitted to the data acquisition system.

Using the data acquisition card (NI PCI-6225), the signals are amplified, filtered, digitized and processed by a computer. A computer code was developed in LabView (version 7.1) environment for signal conditioning such as filtering out the line noise. A representation algorithm as later elaborated in this work was used to map the extracted signal's features to a gray scale image. Using the constructed images, the surgeon realizes the softness of the grasped object.

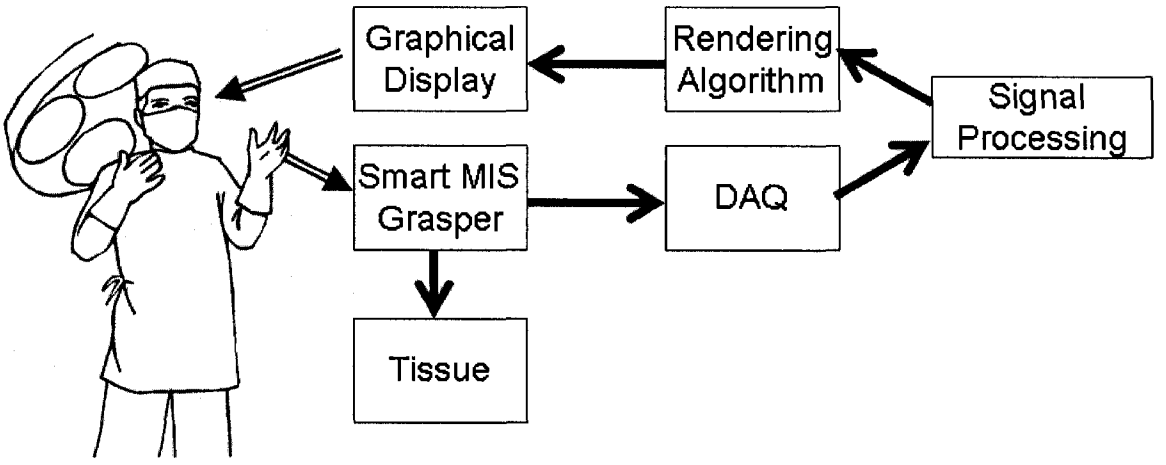

Figure 3.1. The schematic diagram of the complete system.

3.1.1 Feedback system

The smart endoscopic grasper consists of the following items:

1- Array of tactile sensor

2- Data acquisition card

Each sensor in the tactile sensor array has two outputs which are analog voltages resulted from the forces applied by the grasper to the object. These voltages are related to the softness of the grasped object. The sensor outputs are interfaced to a data acquisition card

via the charge amplifiers and buffers. Using the data acquisition card, the signals are amplified, filtered, digitized and finally processed by a computer. The connection of the sensors to data acquisition, created some technical problems which were overcome by adding some electronic components. This is explained in the proceeding sections. Finally these digitized signals are processed and graphically represented by color coding method.

3.1.2 Sensor

The sensor unit consists of a rigid cylinder surrounded by a compliant cylinder. As shown in Figure 3.2-a a Polyvinylidene Fluoride (PVDF) sensing element (Good Fellow Company, USA) is positioned under both rigid and compliant cylinders. When an object is in contact with the sensors, the load is applied on both compliant and rigid cylinders.

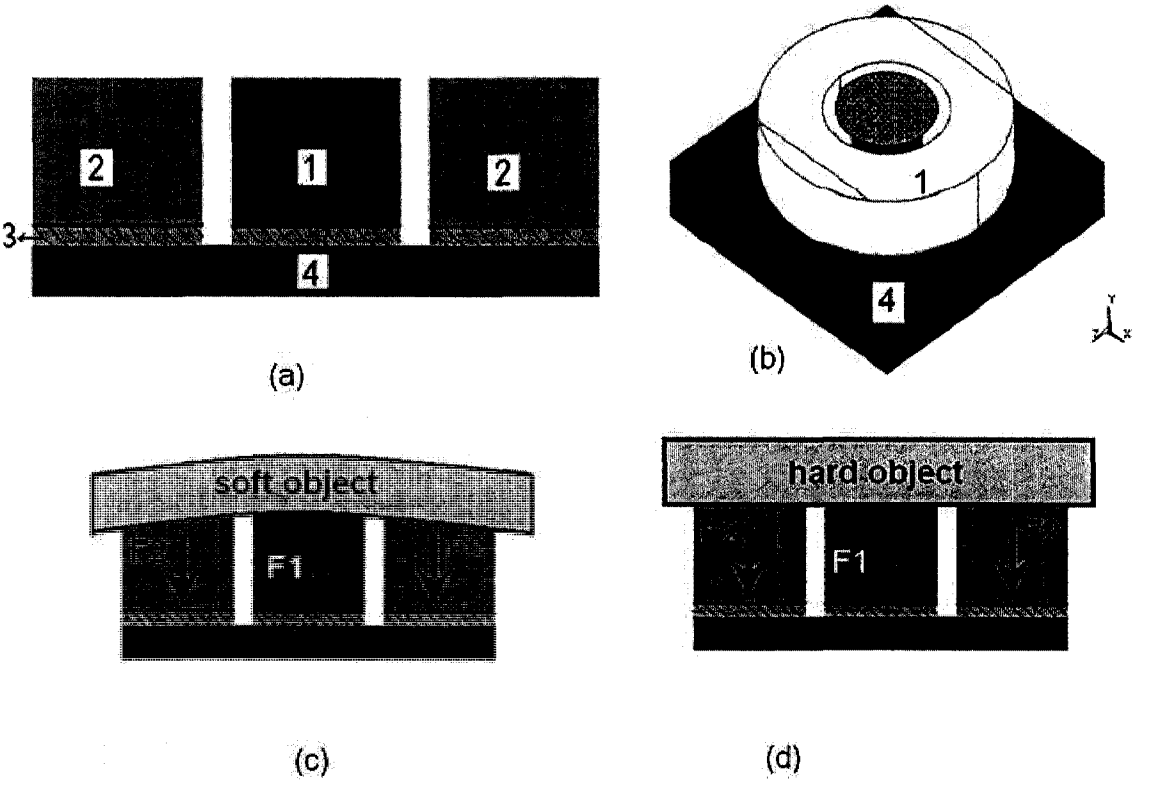

Figure 3.2. a) Cross sectional view of the sensing element: 1-Rigid cylinder 2-Compliant cylinder 3-PVDF 4-Substrate. b) Isometric view of the sensing element. c,d) Transfer of load from rigid to compliant cylinder [91].

As depicted in Figures 3.2-c and 3.2-d, the softer the contact object is, the more the transfer of load from rigid to compliant cylinder will be [89,90]. The force ratio in Figure 3.2 can be calculated as follows [89-91]:

$$\frac{F1}{F2} = 1 + \frac{T2\ E1}{T1\ E2} \tag{3.1}$$

where T1 is the thickness of the sensed object, T2 is the thickness of the rigid or compliant cylinder (which are the same), F1 is the force sensed by the PVDF under the rigid cylinder, F2 is the force sensed by the PVDF under compliant cylinder, E1 is the Young's modulus of the sensed object, and E2 is the modulus of the compliant cylinder. The larger the value of the force ratio, the stiffer the sensed object is when compared with the compliant cylinder.

The integration of 8 tactile sensor units with the prototype grasper is shown in Figure 3.3

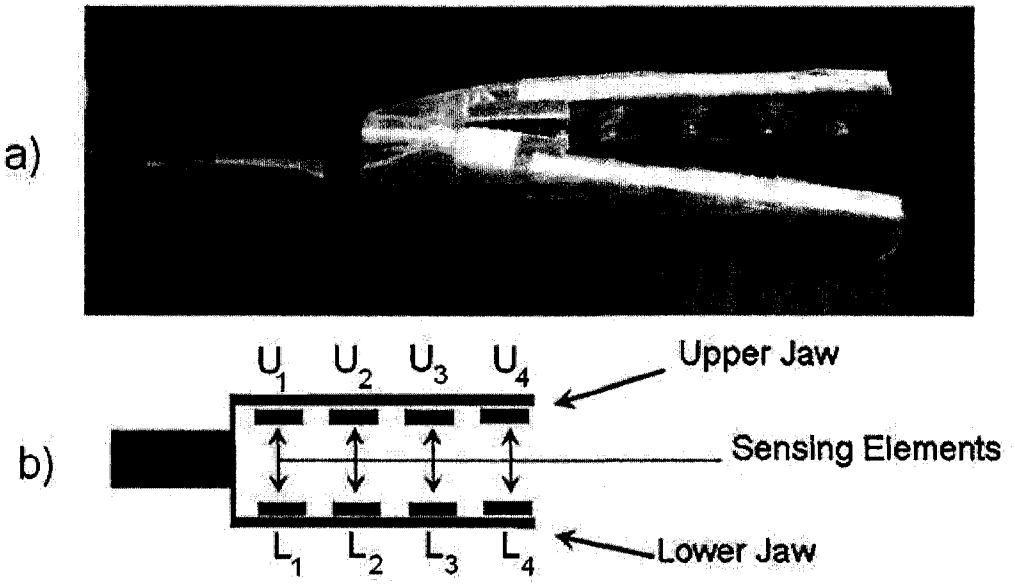

Figure 3.3. a) Photograph of the grasper. b) The two arrays of sensing elements.

Each sensing element in the grasper has two output signals, one from the PVDF under the rigid cylinder and the other from the PVDF under the compliant cylinder. Two arrays of four sensors are microfabricated on the grasper, one on the upper jaw and the other on the lower jaw. These two arrays, numbered from U1 to U4 on the upper jaw and L1 to L4 on the lower jaw, are shown in Figures 3.3-a and 3.3-b. The output of the sensor arrays are then fed to the DAQ, where they are digitized and transmitted to a computer.

3.1.3 Data acquisition system

Data acquisition system (DAQ) contains the necessary hardware which takes the analog signals from the sensor and digitizes them. The DAQ (Type: NI PCI-6225 from National Instrument Company, Resolution: 16 bits, Analog input channel: 70, Analog output channel: 4, sampling rate: 250kS/s) was used in this project.

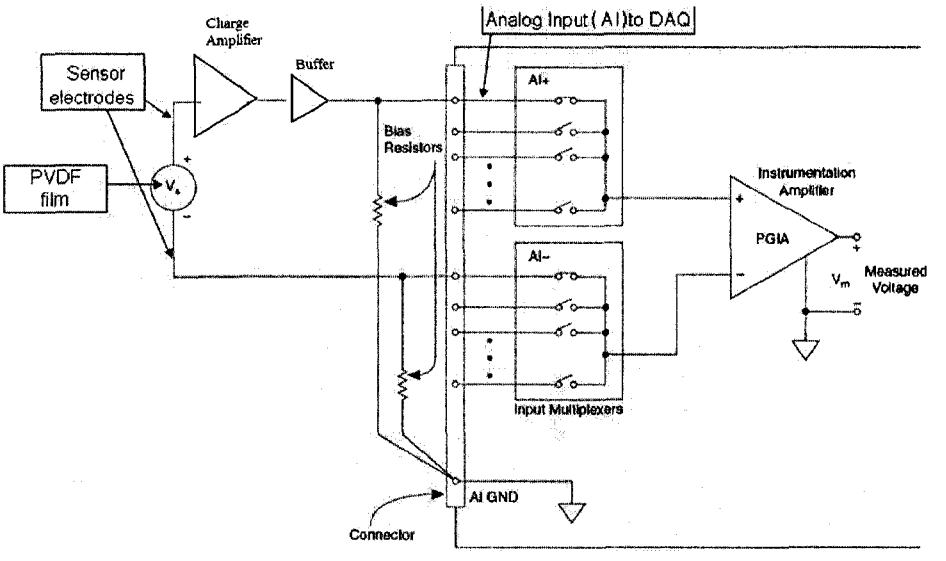

Figure 3.4. The connections from PVDF to DAQ amplifier. In this figure only the first channel is shown. The amplifier is multiplexed between all input channels

Each sensor has two outputs. Each output is connected to a charge amplifier. The output of the charge amplifier is connected to the input channels of the DAQ through a voltage buffer. The buffers are used to reduce the cross talk interference between input channels in the DAQ. Figure 3.4 shows the electronic diagram of the setup. The complete experimental setup is shown in Figure 3.5. The tactile sensor is positioned under a probe. A dynamic load was applied by the shaker which was achieved by a power amplifier and a signal generator. The output of the sensor was fed to the connector box via the charge amplifiers.

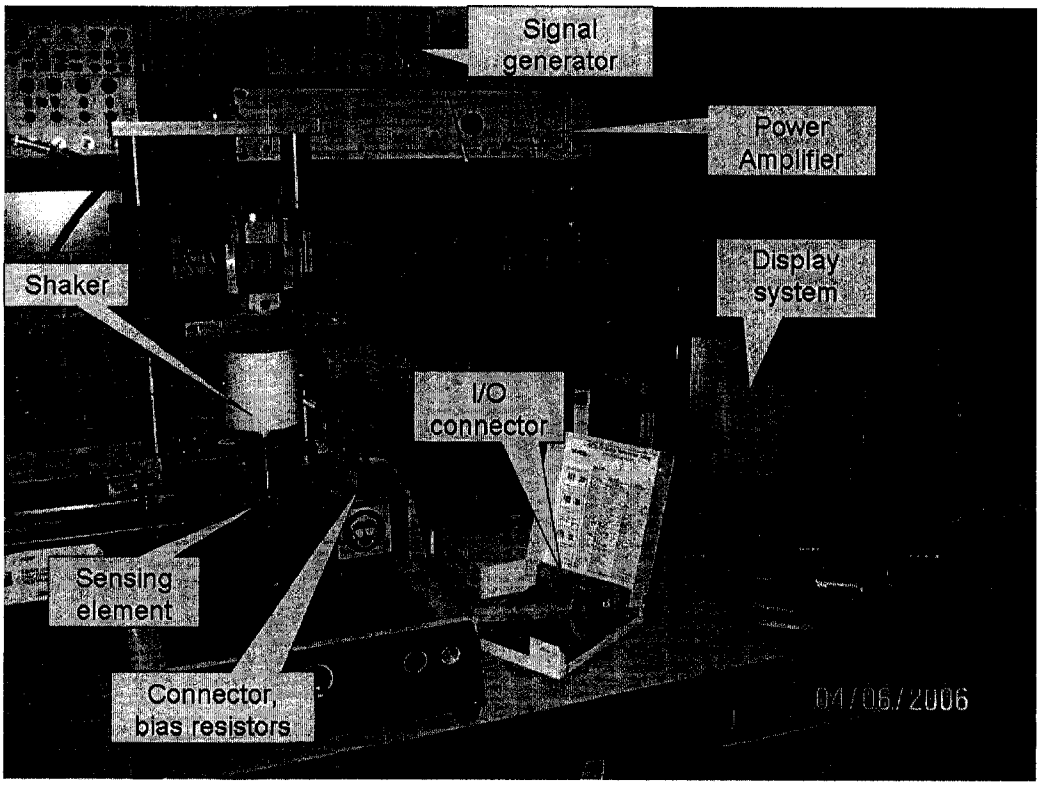

Figure 3.5. Photograph of the complete setup

The data was then transferred to the data acquisition card inside the computer. The block diagram of the data acquisition system is shown in Figure 3.6.

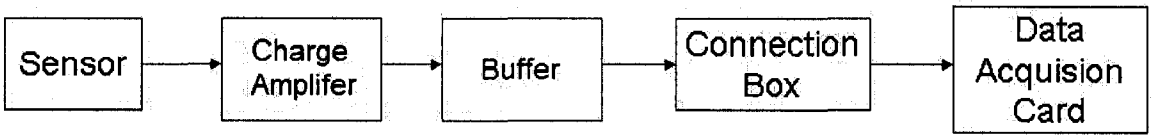

Figure 3.6. Block diagram of data acquisition system

3.1.4 Signal processing

The processing software, developed in LabView 7.1 environment was specifically designed for graphical demonstration of softness of the grasped tissue. Figure 3.7 shows the steps that have been used for the construction of the tactile images.

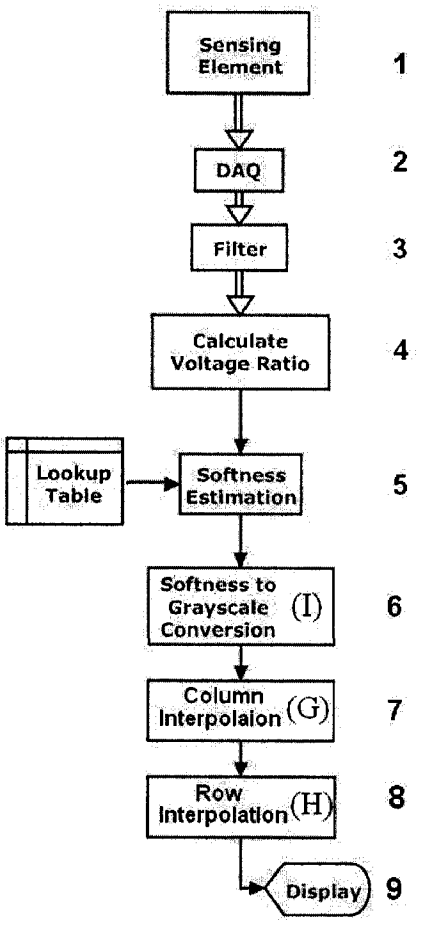

Figure 3.7. The tactile image construction flowchart.

In the first step the sensing elements on the grasper jaws touch an object. The tactile data coming from each sensing element are read in the next step. Two input channels in the DAQ are used to capture data from each sensing element. A filter is used to cancel out the 60Hz line noise from these signals. The filtered signals are then used to calculate the voltage ratio of the rigid and compliant cylinders in each sensing element. The voltage ratio can be used as a criterion to distinguish between different materials with varying softness [90, 91]. Using the standard ASTM D2240 test block kit (Instron Co.) with standard softness values (32.4, 41.9, 52.0, 61.3, 71.1, 81.1, and 88.8 Shore A) the voltage ratio can be experimentally derived for each test material. The resulted voltage ratio and the softness of the material are saved in a lookup table. The voltage ratio calculated for each sensing element, is then compared to the existing voltage ratios on the lookup table. The softness value corresponding to the calculated voltage ratio is extracted from the lookup table and is considered as the softness of the object which is in touch with the sensing element. This softness value is then scaled and converted into grayscale value and can be displayed on the monitor. The complete image for the two tactile arrays which is derived in this way consists of eight cells, arranged in two rows and four columns. Each cell in this 2x4 image is proportional to a sensing element in the two sensor arrays. In step 6, the gray scale value of each cell can be obtained using following relationship:

$$[I] = ([\sigma]/\alpha)K \tag{3.2}$$

where matrices [I] and $[\sigma]$ represent the intensity and softness, respectively. For this study, [I] and $[\sigma]$ take the following forms:

$$[I] = \begin{bmatrix} I_{U1} & I_{U2} & I_{U3} & I_{U4} \\ I_{L1} & I_{L2} & I_{L3} & I_{L4} \end{bmatrix}$$

$$[\sigma] = \begin{bmatrix} \sigma_{U1} & \sigma_{U2} & \sigma_{U3} & \sigma_{U4} \\ \sigma_{L1} & \sigma_{L2} & \sigma_{L3} & \sigma_{L4} \end{bmatrix}$$

where σ_{ij} is the softness for each sensing element obtained from the lookup table in step 5, $[I_{ij}]$ is the gray scale value of the softness display corresponding with the same sensing element. K is a coefficient which determines number of gray scale levels on the display. We considered 256 grayscale levels for displaying the tactile image, i.e. K=256. The symbol α is a coefficient which enables us to show different ranges of softness on the display. We considered four different ranges for softness: Very Soft (α =5 Shore A), Soft (α =20 Shore A), Medium (α =40 Shore A) and Hard (α =100 Shore A).

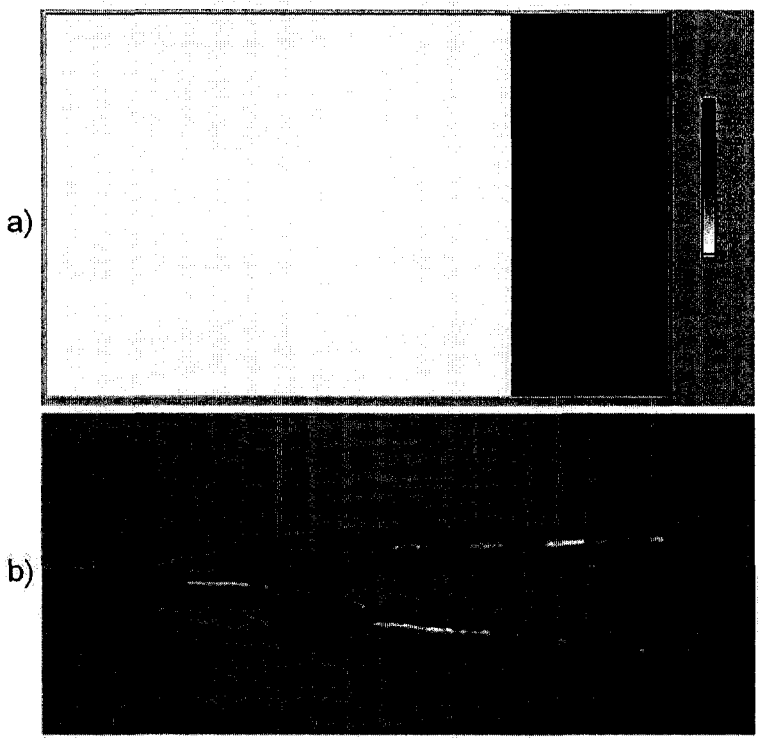

Figure 3.8. Grasper is touching an elastomeric object (with softness of 36 Shore A. a) Softness display representation. b) Photograph of the grasper and the grasped object.

Figure 3.8-a shows the resulting 2x4 image when the grasper is in touch with an object. The two right hand sensors of the grasper (U_4 and L_4) are engaged as indicated in Figure 3.8-b. Furthermore, to create a smooth transition between the columns and rows, an interpolation between the gray scale values of the adjacent columns and rows is necessary. Evidently, increasing the number of cells in both directions enhances the quality of image.

In step 7, a linear interpolation is performed to increase the number of columns from 4 to M. The resulted "2 x M" matrix,$[G]$ is shown in (3.3):

$$[G]=\underbrace{\begin{bmatrix} G_{U1} & G_{U2} & G_{U3} \cdots G_{UM} \\ G_{L1} & G_{L2} & G_{L3} \cdots G_{LM} \end{bmatrix}}_{M\ Columns} \Big\} 2\ Rows \tag{3.3}$$

where:

$$\begin{aligned} &G_{U1} = I_{U1}, \\ &G_{U\frac{M+2}{3}} = I_{U2}, \\ &G_{U\frac{2M+1}{3}} = I_{U3}, \\ &G_{UM} = I_{U4}, \end{aligned} \tag{3.4}$$

and,

$$\begin{cases} G_{Uj} = I_{U1} + (j-1).\dfrac{I_{U2}-I_{U1}}{\frac{M-1}{3}} & , 1 < j < \dfrac{M+2}{3} \\ G_{Uj} = I_{U2} + (j-\dfrac{M+2}{3}).\dfrac{I_{U3}-I_{U2}}{\frac{M-1}{3}} & , \dfrac{M+2}{3} < j < \dfrac{2M+1}{3} \\ G_{Uj} = I_{U3} + (j-\dfrac{2M+1}{3}).\dfrac{I_{U4}-I_{U3}}{\frac{M-1}{3}} & , \dfrac{2M+1}{3} < j < M \end{cases} \tag{3.5}$$

G_{Lj} can be obtained in a similar way.

In the next step, another linear interpolation, as indicated in (3.6) and (3.7), is implemented to increase the number of rows from 2 to N. The resulted matrix H can be shown as:

$$[H]=\underbrace{\left.\begin{bmatrix} H_{11}\cdots & H_{1k} & \cdots H_{1M} \\ H_{21}\cdots & H_{2k} & \cdots H_{2M} \\ H_{31}\cdots & & \cdots H_{2M} \\ \vdots & H_{ik} & \vdots \\ H_{(N-1)1}\cdots & & \cdots H_{(N-1)M} \\ H_{N1}\cdots & H_{Nk} & \cdots H_{NM} \end{bmatrix}\right\}N\ Rows}_{M\ Columns} \tag{3.6}$$

where:

$$H_{ik}=G_{Uk}+(i-1).\frac{G_{Lk}-G_{Uk}}{N-1}\ ,\ i=1,\cdots,N\quad ,\ k=1,\cdots,M \tag{3.7}$$

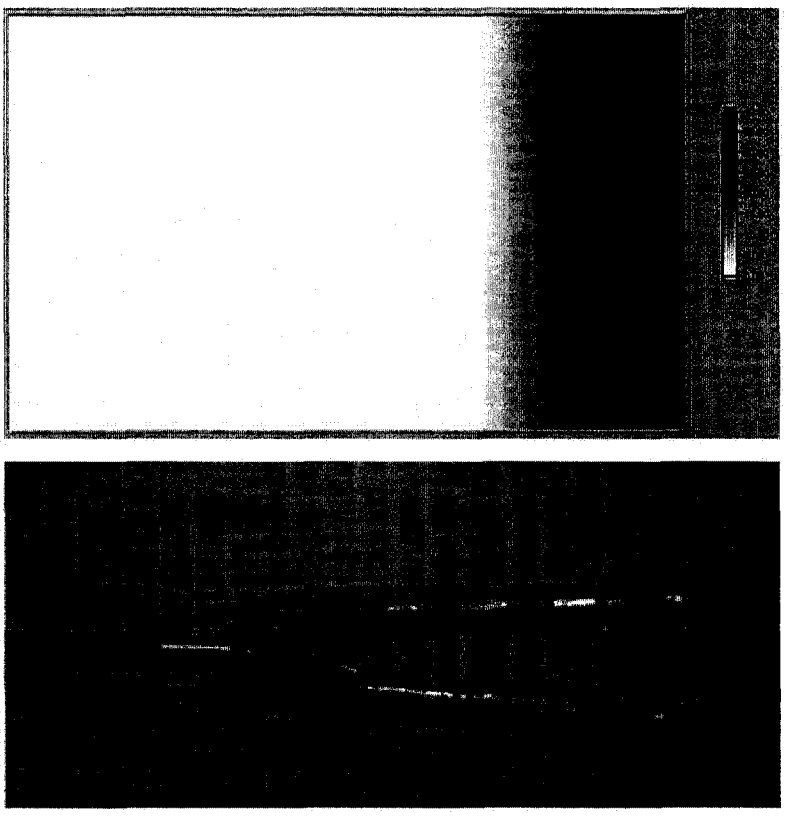

Figure 3. 9. a) The resulting tactile image after interpolation. b) Photograph of the grasper and the grasped object

By following the above mentioned procedures, an image is constructed based on a matrix of 60x100 cells as shown in Figure 3.9-a.

3.1.5 Results and discussion

The results of the conducted experiments are shown as image displays. The softness of the grasped tissue is represented by color coding. As shown in Figure 3.10, a scale in the right hand side of the graph shows the color coding numerically. In this case, the two right hand sensors of the grasper (U_4 and L_4) are engaged. The softness display shows the sensed object in gray scale. Here, both U_4 and L_4 show the same softness.

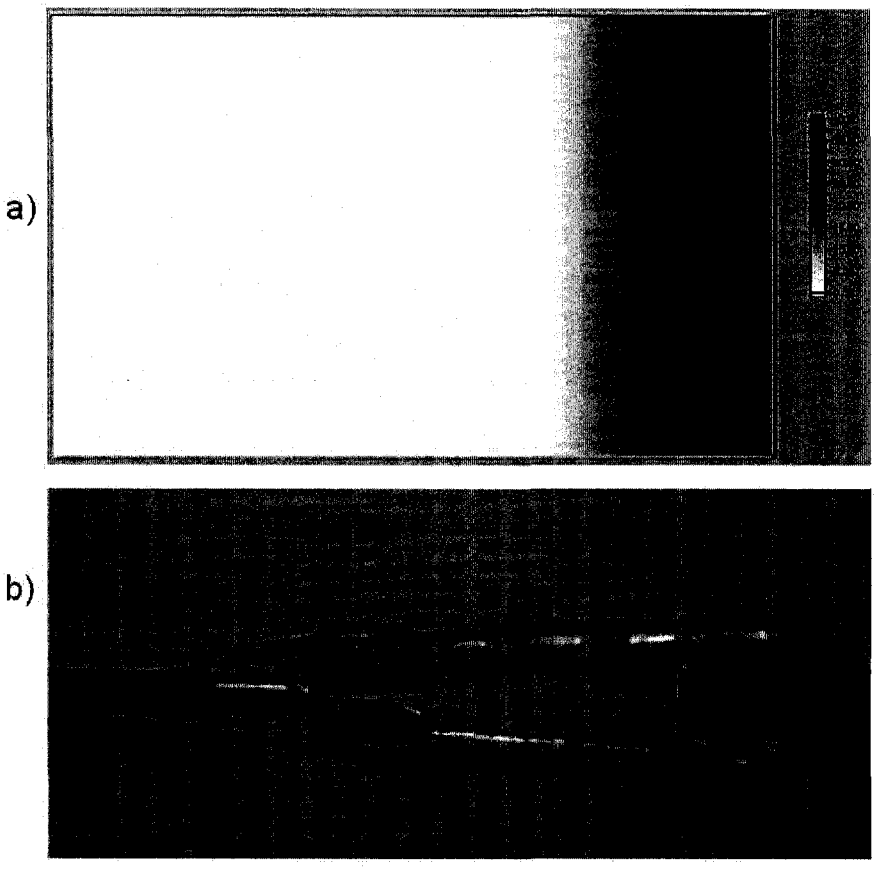

Figure 3.10. a) The resulting tactile image after interpolation. b) Photograph of the grasper and the grasped object

This means that the grasped object has the same softness throughout its thickness. In Figure 3.11, the upper and lower jaws are grasping two different materials with different softness. The material grasped by the upper jaw is softer than the other material. The result in the softness display is presented by two different grayscales on the upper and lower part of the display.

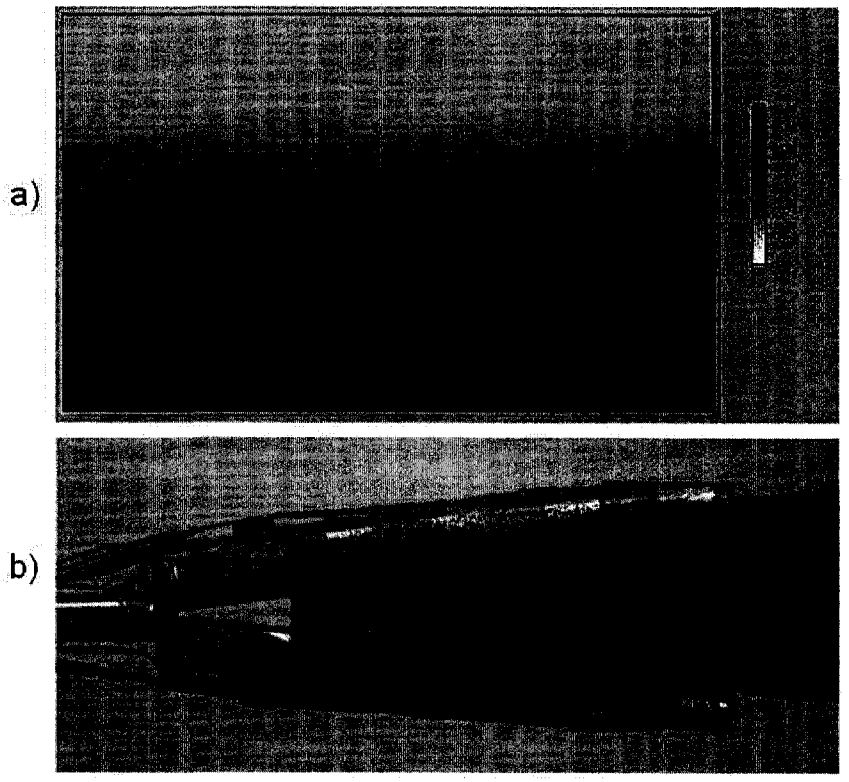

Figure 3.11. Upper and lower jaws are touching two different objects (with softness of 30 and 10 Shore A). The objects are located in parallel. a) Tactile image display. b) Photograph of the grasper and elastomers.

In Figure 3.12, the two central sensors of the upper jaw, i.e. U_2 and U_3, are in touch with a soft material and the other sensors on the upper and lower jaws are in touch with a harder material. Finally in Figure 3.13, the sensors U_4 and L_2 are in touch with a soft material while other sensors are in touch with a harder material.

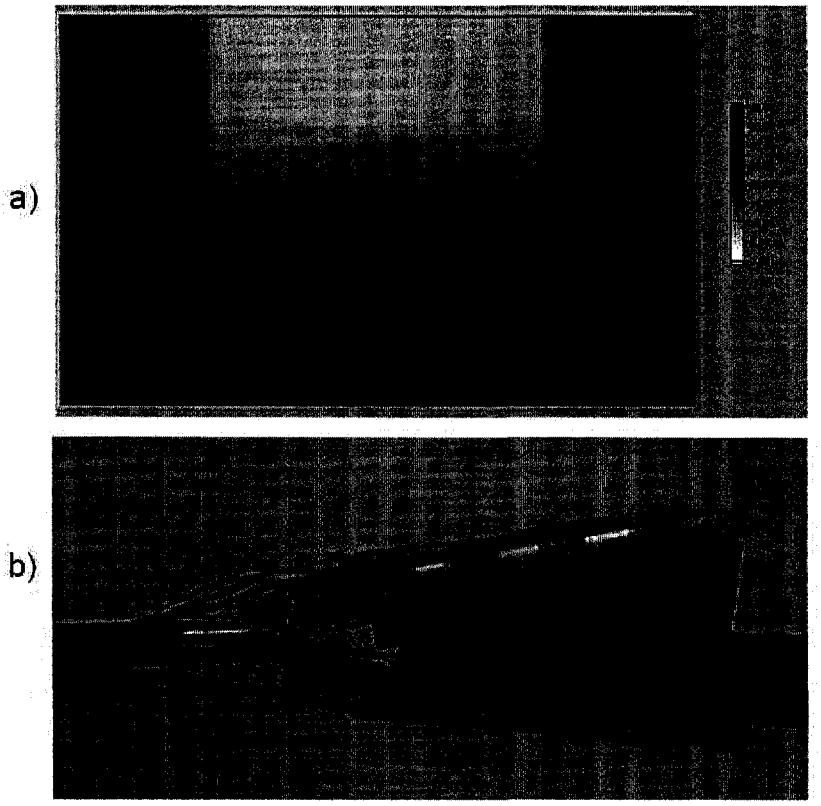

Figure 3.12. Grasper is touching two different objects (with softness of 30 and 10 Shore A). One embedded object is located on top. a) Tactile image display. b) Photograph of the grasper and elastomers.

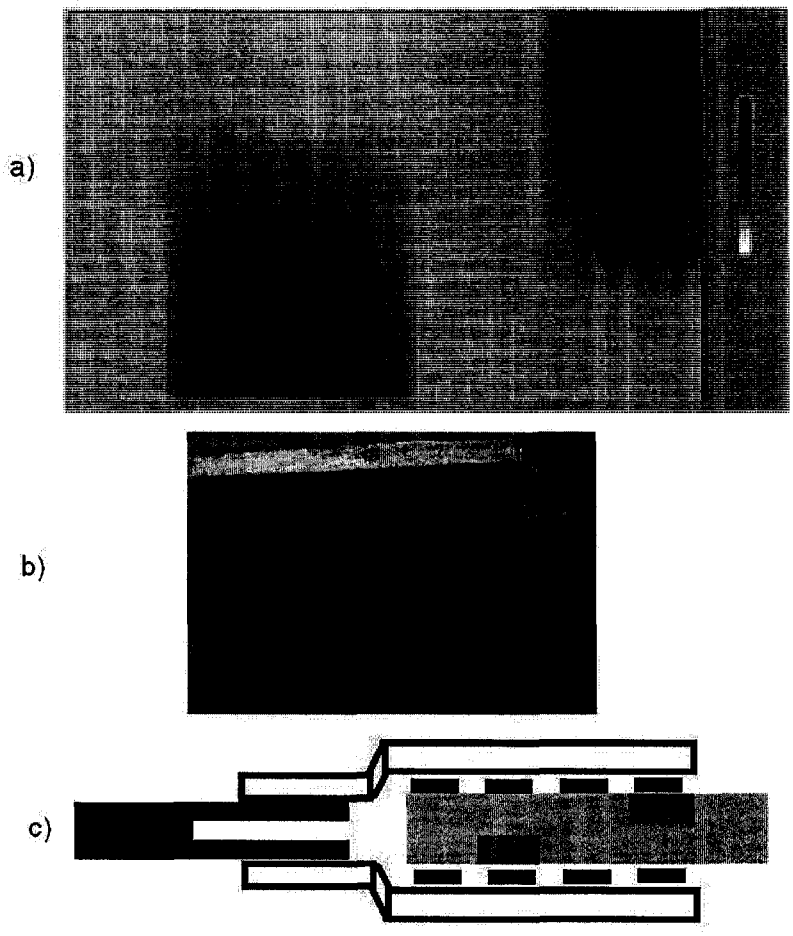

Figure 3.13. Grasper is touching two different objects (with softness of 30 and 10 Shore A). Two embedded objects are located on top and bottom sides. a) Tactile image display. b) Photograph of the grasper and elastomers. c) Grasped object with two different softness demonstrated using different colors.

3.2 Lump detection

While much work has investigated the tumor detection in breast cancer [92-95], little work has examined the proper way to find and localize the lump in MIS surgery. All these methods present advantages but are not useable in MIS surgery. With this situation in mind, a novel tactile sensor that can be used for nodule detection in MIS is presented in [96]. This research work focuses on the processing the data gathered from the sensor described in this work, and converting the sense of touch into the images readily recognizable by the surgeon. Using the proposed system, the surgeons can detect the presence or absence, location and approximate size of unusual lumps (such as tumor) by simply grasping the suspicious organ by a smart endoscopic grasper.

3.2.1 System design

The teletaction system used for the experiment consists of a tactile sensor that measures the pressure, data acquisition card and its electronics, and the necessary signal processing algorithms that process the information from the sensor to the display. The tactile sensor (PVDF film) measures the pressure across the seven sensing elements (1.5 mm width spaced 0.5mm apart). Each sensor in the PVDF array has an output which is an analog voltage resulted from the forces applied by the object. The electrical outputs of the piezoelectric sensing elements are then conditioned and transmitted to the data acquisition system. Using the data acquisition card, the signals are amplified, filtered, digitized and processed by a computer. A computer code was developed in LabView (version 7.1) environment for signal conditioning such as filtering out the line noise. In addition, a rendering algorithm also developed in LabView, was used to map the

extracted signal's features to a gray scale image. Using the constructed images, surgeon realizes not only the presence or absence of lump, but also the approximate size and location of the detected lump.

3.2.2 Sensor structure

The details of the sensor including its design and working concept have already been presented in [97]. The design of the deformable force-stretch array sensor is shown in Figure 3.14-a. The structure of the sensor integrated with an MIS grasper, as shown in Figure 3.14-b, is corrugated to ensure a firm grasping of the tissue. Figure 3.14-b shows the proposed grasper in which just the lower jaw is equipped with an array of the tactile sensors. The sensor array consists of 7 equally spaced PVDF films which are placed in parallel on an elastic material. The number of the sensors, their length, width and thickness as well as the space between them could be optimized for each particular application. In this study, in order to replicate the human finger's spatial resolution, the sensor array was made of seven equally spaced piezoelectric PVDF base sensing elements.

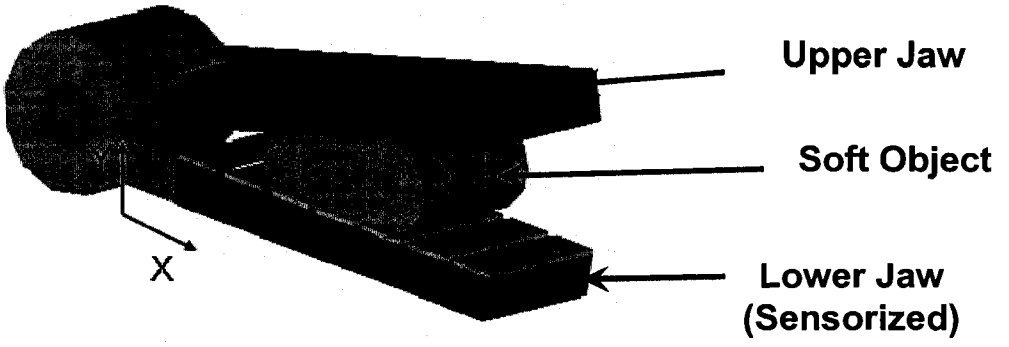

Figure 3.14. A view of the grasper with one active jaw equipped with an array of the seven sensing elements

The spatial resolution for human finger using the Two-Point Discrimination Threshold (TPDT) is reported to be about 2 mm [98]. Therefore, 1.5 mm wide sensing elements positioned 0.5 mm apart were considered for this study. Evidently, a finer array will yield into better spatial resolution than that of human finger. The outputs of these PVDF films are then registered and transported to data acquisition card. Figure 3.14 shows the sensor array and its PVDF films. The PVDF can be modeled as a voltage source with very high output impedance. As the data acquisition card needs the input impedance be less than 100KOhm, a buffer is necessary to match the impedance. The voltages from PVDF sensing elements are read by the DAQ. Since the sensor consists of seven PVDF films, the total of 7 analog input voltages is registered.

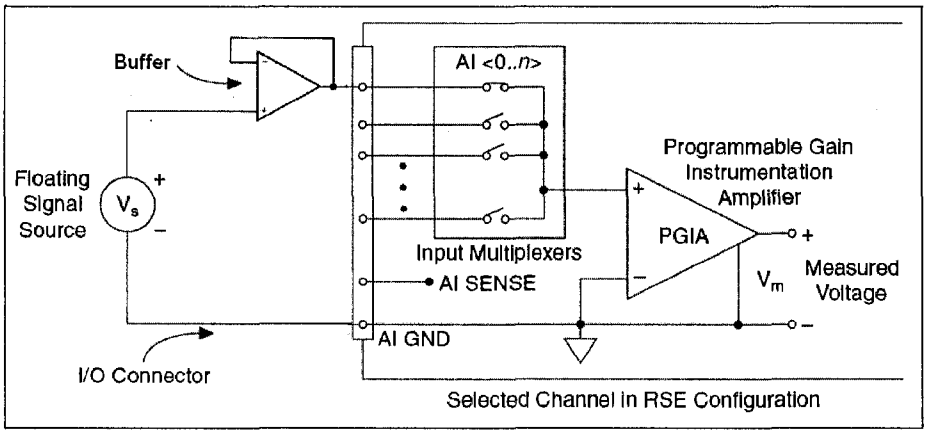

Figure 3.15. The connections from PVDF to DAQ amplifier. In this figure, only the first channel is shown. The amplifier is multiplexed between all input channels

The DAQ main amplifier was used in RSE (reference single ended) mode. Hence, in order to read 7 input voltages, 7 channels from the DAQ were utilized. Sensors electrodes connected to this board are interfaced with the DAQ by a flat cable. The

detailed electronic connections from PVDF to the differential DAQ amplifier (instrumentation amplifier) is shown if Figure 3.15.

3.2.3 Rendering algorithm

Two configurations of the sensors on the grasper are examined. The grasper structure shown in Figure 3.14, with one sensorized jaw is capable of locating the lumps in one dimension (x-axis), while the grasper with two sensorized jaws, which will be described in Section 4.2, can characterize the lumps in two dimensions-- x and y axes (location of the lump in y direction can be considered as lump depth). In both designs, when there is no extraneous feature in soft object, depending on the grasper geometry and design, all sensing elements show either an equal output voltage or exhibit a regular pattern that is assumed as background frame. The presence of the lump causes an uneven voltage distribution through the sensing elements. The deduction of the background frame from the total response results in the net effect of the lump and increases the sensitivity. In addition to the lump detection, the softness of the bulk soft object in the sections with no embedded masses can also be measured [99].

The outputs of the sensing elements depend on several factors, such as the ratio of the Young's modulus of the lump (E_L) to that of the tissue (E_T), the size and depth of the lump and the magnitude of the applied load. Extracting all features of lump from the minimal sensor used in this study is a formidable task, as some combinations of lump stiffness, size, depth and the applied force create similar output pattern. This complexity is also reported by other researchers [92]. However, there are some constraints that can be used to reduce the number of variables or at least to control their range. For instance, our

analysis [100] shows that for $\frac{E_L}{E_T} > 10$, the variation of this ratio has negligible effect on the output. Fortunately, the absolute majority of the reported stiffness for the tumors are greater than this ratio [92]. Therefore, in the practical range, the output response is not much influenced by the variation of the Young's modulus of the lump. Another influential factor is the magnitude of the applied load. The contact force between the grasper and the tissue depends on the load exerted by grasper jaws to the tissue. Therefore, it is necessary to measure the total applied load besides the pressure distribution. The applied load can be measured in different ways. For instance, a strain gauge attached to the jaw can provide the data on the magnitude of the applied load. Another approach to measure the applied load was presented in a previous work, in which an extra PVDF film is used at the supports of each sensing element [97]. In the experiments conducted in this study, the load was measured using a reference load cell. Furthermore, to reduce the number of contributing parameters, throughout this article, the force was kept constant. The other remaining factors are the size of tumor, its location in x and y directions. Since the majority of masses can be approximated as spherical features, the number of parameters to characterize the size of the sensor can be reduced to one value, i.e., the lump radius. The first design (see Figure 3.14) overlooks the depth of lump and locates lump merely in x direction. While, by using two sets of arrays of sensing elements in the second design described in Section 3.2.3.1, it is possible to determine the depth of lump as well.

3.2.3.1 Graphical representation of localized lumps in one dimension

As shown in Figure 3.14, in the first design the lower jaw is equipped with the sensor array, hence the upper jaw only applies compressive load to the object containing lumps. To graphically represent the location of the lump, initially an image with seven vertical parallel bands corresponding to the seven sensing elements was considered (see Figure 3.16-b). The intensity of each band was considered to be proportional to the output of the corresponding sensing element. The voltage distribution along the sensor array can be considered as a vector $\{V\}_{1\times7}$ that is related to the intensity vector $\{I\}_{1\times7}$ by:

$$\begin{cases} I_i = \left(V_i / \alpha\right).(K-1) & ,V_i \le \alpha \\ I_i = K-1 & ,V_i > \alpha, \end{cases} \quad , \; i = 1,..,7 \tag{3.8}$$

where α is the normalizing factor that determines the working range (very soft, soft, medium, etc.), and K is the number of gray scales that are used in construction of graphical image (here K=256). It is seen from Equation (1) that for a given α, when $V_i \le \alpha$, the scaling factor α maps the input voltage domain into interval [0, 1], then this value, using (K-1) factor, would be mapped into the corresponding gray level, between 0 to 255. Once $V_i > \alpha$, all the values of V_i would be mapped to the maximum intensity (i.e, $I_i = 255$). For instance, Figure 3.16-b shows the graphical display for the case that two lumps were detected in the grasped tissue. In this case, one of the lumps had been positioned above the sensing element No. 6 and the other one had been placed above and between the sensing elements 2 and 3 (see Figure 3.16-a for the configuration). However, due to the limited number of the sensing elements, the quality of image shown in Figure 3.16-b was not satisfactory. Therefore, by using an interpolation technique the quality of

the image as shown in Figure 3.16-c was enhanced. Prior to implementation of interpolation, the number of elements had to be increased from 7 to any desired number (N). To do this, (N-7) extra elements were required. Therefore, $\frac{N-7}{6}$ elements were inserted between each two original elements. The resulted (1xN) vector {G}, is in the following form:

$$\{G\} = \underbrace{\{G_1\, G_2 \cdots G_{N-1}\, G_N\}}_{N\ elements} \tag{3.9}$$

in which

$$G_1 = V_1, \quad G_{\frac{N+5}{6}} = V_2, \quad G_{\frac{2N+4}{6}} = V_3, \quad G_{\frac{3N+3}{6}} = V_4,$$
$$G_{\frac{4N+2}{6}} = V_5, \quad G_{\frac{5N+1}{6}} = V_6, \quad G_N = V_7$$

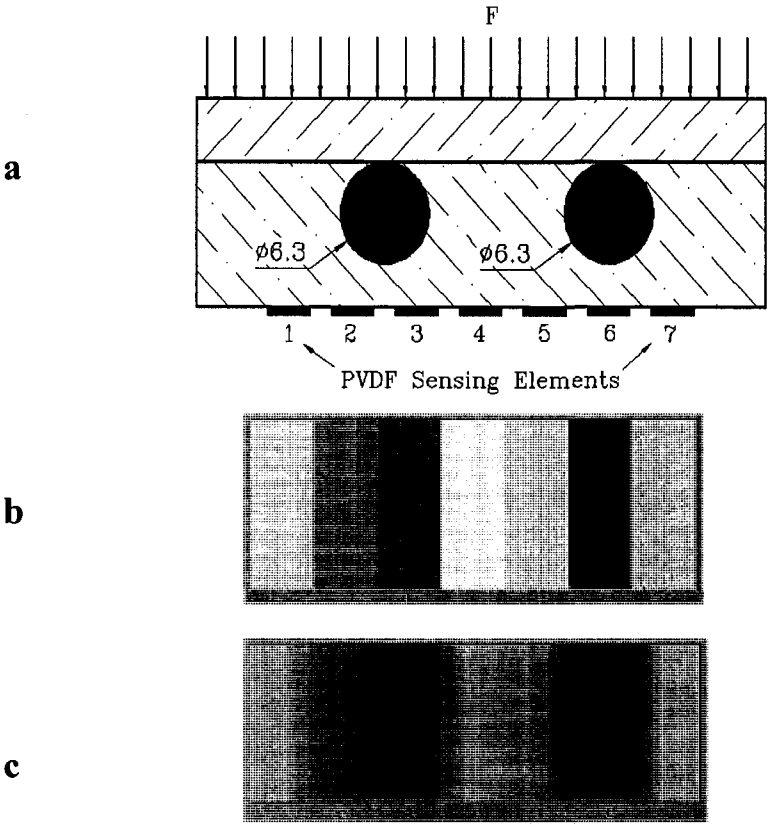

Figure 3.16. Locating the lump in one direction and its graphical rendering.

The intensity values assigned to the inserted elements were calculated using linear interpolation relationship expressed in Equation (3.10).

$$G_i = V_j + \left\{ i - 1 - (j-1)\left(\frac{N+5}{6}\right) \right\} \cdot \frac{V_{(j+1)} - V_j}{(N-1)/6} \quad , 1 + (j-1)\frac{N-1}{6} < i < 1 + j\left(\frac{N-1}{6}\right) \tag{3.10}$$

where '*j*' $(1 \le j \le 6)$ and '*i*' $(1 \le i \le N)$ are indices associated with the original vector {V} and the augmented vector {G}, respectively. The numerical example for N=60, is illustrated in Figure 3.16-c.

3.2.3.2 Graphical representation of localized lumps in two dimension

Figure 3.17, illustrates the second prototyped grasper in which both upper and lower jaws are equipped with the arrays of sensors. Using this grasper, it is possible to locate lumps in two directions, along the jaw (x-axis) as well as its depth (y-axis).

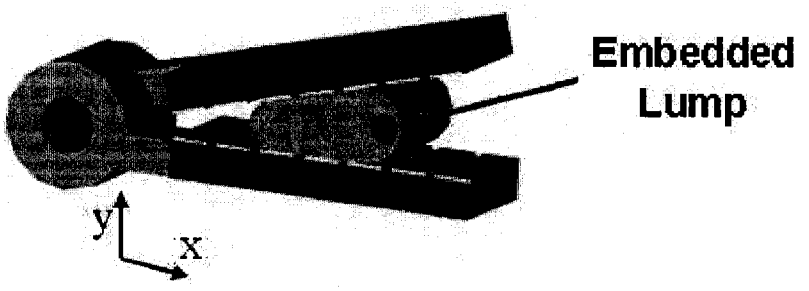

Figure 3.17. The second design of the grasper in which both upper and lower jaws are equipped with the sensing elements.

The steps used for the construction of 2D tactile images, are demonstrated in Figure 3.18.

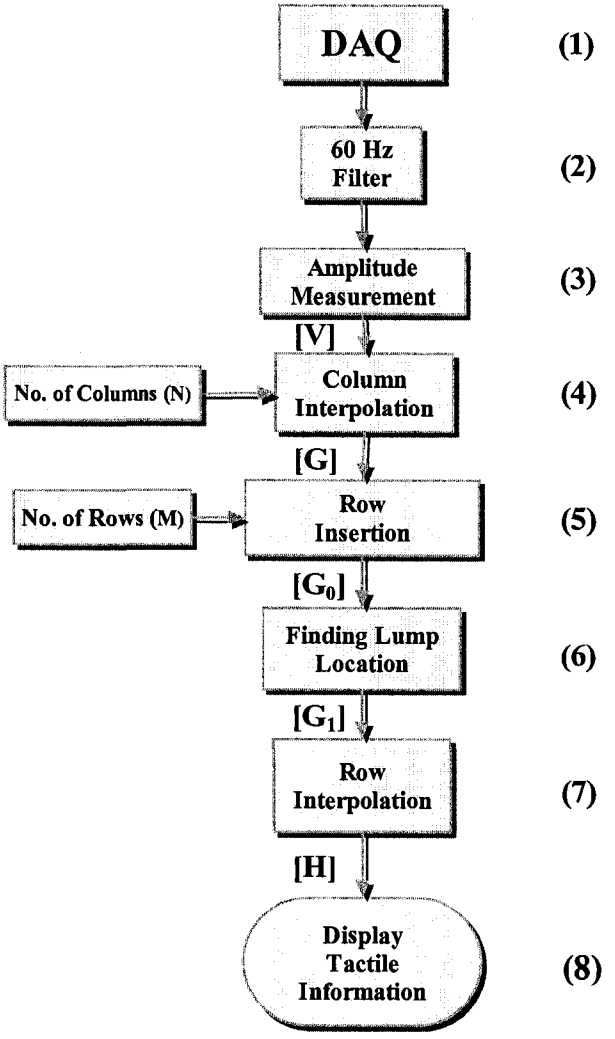

Figure 3.18. The flowchart of the algorithm implemented in LabView and used for the graphical rendering.

For better clarification of the algorithm used in this study, consider the case illustrated in Figure 3.19-a. This Figure, demonstrates a grasped tissue which contains a lump that is aligned with the sensing elements 2_U and 2_L, where the subscript U and L refer to the

Upper and Lower sensing arrays, respectively. The distance of the lump from the upper and lower sensing elements are shown by '***a***' and '***b***', respectively.

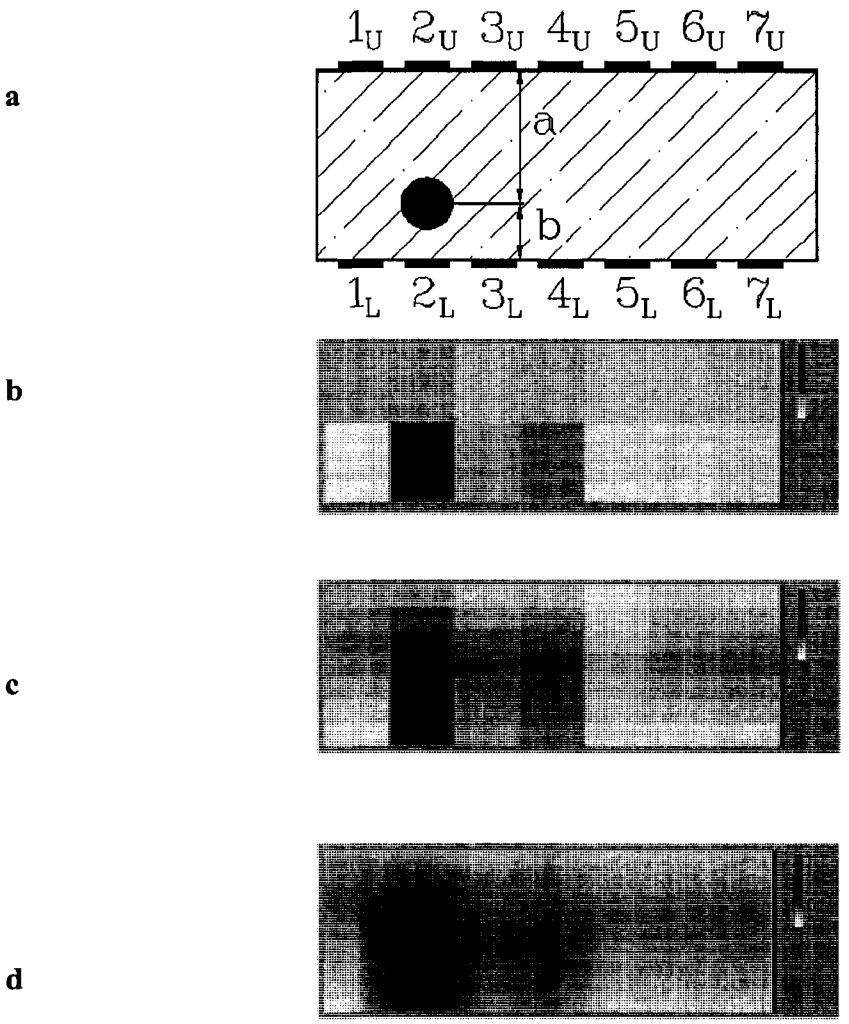

Figure 3.19. The graphical rendering of the characterized lump in two dimensions.

a) A lump located in a soft material with the upper and lower sensor arrays

b) 2D intensity graph associated with the sensor array outputs

c) A 7x7 matrix showing the location of the lump

d) A 60x100 matrix that gives a better information on location and size of the lump

Figure 3.19-b shows the 2D intensity graph which was built using one dimensional algorithm as explained in Section 4.1. This graph consists of two rows of color bands, which are corresponding with two arrays of the sensors, one on the top and the other at the bottom. Therefore, this graph can be considered as a matrix with 2 rows (color bands) and 7 columns (sensors), i.e. 2x7 cells. The corresponding matrix in which each element represents voltage amplitude is in the following form:

$$[V]=\begin{bmatrix} V_{U1} & V_{U2} & V_{U3} & V_{U4} & V_{U5} & V_{U6} & V_{U7} \\ V_{L1} & V_{L2} & V_{L3} & V_{L4} & V_{L5} & V_{L6} & V_{L7} \end{bmatrix} \tag{3.11}$$

As it can be seen, Figure 3.19-b cannot clearly demonstrate the valuable information about the location of the lump. To show the precise location of the lump, the dimensions of the matrix and consequently the number of matrix elements were increased. The graphical enhancement in x-direction was explained previous section, hence in this section the row operations (y-direction) are emphasized.

As shown in Flowchart 1 step 5, the number of rows was increased to M by inserting (***M***-2) rows of zeros between the first and second rows of matrix [V] which led to an ***M***x7 matrix. Furthermore using the technique explained in previous section 4.1, the number of columns was also increased to ***N***. The resulted ***M***x***N*** matrix $[G_0]$ would be in the form of:

$$[G_0]=\underbrace{\left.\begin{bmatrix} G_{U1} & G_{U2} & \cdots & G_{U(N-1)} & G_{UN} \\ 0 & 0 & \cdots & 0 & 0 \\ \vdots & \vdots & & \vdots & \vdots \\ 0 & 0 & \cdots & 0 & 0 \\ G_{L1} & G_{L2} & \cdots & G_{L(N-1)} & G_{LN} \end{bmatrix}\right\}M\ Rows}_{N\ Columns} \tag{3.12}$$

For the graphical representation of the lump, two parameters had to be determined, the location of the centre of lump in each column and its corresponding intensity value. In order to designate the vertical location of the center of lump in each column (step 6, flowchart 1) a relationship between the thickness of the tissue and the rows of matrix $[G_0]$ was used. If a lump is located in the tissue at a distance of ***a*** from the upper sensor array, it will be mapped into the row ***r,*** where ***r*** can be found from relationship:

$$\frac{r}{M}=\frac{a}{a+b}=\frac{G_U}{G_L+G_U} \tag{3.13}$$

in which ***(a+b)*** that is equal to the tissue thickness, was considered to be proportional to the number of rows (***M***). Regardless of existence of lump, the above equation was applied to all columns (see Figure 3.20).

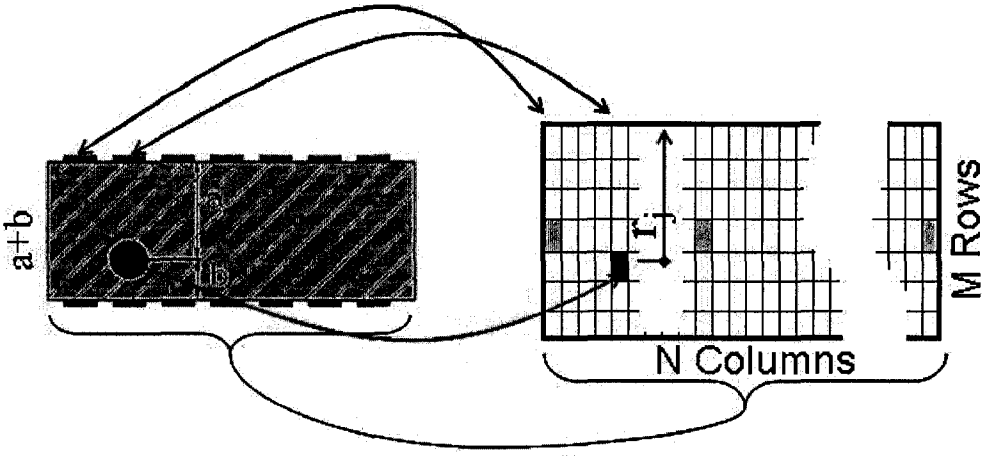

Figure 3.20. The relationship between grasped object and intensity matrix

If a lump exists in a column, then ***a*** and ***b*** are the distances of the center of the lump from the upper and lower sensor arrays, respectively. For the columns with no lump, the

associated sensor outputs are equal and $G_L = G_U$, thus $r = M/2$. These cells are indicated in Figure 3.20 with gray color. In other words, the algorithm assigns a non-zero value to the middle row of the columns with no lump. Although this value is not significant, it can be considered as a shortcoming of the algorithm.

In order to determine the intensity values of these locations in each column, the following relation was used:

$$G_{rj} = G_{Uj} + G_{Lj} \tag{3.14}$$

Where index G_{rj} specifies the intensity value of the cell located in the row ***r*** and column ***j,*** showing the center of lump in that column. The result of this operation is matrix [G_1], in which the centers of detected lumps are specified.

$$[G_1] = \underbrace{\begin{bmatrix} G_{U1} & G_{U2} & \cdots & G_{UN} \\ 0 & 0 & \cdots & 0 \\ \vdots & \vdots & & \vdots \\ 0 & 0 & \cdots & 0 \\ G_{r_1 1} & G_{r_2 2} & \cdots & G_{r_N N} \\ 0 & 0 & \cdots & 0 \\ \vdots & \vdots & & \vdots \\ 0 & 0 & \cdots & 0 \\ G_{L1} & G_{L2} & \cdots & G_{LN} \end{bmatrix}}_{N\ Columns} \Big\} M\ Rows \tag{3.15}$$

It should be noted that in case of having multiple lumps, the center of each lump is mapped to a row that corresponds to the lump's original depth in the tissue. Therefore, for instance, $G_{r_1 1}$ and $G_{r_2 2}$ are not necessarily in the same row.

As depicted in step 7 of Flowchart 1, a row interpolation procedure was implemented. At this step, in each column three values were known; G_{Ui}, $G_{r_i i}$ and G_{Li}. Therefore, using

these values and through a linear interpolation, a new intensity distribution was assigned to all zeros. The final intensity matrix $[H]$ can be represented as:

$$[H]=\begin{bmatrix} H_{11} & H_{12} & \cdots & H_{1N} \\ H_{21} & H_{22} & \cdots & H_{2N} \\ \vdots & \vdots & \vdots & \vdots \\ H_{(M-1)1} & H_{(M-1)2} & \cdots & H_{(M-1)N} \\ H_{M1} & H_{M2} & \cdots & H_{MN} \end{bmatrix} \tag{3.16}$$

where the intensity of each cell was calculated from relationship (3.17).

$$\begin{cases} H_{ij}=G_{Uj}+(i-1).\dfrac{G_{r_j j}-G_{Uj}}{r_j-1} & ,1\le i\le r_j,\ 1\le j\le N \\ H_{ij}=G_{r_j j}+(i-r_j).\dfrac{G_{Lj}-G_{r_j j}}{M-r_j} & ,r_j\le i\le M,\ 1\le j\le N \end{cases} \tag{3.17}$$

Figure 3.19-c shows the lump position and its approximate size after implementing the mentioned algorithm when M=N=7. Evidently, increasing the number of cells in both directions will enhance the quality of image. Figure 3.5-d, for instance, is the constructed graphical image based on the same sensor's output and enhancement of associated matrix to M=60 and N=100.

3.2.4 Experiments

An experimental set up was used to generate tactile information by the application of known loads through the fabricated graspers to the soft object which was contained lump. The graspers positioned under a probe which was equipped with a reference load cell, while the soft object and lump were sandwiched between two jaws. The photographs of both prototyped graspers, with one and two active jaws are shown in Figures 3.21-a,

and 21-b, respectively. Because the PVDF base sensing elements were prepared manually, the discrepancy between the output voltages for equal load was observed at the beginning. To compensate this disparity, a controllable coefficient for each sensing element was defined. Then using homogenous elastomeric materials (without any inclusion) the output of the sensors were identically adjusted. The output voltages of the sensing elements in both designs were processed and according to the explained algorithm, graphically demonstrated.

The soft elastomeric material with known Young's modulus was used as the bulk soft object and metallic balls simulating the lumps with different sizes (3.9, 6.3 and 7 mm) were inserted into the hollow spaces carved out of the bulk elastomeric. To change the depth of the lumps, several layers of the elastomeric material were cut into same dimensions but with different thicknesses. The lumps were placed in one of the layers, so that the other elastomeric layers were used as spacers to increase or decrease the distance of lump layer from the top and bottom surfaces. A dynamic load was applied by the shaker that was driven by a power amplifier and a signal generator, as shown in Figure 3.22. The outputs of the sensors were fed into the connector box through the buffer electronics. The piezoelectric PVDF can be considered as a voltage source with very high output impedance. Since the DAQ needs the input impedance to be less than 100 kΩ, a buffer was necessary to match the impedance. The data was transferred to the computer, using the DAQ (NI PCI-6225). The DAQ main amplifier was used in RSE (reference single ended) mode [101]. A low pass filter with a cut-off frequency of 40Hz was used to remove the 60Hz line noise. As explained in Section 4, the processing algorithm was

developed in LabView environment for the graphical demonstration of the forces sensed by the sensor elements.

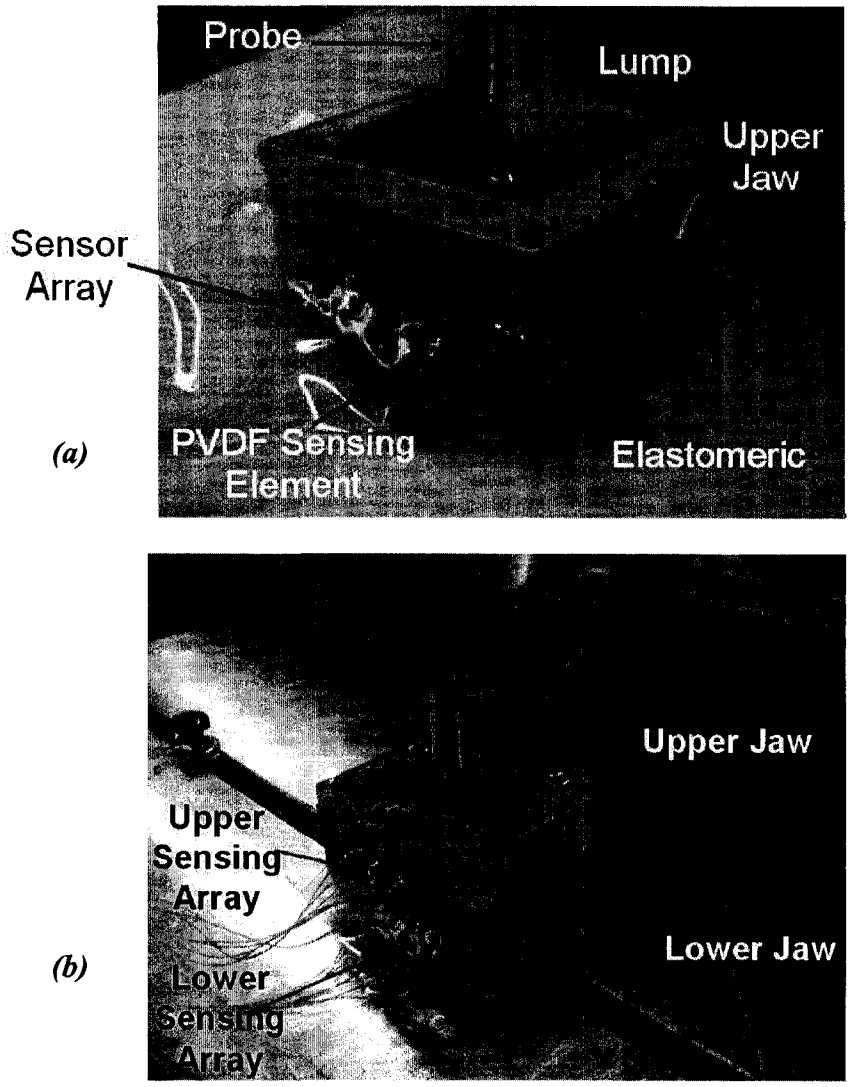

Figure 3.21. Photographs of the sensors under the test. (a) The sensor with one active jaw used for construction of one dimension graphical images. (b) The sensor with two active jaws used for two-dimension graphical rendering of detected lumps.

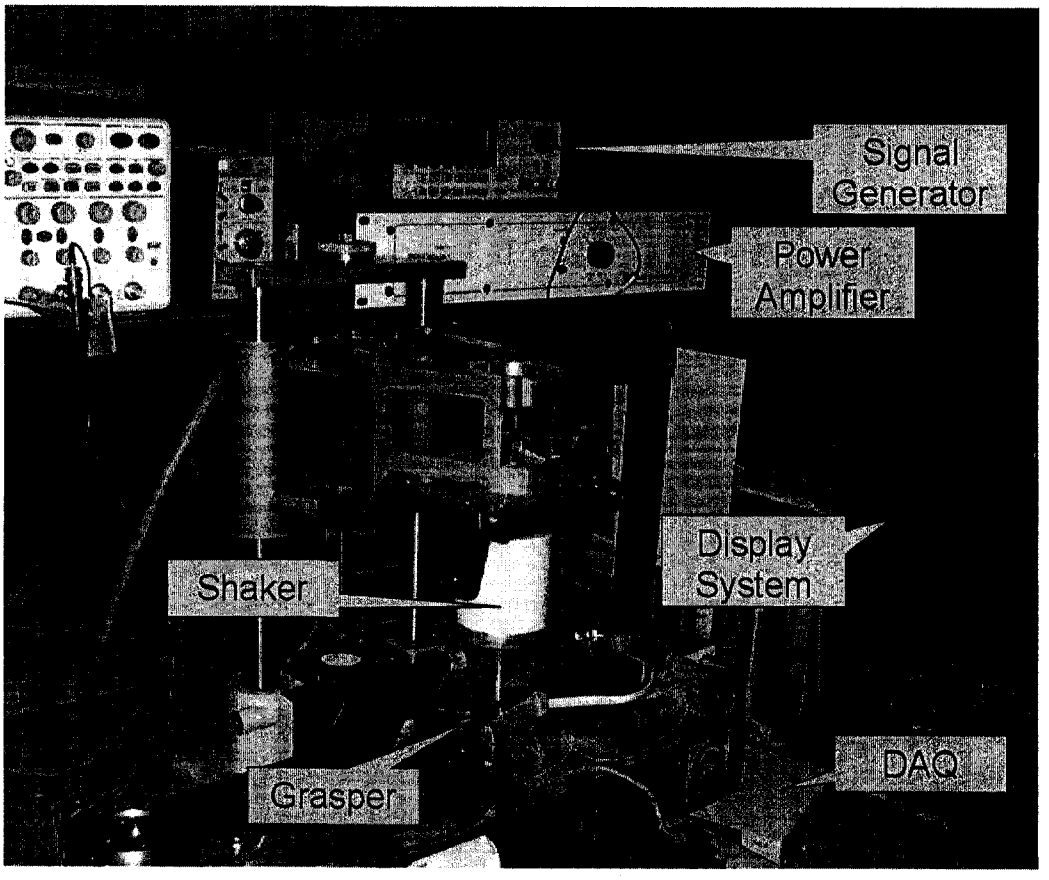

Figure 3.22. Photograph of the experimental setup

3.2.5 Results and discussion

The results of the finite element analysis as well as the graphical representations of tactile information obtained from experimental cases are shown in Figures 3.23 and 3.24 for one and two dimensional procedures, respectively. Each row in Figure 3.23 shows a scenario in which multiple lumps with different sizes were inserted into the elastomeric

bulk material. The left column in this Figure. illustrates the geometrical information about the locations and size of the lumps that were placed in the soft object. The middle column in Figure 3.23, is the one dimension graphical representation of the sensor's outputs obtained from the experiments. The right column is the normalized voltage response of the sensing elements obtained from the finite element analysis.

In the graphical representation in Figure 3.23-a (middle column), the dark column 2 has the highest intensity, showing that the lump is located above this sensing element. This can be compared with the intensity of the sensing elements 4 and 5 that share a lump. For the latter elements, the maximum contact stress value occurs in a place between the sensing elements 4 and 5. Therefore, each sensing element senses part of the load and in comparison with the sensing element 2, shows lower amplitude. These two elements also provide information about the size of the lump. If the middle lump was large enough to cover both sensing elements, the result would be two completely dark bands. Therefore, from the shown gray levels the approximate size of the middle lump can be deduced. The difference observed between the outputs of the sensing elements 2 and 7 can be attributed to the edge effect on the latter element. The second case (Figure 3.23-b) shows two identical lumps embedded above the sensing elements 2 and 5. The similar output voltage and intensity can be seen in the graphical representation as well as finite element analysis. In the third case (Figure 3.23-.c) a larger lump is placed between two smaller lumps. It is shown that the system is capable of detecting all three masses. However the darker band associated with the sensing element 4, gives information on the relative size of middle lump respect to the other ones. In the last case, (Figure 3.23-d), a small lump had been positioned between two larger lumps. As can be seen from the

results, the sensor has not been able to detect the smaller mass. A closer examination of finite element stress distribution shows that two larger lumps created a stress profile between themselves in such a way that the effect of the small mass has been suppressed. This Figure demonstrates that for multiple lumps with different sizes and locations, to obtain an accurate result more than one attempt and in different orientations might be needed.

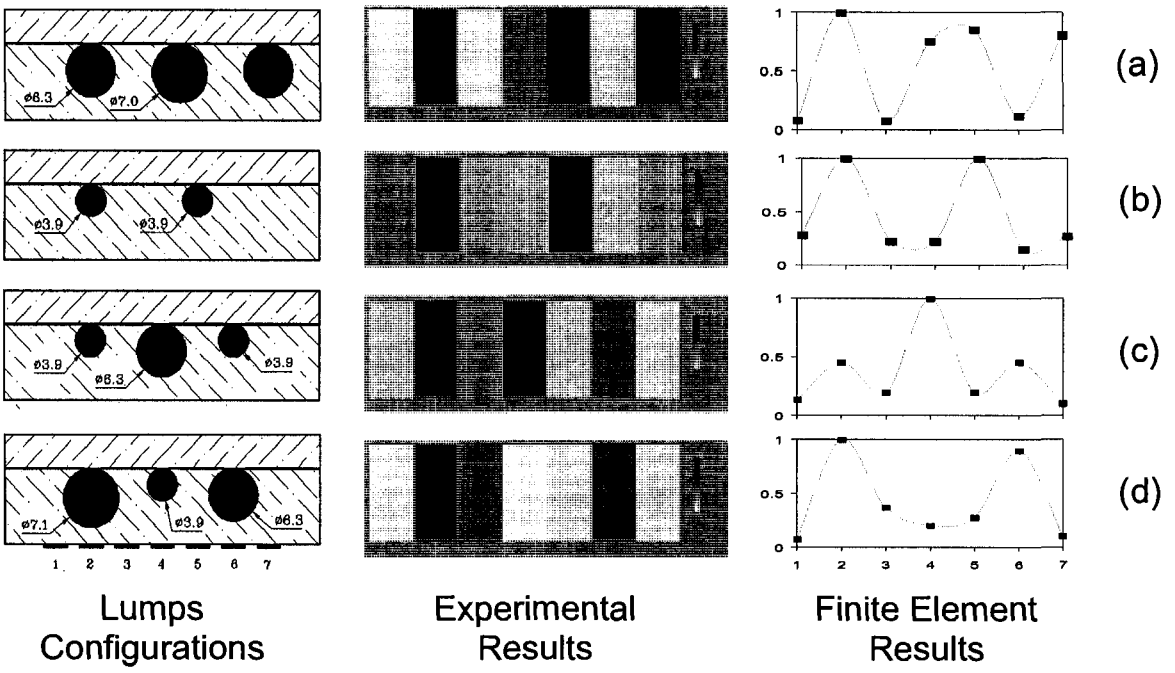

Figure 3.23. The experimental and analytical results of four case study.

Figure 3.24, alternatively shows the results of four case studies in which both jaws of the graspers were equipped with arrays of the sensing elements. Figure 3.24-a, demonstrates a case in which two identical lumps were positioned close to the sensing elements 1 and 4 of upper jaw (1_U and $4_{U)}$, respectively. The corresponding graphical image shows clearly

the place of the lumps. In addition, the gray level of image gives some information about the size of the lumps.

In the next configuration (Figure 3.24-b), lumps are positioned apart in such a way that one lump is put beneath the sensing element 4_U and the second lump is placed above the sensing element 1_L (slightly overlapped with sensing element 2_L). The graphical image constructed based on the experimental sensor's output is shown in middle column of Figure 3.10-b, in which the place (in x and y directions) is clearly extractable. The gray levels in this case can be compared with those of Figure 3.24-c, in which the lumps positioned far from the sensing elements.

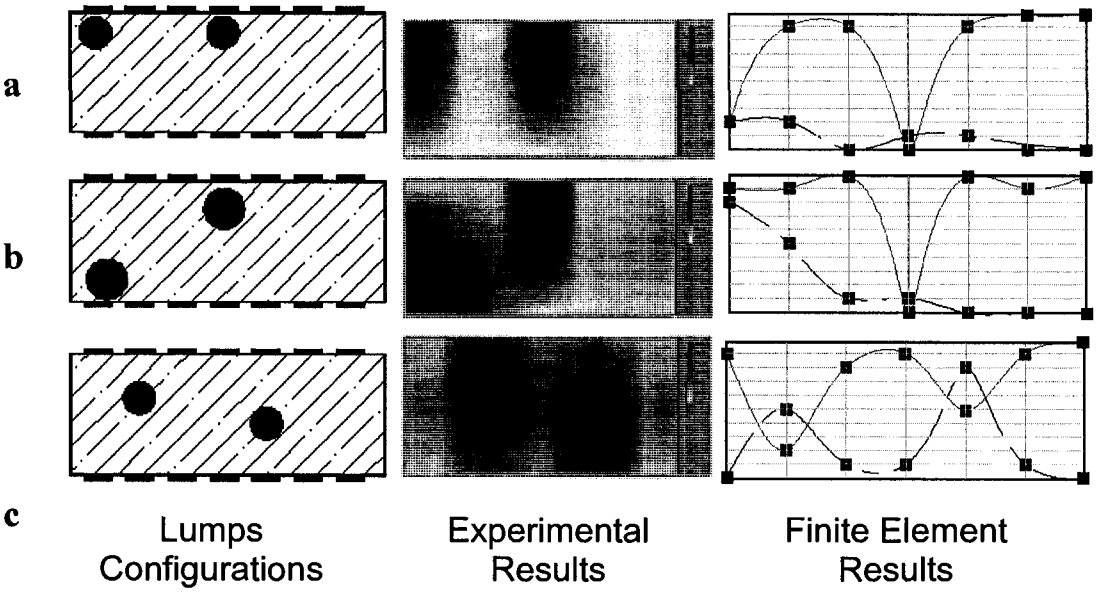

Figure 3.24. The experimental and analytical results for two dimensional localization. Each row illustrates the information of the studied case. In the right column, the dashed line represents the output voltages of the lower array of the sensors, while the solid line is associated with the upper jaw.

Again the position and size of lumps can be clearly perceived from the experimental data shown in the middle column. The finite element results shown in the right column are consistent with the experimental data in all three cases. However, implementation of this algorithm may produce gray areas in the middle of image in absence of any lump. To rectify this problem, an enhanced algorithm is under process.

3.3 Summary and conclusions

An MIS grasper capable of measuring the softness of the grasped objects is reported in the first part of this chapter. A feedback system is designed and incorporated in the sensor arrays assembly on the grasper jaws. This allows the transmission of the tactile signals from the grasper to the signal processing system. Following this step, we developed the signal processing and display system. By doing so, we managed to obtain the graphical representation of the tactile data on a computer monitor. The resulting data include the tissue softness on the tissue/grasper interface. Finally, the testing of the grasper device with its feedback and tactile graphical representation systems was performed and the results were discussed.

In the next part of this chapter, a system for characterizing and rendering the hidden lumps in soft bulk objects is presented. The proposed system is comprised of an endoscopic grasper equipped with array(s) of tactile sensors, a signal processing unit, graphical rendering algorithm and a graphical display. This setting potentially could be used for nodule detection in laparoscopic surgery.

Initially the required information has to be collected from the grasped object. This task has been performed by using a multifunctional tactile sensor that had already been

developed. A unit of the utilized sensor is capable of measuring the applied contact force as well as the softness of the grasped object. An array of this sensor used in this study, is capable of reporting the location and size of the lump as well. The output voltages of the sensing elements are buffered, digitized, filtered and transmitted to a computer. Then through a rendering algorithm developed in LabView environment, the tactile data were transformed to gray scale image and were displayed on a monitor.

The experiments on the prototyped graspers were conducted and the data were graphically rendered on a display. Hard objects were inserted into pre-determined positions in elastomeric and were grasped by the device and the calculated images were compared with the known ones.

Graphical rendering of localized objects is a feasible technique with great potential for use in MIS. Using this method a part of lost tactile information which is the palpation can be restored. This capability is useful not only for MIS, but also for MIS robotic surgery and, in general, for robotic surgery. Other anatomical features such as beating arteries potentially could be detected and graphically rendered.

CHAPTER 4

LINEAR ACTUATOR FEEDBACK BASED TACTILE DISPLAY

In this chapter, a new tactile display is developed which can reconstruct the softness of different materials based on the characteristics properties of these materials. From a simplistic point of view, most materials can be modeled by a spring. In small strains, this model can be good for characterizing the softness of the material. However, when the strain goes higher, the spring model can not model the behavior of the material. The reason is that the behavior of the material in high strains is not linear. Most tactile displays which are driven by the servomotor or any kind of actuation use the spring model to simulate the softness. In this research work, the non-linear behavior of the materials is considered to describe the softness.

4.1 System Design

A linear actuator has been used as a softness display. The basic idea is to measure the force applied by the finger to the linear actuator shaft, calculate the displacement of the shaft in response to the applied force according to the mechanical properties of the simulated material, and move the shaft to the calculated position.

A force sensor is used to measure the applied force by the finger to the tip of the shaft. The measured force is registered by the data acquisition card and read by the processing software. The position of the shaft is also measured and transmitted to the processing software through the data acquisition card. The mechanical properties of the

object to be simulated have been already determined and saved in the computer. These data contain the strain-stress relation for different objects. Having the force applied to the linear actuator by the fingertip and the dimensions of the cap over which the force is applied, the stress is calculated and the desired strain can be found by using the characteristic curve of the simulated object. The desired strain is then converted to the displacement and used as the input to the PID controller.

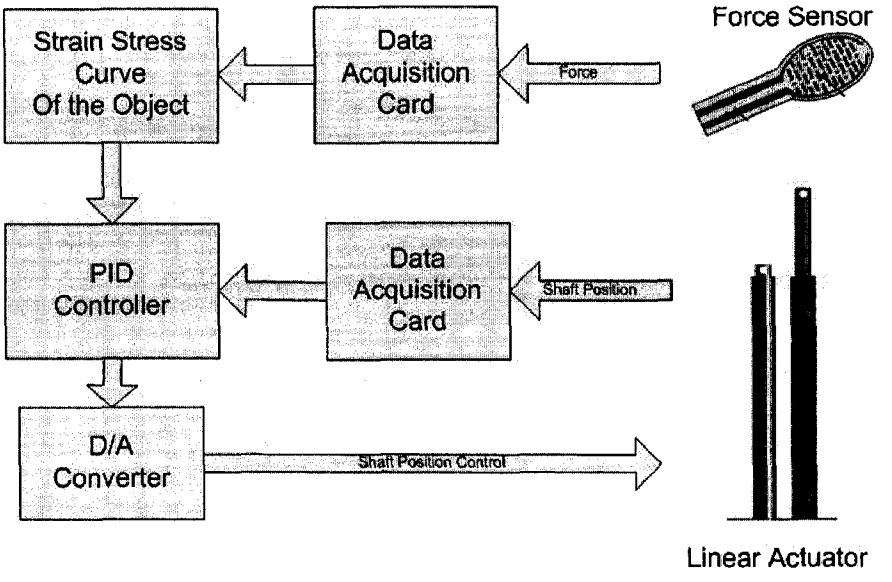

Figure 4.1. Block diagram of the tactile display

Having the desired position of the shaft and the actual position, the PID controller prepares the control commands for the actuator and transmits them to the driver circuit. Figures 4.1 shows the block diagram of the system. A photo of the tactile display is shown in Figure 4.2.

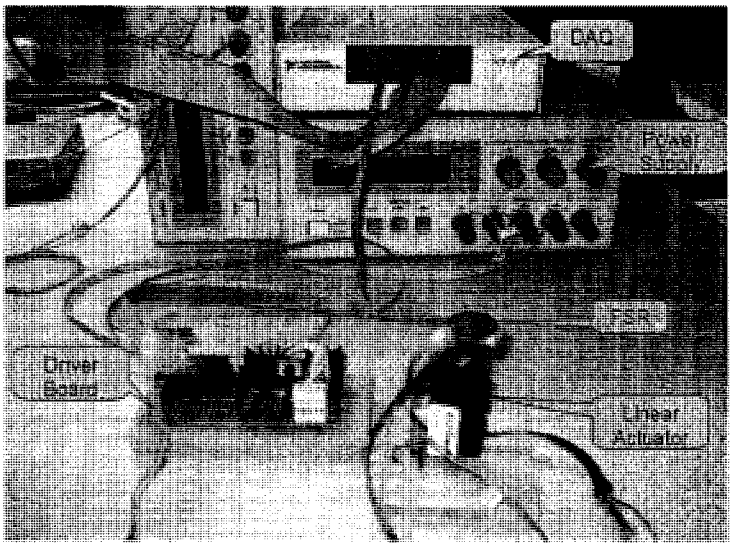

Figure 4.2. Photo of the tactile display including: linear actuator, Force Sensitive Resistor (FSR) , Data acquisition card (DAQ) and driver circuit.

4.2 Linear Actuator

The tactile display shown in Figure 4.3 is made of a combination of a linear actuator, plexiglas cap, force sensor, shaft position sensor and current driver electronics. The shaft of the actuator is able to move up to 2 cm in vertical direction.

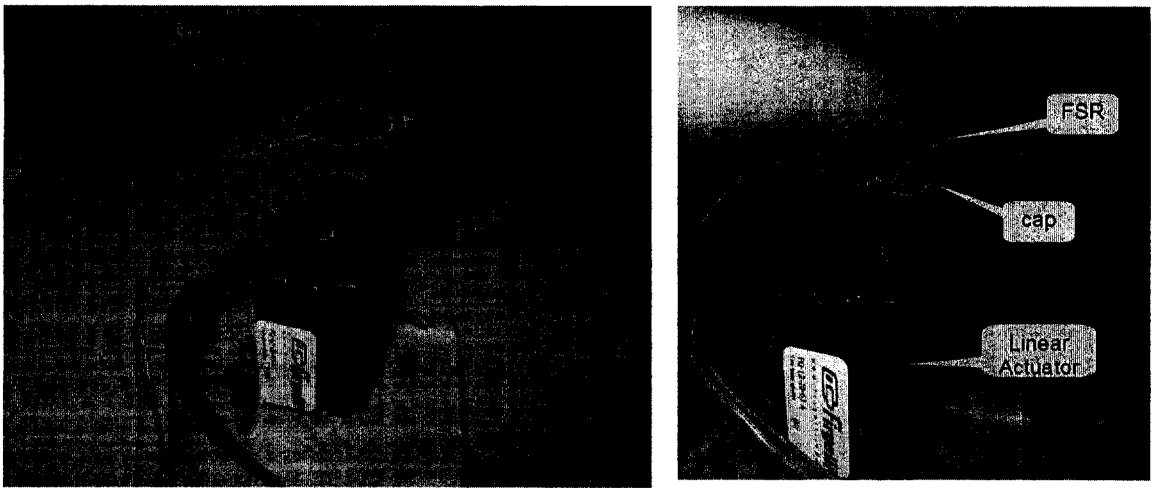

Figure 4.3. The linear actuator, FSR and plexiglas cap

It can apply a force up to 30N. The cap is glued to the tip of the shaft. It can resist to the pressure to a load up to 40 N. A force sensor which is placed on the cap can measure the force applied by finger to the shaft. A position sensor is used to measure the position of the shaft. It can measure the position with an error less than 0.5 mm. The linear actuator (from Firgelli Technologies Inc.) has the specifications presented in Table A-1 (appendix A). The dimensions, load curve, and the electrical diagram of the actuator are shown in Figure A-2.

4.3 Force Sensor

Force Sensing Resistor (FSR) is a polymer thick film (PTF) device which exhibits a decrease in resistance with an increase in the force applied to the active surface. Its force sensitivity is optimized for use in human touch control of electronic devices. FSRs are not a load cell or strain gauge, though they have similar properties. Figure B-1 and B-2 (Appendix B) demonstrates the structure of the sensor and its different components.

To experimentally determine the force-conductance relation for the FSR, several different standard weights are placed on the active area of the FSR and its conductance is measured. The results are shown in Table 4.1.

Table 4.1. Experiment results for determining force-conductance relation

Force (gr)	0	00	00	00	*00*	00	00	00	00
Conductance (1/KΩ)	.0733	.1518	.2151	.2603	.3589	.4611	.5314	.6217	.6774

The data plotted in Figure 4.4 shows that the conductance in FSR is almost linearly related to the applied force.

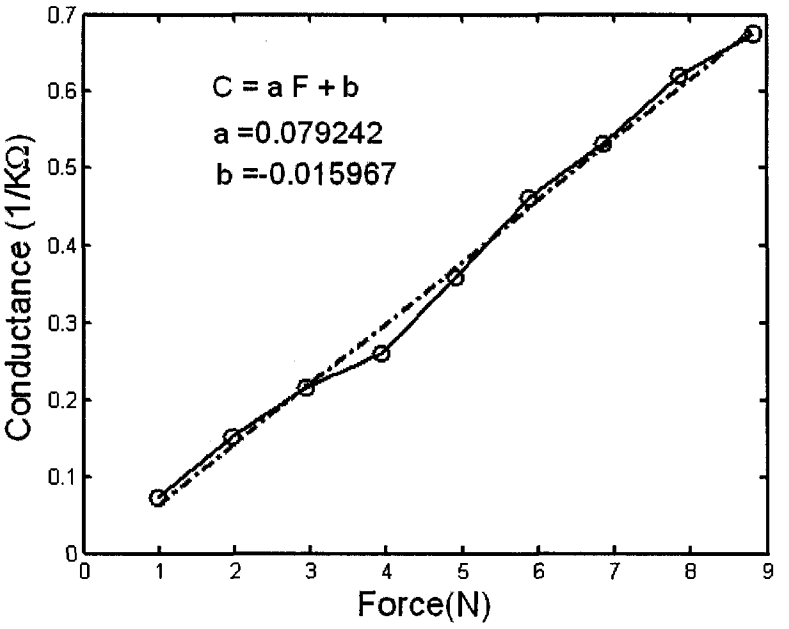

Figure 4.4. The conductance of the FSR versus Force

Fitting a line on the experimental data, the following equation can be used to relate the conductance (C) and force (F).

$$C = a.F + b \tag{4.1}$$

where a=0.079, b=0.016 .

To find the resistance of the FSR, we used the electric circuit shown in Figure 4.5.

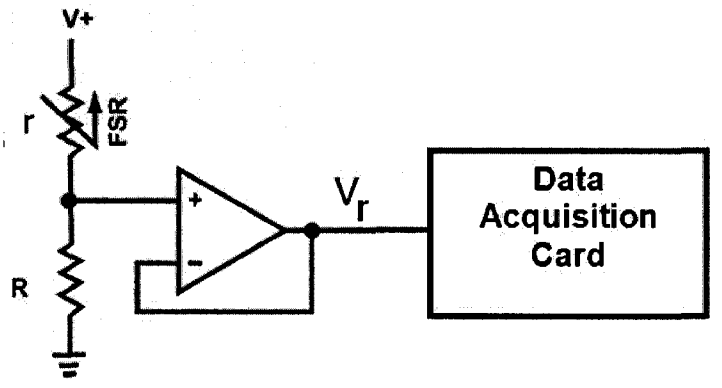

Figure 4.5. The electric circuit for measuring the resistance 'r'

In this figure the conductance of the FSR can be calculated from equation (4.2).

$$V_r = \frac{R}{R+r}V^+ \Rightarrow C = \frac{1}{r} = \frac{1}{(\frac{V^+}{V_r} - 1)R} \tag{4.2}$$

By combining equations (4.1) and (4.2) we can find a relationship between the force and voltages V_r and V^+.

$$F = \frac{1}{(\frac{V^+}{V_r} - 1)R.a} - \frac{b}{a} \tag{4.3}$$

where a=0.079, b=0.016, R=10KΩ, and $V^+ = 5^v$.

The voltages V_r and V^+ are transmitted to the data acquisition card and the force is calculated by the processing software from equation 4.3.

4.4 Shaft position sensor

A built-in linear potentiometer is used to find the position of the shaft. The relationship between resistance of the potentiometer and the length of the shaft is plotted in Figure 4.6.

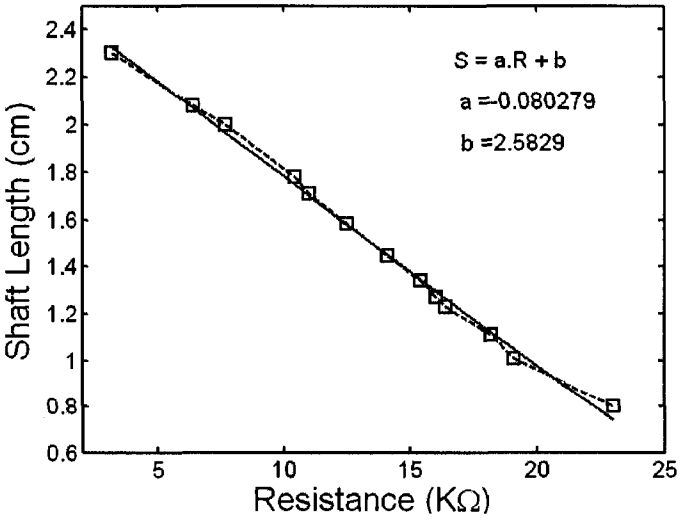

Figure 4.6. The relationship between shaft length and resistance

Using the linear relation of the shaft length and resistance, the position of the shaft can easily be determined by measuring the resistance of the potentiometer. To measure the resistance, an electric circuit similar to Figure 4.5 is used. The only difference is that the FSR is replaced by the potentiometer. The relation between shaft length (l) and the measured voltage (V_s) can be found similar to equation 4.3:

$$l = \frac{1}{(\frac{V^+}{V_s} - 1)R.a} - \frac{b}{a} \tag{4.4}$$

where a=0.080279, b=2.5829, R=10KΩ, and $V^+ = 5^v$.

Therefore the applied force (F) and the displacement of the shaft (l) can be found using relations 4.3 and 4.4.

4.5 Stress-Strain curves

When the force is applied to a material, its form is changed and when the force is removed, the material returns to its primary form. The relation between the applied force per unit of area (stress) and the percent of deformation (strain), which is nonlinear, is known as stress-strain curve. This curve can be determined for any material using mechanical compression tests. For this project, the mechanical properties of several materials were determined using mechanical compression test. Figure 4.7 shows the results of this test for different materials.

Each row in this figure shows an elastomeric material. The left column shows the stress-strain curve. Having the dimensions of the test materials, the force and deformation can be calculated from the stress and strain. The right column shows the real force-displacement relation for the same material and the same test. These force-displacement

relations are used in this project to simulate the same elastomers behavior with the linear actuator.

a) A2(3.4")

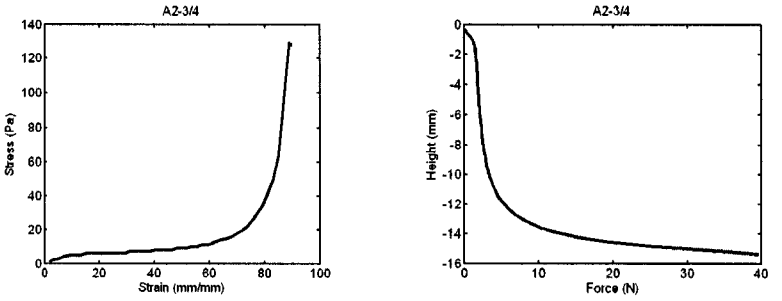

b) EVA(1/2")

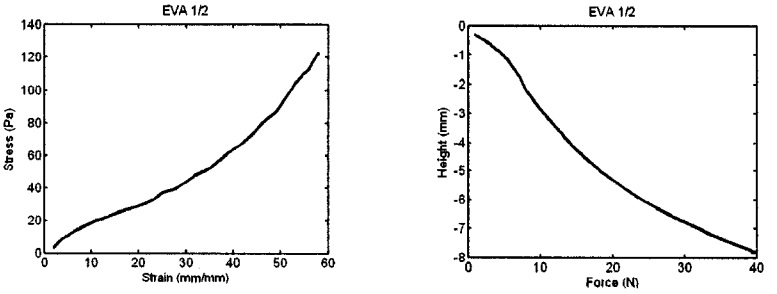

c) ICF400(1")

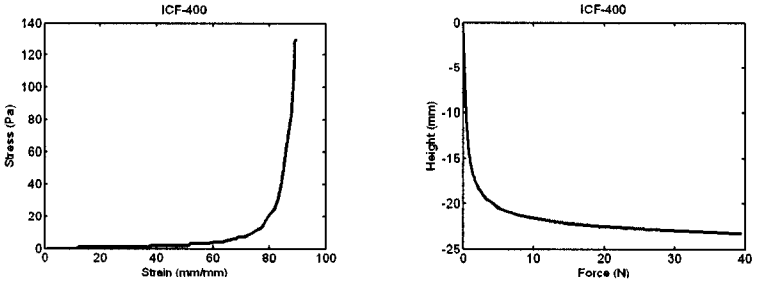

d) B1(3/4")

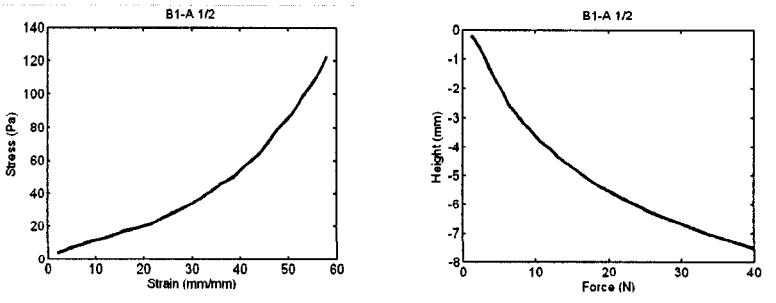

Figure 4.7. Mechanical compression test results for elastomeric material, left column: Stress-Strain relation, right column: Force, displacement relation

4.6 Data acquisition Card

NI-6225 is used for data acquisition. The sampling rate is selected 1000 sample/sec. Three channels are used in SRE mode to gather information. To avoid the interference between the channels, a buffer is used for each channel.

4.7 PID controller

To simulate the behavior of these elastomers, the linear actuator must follow the force-compression relation of the elastomers. In other words, the Young's modulus of elastomers is simulated by the actuator. To do so, a negative feedback closed-loop control system with feed-forward PID controller is used. The PID controller monitors the position of the shaft, compares this position with the desired position of the shaft and prepares proper commands to the actuator to move the shaft to the desired position.

To be able to design a controller for the system, a model for the linear actuator must be found. Figure 4.8 shows the block diagram of the system.

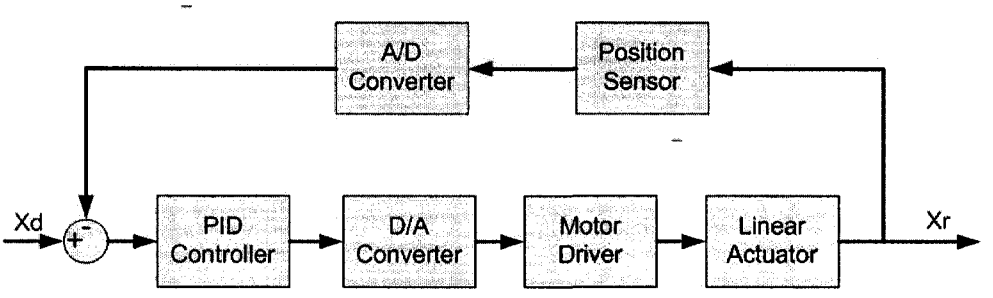

Figure 4.8. Complete block diagram of the system

For simplification, we neglect some of the blocks like position sensor, ADC and DAC. These blocks are linear and operate as a simple unity gain. To find the transfer

function for the linear actuator and the driver circuit, the PID controller is replaced by a unity gain. Figure 4.9 shows the simplified block diagram of the linear actuator and the driver.

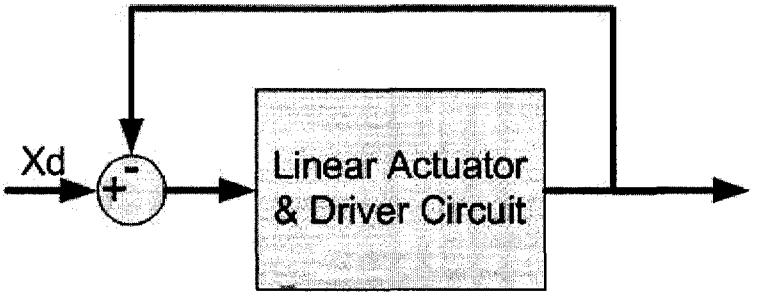

Figure 4.9. Simplified block diagram of the system

4.7.1 Linear Actuator Model

To identify the parameters in the transfer function of the actuator, a sinusoidal wave with the unity gain and variable frequency is applied to the system. The frequency was changed over the range of 0- 5Hz and the magnitude ratio between the output of actuator and input sinusoidal signal and also the time delays for each input are registered. Then using the experimental data, the Bode plot of the system is traced out and is shown in Figure 4.10.

The transfer function of the actuator can be considered as a second order system. The general form of a second order system is:

$$G(s) = \frac{k\omega_n^2}{s^2 + 2\zeta\omega_n s + \omega_n^2} \tag{4.5}$$

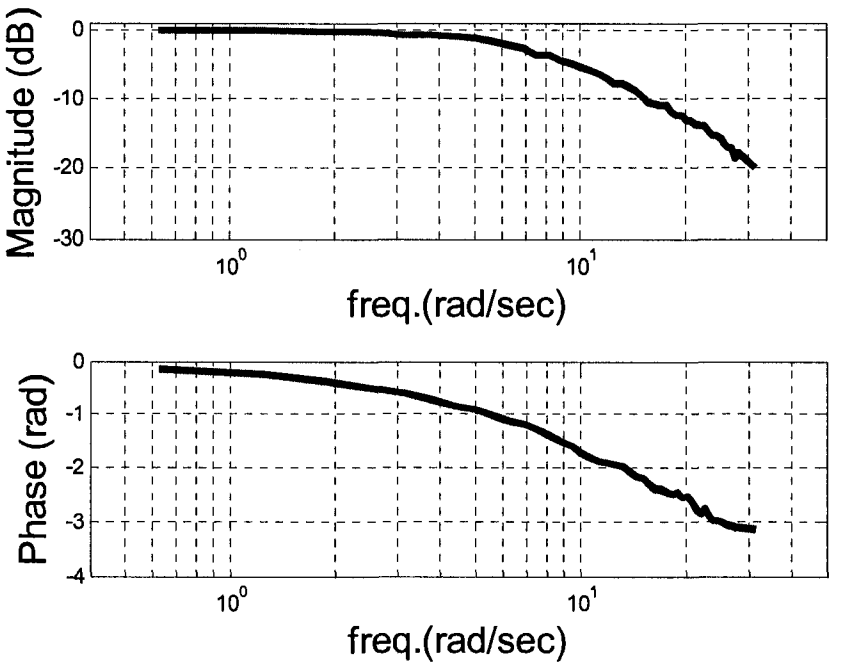

Figure 4.10. Frequency response of the system

The parameters of the second order system can be derived from the Bode plot as below (please refer to Appendix C):

$$\begin{cases} DC\ gain = k = 10^{\frac{M(0)}{20}} \\ M(0) = 0 \end{cases} \Rightarrow k = 1 \tag{4.6}$$

$$\begin{cases} \omega_n = \omega_{-90^\circ} \\ \omega_{-90^\circ} = 9.3 \end{cases} \Rightarrow \omega_n = 9.3 \tag{4.7}$$

$$\begin{cases} \zeta = K / (2 * 10^{\frac{M_{-90^\circ}}{20}}) \\ M_{-90^\circ} = 20 \log(0.4) = -7.96\ dB \end{cases} \Rightarrow \zeta = 1/(2*10 - 0.4) = 1.26 \tag{4.8}$$

Therefore the transfer function of the system is:

$$G(s) = \frac{86}{s^2 + 2(1.26)(9.3)s + 86} = \frac{86}{s^2 + 23.4s + 86} \tag{4.9}$$

Please note that G(s) is the transfer function of the closed-loop system. To find the open loop transfer function, H(s), consider Figure 4.11.

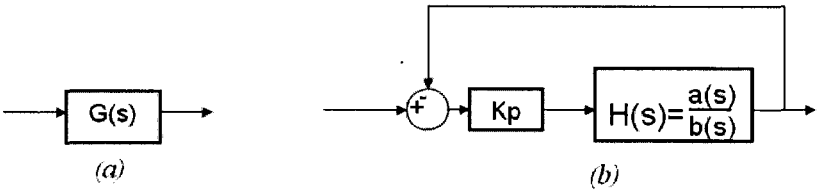

Figure 4.11: Closed-loop system and its equivalent transfer function

In this figure, the closed loop transfer function of the system is:

$$H(s) = \frac{a(s)}{b(s)} \Rightarrow G(s) = \frac{K_p.a(s)}{b(s) + K_p.a(s)} \tag{4.10}$$

In the experiments, we set $Kp = 1$. Therefore H(s) can be easily derived from G(s):

$$G(s) = \frac{a(s)}{b(s) + a(s)} = \frac{86}{s^2 + 23.4s + 86} \Rightarrow H(s) = \frac{a(s)}{b(s)} = \frac{86}{s^2 + 23.4s} \tag{4.11}$$

4.7.2 Verifying the Identification Results

To verify the identification results which are obtained in the frequency domain, a step input is applied to the system and the time response of the position of the linear actuator is checked. Figure 4.12 shows the response of the system to a step input.

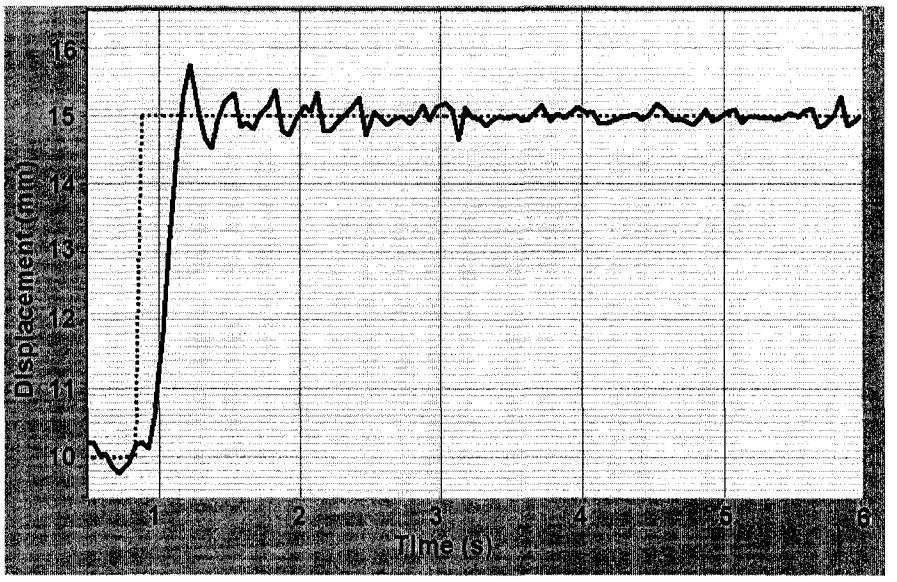

Figure 4.12. The response of the system to a step input

In this figure, the overshoot can be calculated as:

$$OS = \frac{0.7}{5}.100 = 14\% \tag{4.12}$$

And ζ can be calculated:

$$\zeta = \frac{-\ln(0.14)}{\sqrt{\pi^2 + (\ln(0.14))^2}} = 0.53 \tag{4.13}$$

Using the following relationship, ω_d and ω_n can be found:

$$\omega_d = \frac{2\pi}{\Delta t}, \Delta t = Peak - to - Peak \ \ time, \tag{4.14}$$

$$\Delta t = 0.3\text{sec} \Rightarrow \omega_d = \frac{2\pi}{\Delta t} = \frac{2\pi}{0.3} = 6.67\pi \tag{4.15}$$

$$\omega_n = \frac{\omega_d}{\sqrt{1-\zeta^2}} = \frac{6.67\pi}{\sqrt{1-0.53^2}} = 24.7 \tag{4.16}$$

$$G(s) = \frac{24.7^2}{s^2 + 2(0.53)(24.7)s + 24.7^2} = \frac{610}{s^2 + 26.2s + 610} \tag{4.17}$$

Now the transfer function H(s) is calculated:

$$G(s) = \frac{k_p a(s)}{b(s) + k_p a(s)} \tag{4.18}$$

$$k_p a(s) = 361\,,\ k_p = 7 \Rightarrow a(s) = 87 \tag{4.19}$$

$$H(s) = \frac{a(s)}{b(s)} = \frac{87}{s^2 + 26.2s} \tag{4.20}$$

Relationships 4.11 and 4.20 which were driven using two different experiments are very close to each other. A small error exist between the two relations is considered to be normal due to the nonlinearities in the linear motor.

4.7.3 PID Controller

A PID controller can be designed in several ways; most of them can be classified in the following categories [102]:

4.7.3.1Classical synthetic open-loop design

In synthetic method, the designer starts with a simple controller and continues to add more term to the controller action, in the hope that after some number of additions the controller will meet the design goals. In other words, the controller is "built up: piece by piece, possible using a variety of "tools" at different stages [103-106].

4.7.3.2 Analytic state-space methods

An analytic method, on the other hand, is based on an analytic solution of some optimal controller design problem, for example, the Linear Quadratic Gaussian (LQG) problem [107-109].

4.7.3.3 Parameter optimization methods

Parameter optimization methods for LTI feedback design start with controller structures that are motivated by ideas from classical, modern, or other techniques. What is generally meant by controller structure is a system model with one or more parameter values that can be adjusted. A simple example is a PI (proportional-plus-integral) controller structure- the coefficients K_p and K_i in the controller transfer function K_p+K_i/s are the parameters

The next step in a parametric method is to select a cost function that represents the quality of system performance. One way to get a cost function is to take one from an analytically solved optimization problem, for instance the LQG (Linear-Quadratic Gaussian) problem. This has advantage that the cost yielded by the structured controller by parameter search can then be compared to the absolute minimum achieved by any controller, which is analytically computable.

Another possible way to obtain a cost function is to form a weighted sum or maximum of various performance indices, such as integrated square error in response to a step command, integrated magnitude of frequency response across some band where a disturbance is concentrated, some indices representing the actuator use, and so on; the idea is that the weights define the relative importance of different aspects of system performance. Finally, the designer may add explicit constraints, such as bounds on the values of the parameters, bounds on closed-loop pole locations, bounds on open-loop frequency responses, and so on.

After a controller structure is determined, a cost function and possibly some constraints have been specified, the designer has to solve a nonlinear optimization

problem which almost certainly requires numerical solution. Many techniques for numerical solution of optimization problems resulting from control design problems have been proposed in the control literature [110-115]. Some of these techniques are simple heuristic algorithms, such as steepest descent; some are highly specialized algorithms for certain kinds of problems; others are sophisticated software packages for handling very general classes of problems. It is beyond the scope of this thesis to provide a comprehensive overview of parameter optimization methods.

4.7.3.4 Controller design

For the special system explained in this chapter the position of the shaft and the applied force by the finger to the shaft follow the desired force-position curve as close as possible. To minimize this tracking error, the optimum controller design method is used to find the best possible PID controller.

4.7.3.5 Solving the problem in Simulink

The plant is a second order linear system shown in Figure 4.13. The closed loop system including the actuator and the PID controller is shown in Figure 4.14

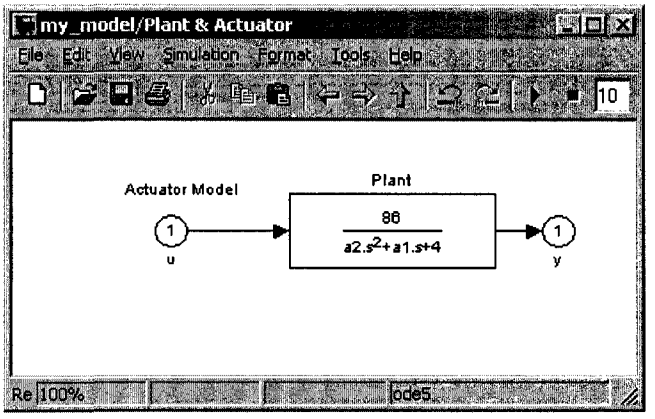

Figure 4.13. The plant is a second order linear system.

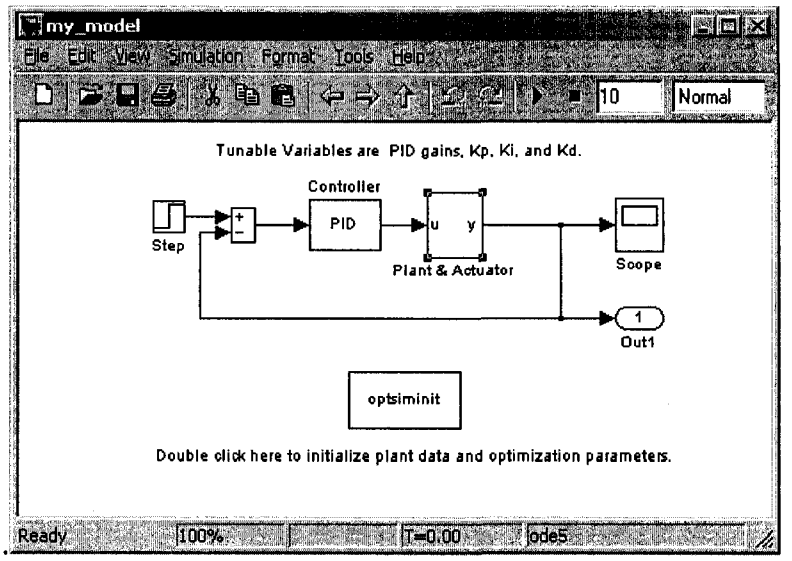

Figure 4.14. The closed loop system

The error is defined as the difference between step input and output. The cost function to be minimized (J) is the total square error from 0 to 100 seconds (see relationship (4.21).

$$J = \int_0^{100} [y(t) - u(t)]^2 dt \tag{4.21}$$

The variables are the parameters of the PID controller.

$$J(K) = J(K_P, K_I, K_D) \tag{4.22}$$

where $K=[K_P, K_D, K_I]$.

In discrete case the equation (4.21) is written as:

$$J(K_P, K_I, K_D) = \sum_{k=1}^{N} [y(k) - u(k)]^2 \quad ; \quad k = 1, \ldots, N \tag{4.23}$$

where

$$N = \frac{100}{T_s} \tag{4.24}$$

N is the total number of samples in 100 seconds and Ts is the sampling period.

Having the number of samples (N) and sampling period (Ts), the objective of optimization problem is to find PID controller parameters (K_P,K_D,K_I) for which J(K) is minimized.

$$\underset{K_I,K_P,K_D}{Min}\ J(K) \tag{4.25}$$

The Matlab routine "*lsqnonlin*" is used to perform least-squares fit on the tracking of the output. The tracking is performed via an M-file function "*tracklsq*", which returns the error signal, the output y_{out} computed by calling "*sim*", minus the input signal 1(unit step). The code for "*tracklsq*" is shown in the appendix D.

The function "*runtracklsq*" sets up all the needed values and then calls "*lsqnonlin*" with the objective function "*tracklsq*", which is nested inside "*runtracklsq*". The variable options passed to "*lsqnonlin*" defines the criteria and display characteristics. In this case the medium-scale algorithm is used, and termination tolerances for the step and objective function are given on the order of 0.001.

To run the simulation in the model "*optsim*", the variables K_p, K_i, K_d, a_1, and a_2 (a_1 and a_2 are variables in the Plant block) must all be defined. K_p, K_i and K_d are the variables to be optimized. The function "*tracklsq*" is nested inside "*runtracklsq*" so that the variables a_1 and a_2 are shared between the two functions. The variables a_1 and a_2 are initialized in "*runtracklsq*".

The objective function "*tracklsq* "must run the simulation. The simulation can be run either in the base workspace or the current workspace, that is, the workspace of the function calling "*sim*", which in this case is the workspace of "*tracklsq*". In this example, the "*simset*" command is used to tell "*sim*" to run the simulation in the current workspace by setting '*SrcWorkspace*' to '*Current*'. A solver for "*sim*" can be also chosen using the "*simset*" function. The simulation is performed using a fixed-step fifth-order method to 100 seconds.

When the simulation is completed, the variables t_{out}, x_{out}, and y_{out} are now in the current workspace (that is, the workspace of "*tracklsq*"). The "*Outport*" block in the block diagram model puts y_{out} into the current workspace at the end of the simulation. When you run runtracklsq, the optimization gives the solution for the proportional, integral, and derivative (K_p, K_i, K_d) gains of the controller after 20 function evaluations.

Iteration	**Func-count**	**Residual**	**Step-size**	**derivative**	**Lambda**
0	4	1.01742			
1	12	1.00068	1.55	-0.00303	1.00024
2	20	1.00007	1.35	-8e-007	0.243569
Kp = 0.9236					
Ki = 0.1654					
Kd = -0.0095					

4.8 Processing Software

The processing software which is written in the LabView environment, receives the feedback signals from FSR and linear potentiometer (Figure 4.15). After filtering these signals and removing 60Hz noise, the force (F) and shaft position (Xr) are calculated in separate modules using relationships (4.3) and (4.4). Then the calculated

force is used to find the strain for the simulated material which is saved in a lookup table (LUT).

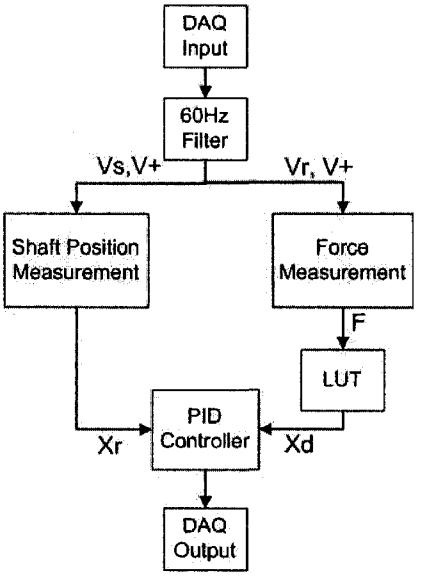

Figure 4.15. The flowchart of the processing software

Having the dimensions of the material to be simulated, the stress is transformed to compression (Xd). Then the shaft position and desired compression (Xr and Xd) are fed to the PID controller. The output of the controller is finally transmitted to the output.

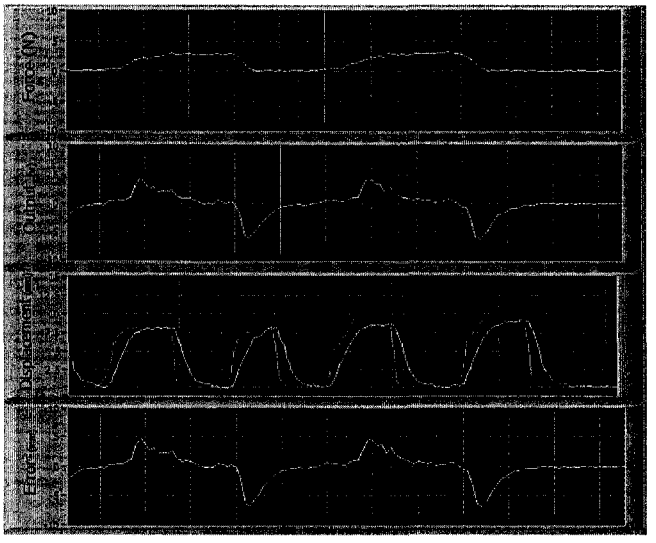

Figure 4.16. Measured and calculated signals plotted on real time

Figure 4.16 shows these parameters which are plotted in LabView. The force, shaft displacement, desired displacement, displacement error and the output are sketched in real time. Figure 4.17 shows the programming environment and block diagram of the system.

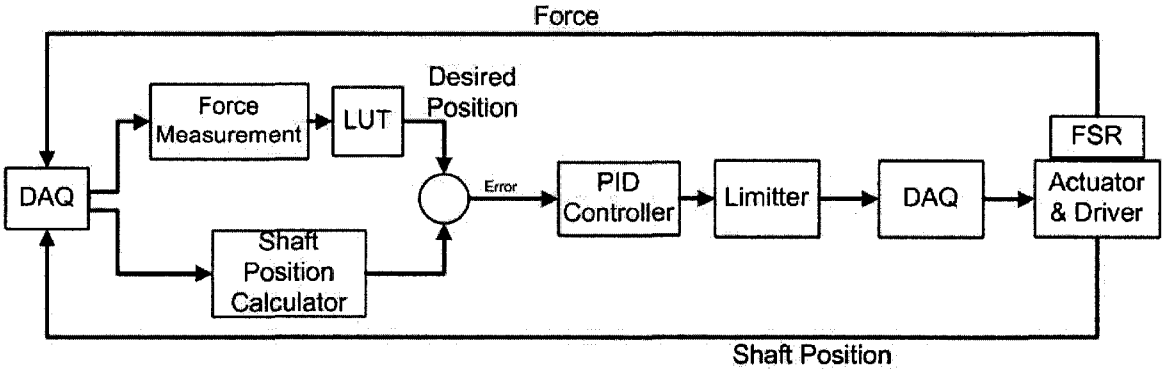

(a)

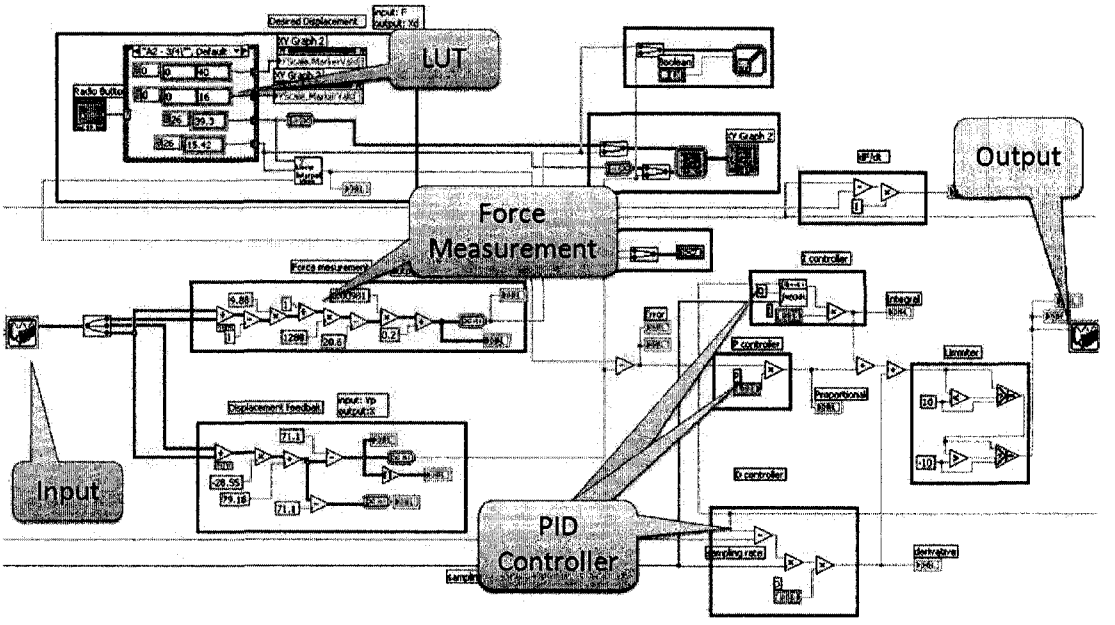

(b)

Figure 4.17. a) The block diagram of the completer system b) The block diagram simulated in the LabView programming environment.

4.9 Experiments

Different materials including elastomers (*A2 (¾inch), EVA(½ inch), ICF400(1inch), A2-FR((¾inch) and B1((¾inch))* and a hard material (Plexiglas) are selected to be simulated by the actuator. The strain-stress relations for these materials are shown in Figure 4.18.

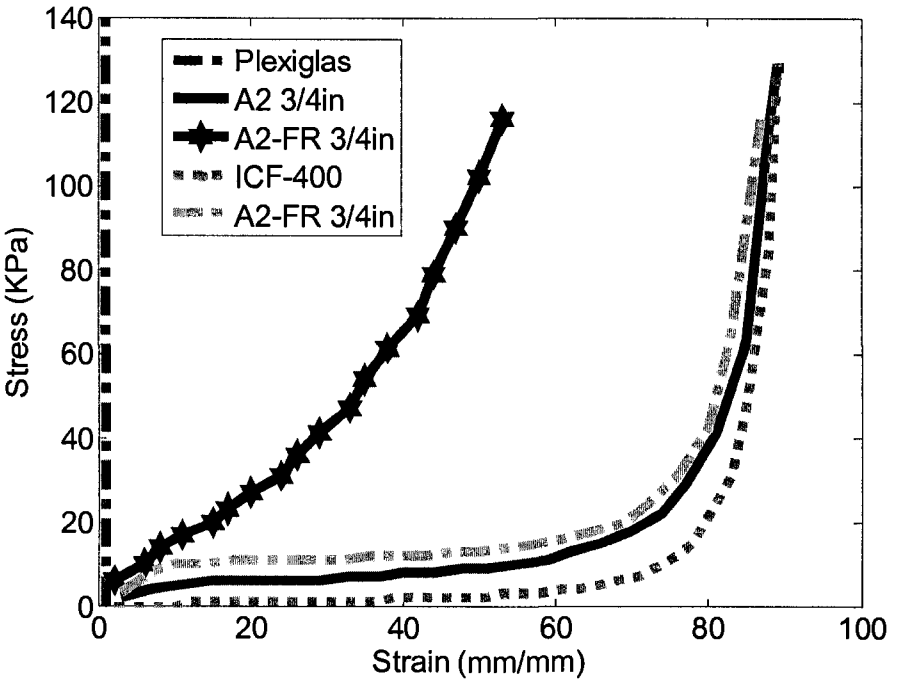

Figure 4.18. The stress-strain curves for different materials

To compare the performance of the proposed tactile display, the force-position relation for each simulated material is saved, plotted and compared to the force-position relation of the material. Each curve can be divided into two separate phases: loading and unloading. The loading phase starts when the finger makes contact to the shaft and applies force. As soon as the force is removed, the unloading phase is started. In this phase, the material with a speed which depends on the structure of the material, it returns

to its initial form. The softer the material, the return speed is slower. Figure 4.19 shows both phases in A2 (*¾ inches*).

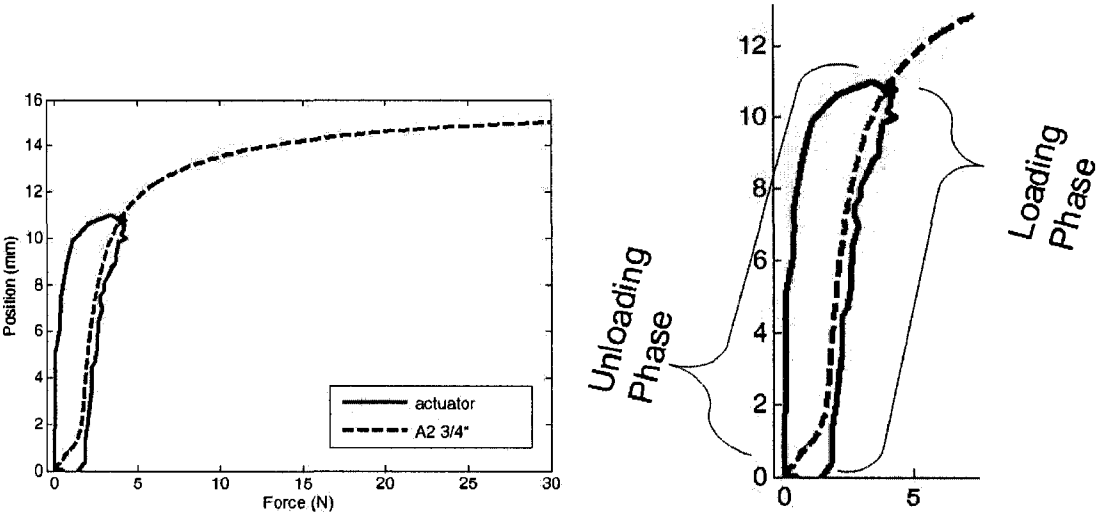

Figure 4.19. The force-position relation for A2 (3/4")

Figure 4.19 shows that during the loading phase, a small error exists between the simulated curve and the real curve. By selecting the optimum controller, the error is tried to be minimized. This error is larger in the unloading phase; however it is not very important. Because the unloading phase, both in elastomer and in linear actuator, starts when the finger separates from the surface of the object and the speed of unloading does not affect the sense of touch.

4.10 Results and Discussion

Figures 4.20, 4.21 and 4.22 show the loading and unloading phases for three other elastomers (EVA ½ inch, ICF400 1inch, and B1 ¾ inch).

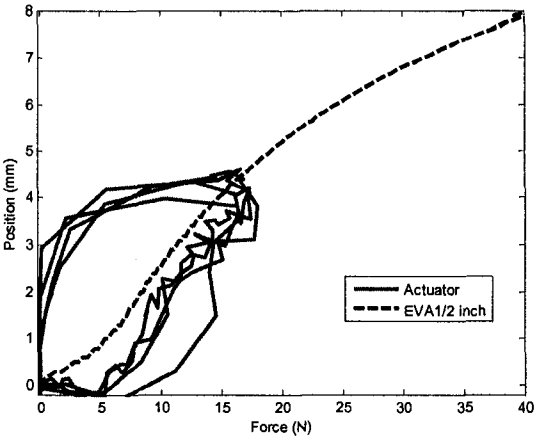

Figure 4.20. The position-force curve of EVA elastomer and its simulated equivalent

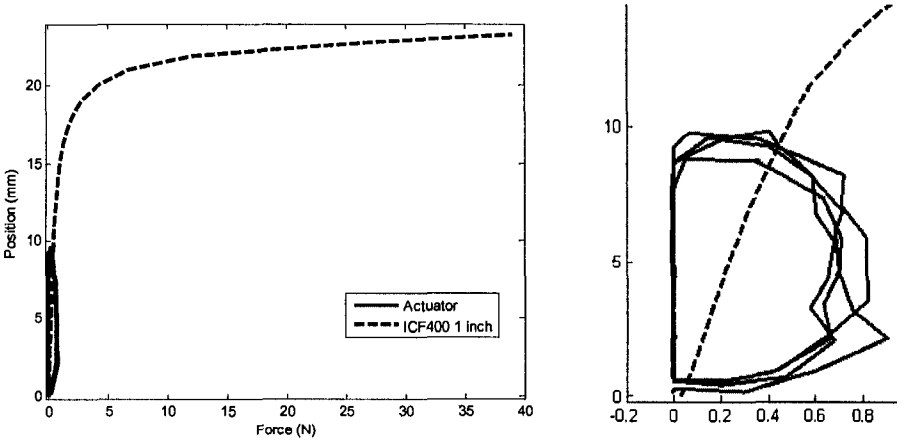

Figure 4.21. The position-force curve of ICF400 elastomer and its simulated equivalent

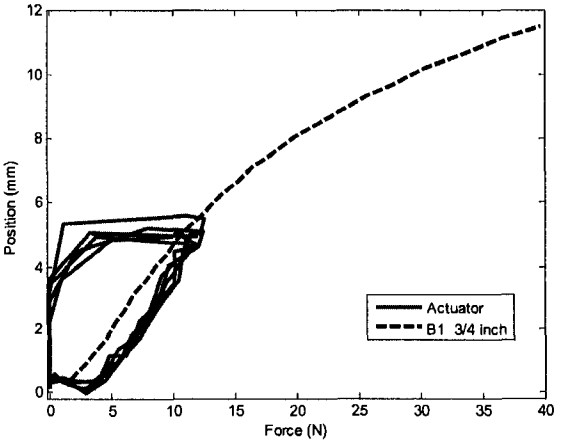

Figure 4.22. The position-force curve of B1 elastomer and its simulated equivalent

The rate of applying force is also important in the feel of softness. As depicted in Figure 4.23 the error is negligible when the force is applied slowly. However, when the force is applied suddenly, the error becomes larger. Figure 4.23 shows the real and desired force-position curves for two different speeds. In the first cases the force is applied slowly and in the second case it is applied abruptly. The error in the first case is much less than the other second case. When the finger touches an object for softness recognition, it usually applies the force slowly. So the error would be negligible.

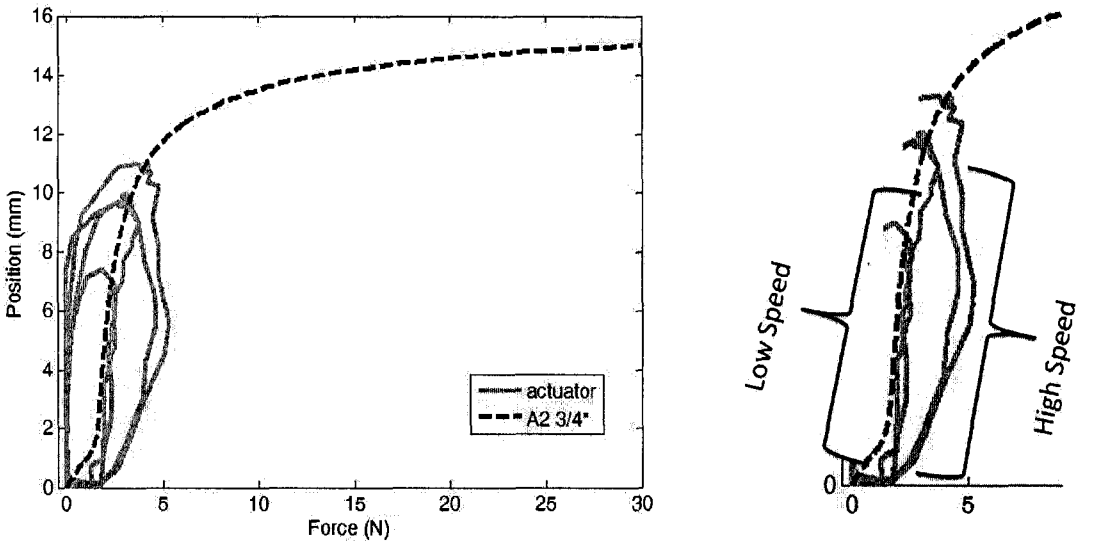

Figure 4.23. The effect of the force rate on the error

To evaluate the efficiency of the tactile display, an experiment is conducted. In the experiment, an observer touches 4 elastomer materials with finger. Then she/he touches the linear actuator and determines which elastomer its softness is similar to. For each person the experiment repeated for all of the four simulated materials. The setup which is used for testing the volunteers is used in Figure 4.24.

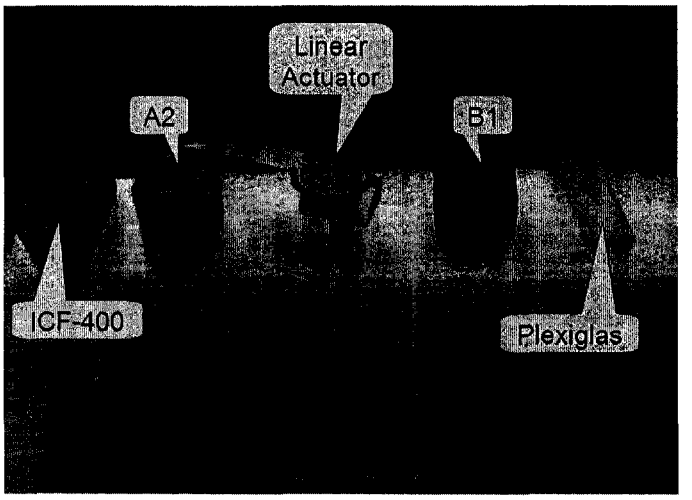

Figure 4.24. The setup of the experiment

To remove the effect of visual feedback, the setup is covered and the volunteer cannot see the materials. In the first experiment four different materials (ICF-400, A2, B1, and Plexiglas (Young modulus =1.2GPa) are simulated by the tactile display. The volunteer touches the materials and finally decides which one of the objects has similar softness with the display. Totally, 25 persons participated in the experiment. All of the participants successfully distinguished the simulated elastomer (Table 4.2).

Table 4.2. Results of the first human subject test

SIMULATED MATERIAL	ICF-400	A2	B1	PLEXIGLAS
recognized	25	25	25	25
error	0	0	0	0

In the second experiment two materials with very similar mechanical properties (H1N and ICF-400) are simulated by the display (Table 4.3). The results of the simulation show some errors in recognition.

Table 4.3. Results of the second human subject test

SIMULATED MATERIAL	A2-FR ¾"	A2 ¾"
recognized	15	12
error	10	13

The reason is that distinguishing these two materials even with finger touch is difficult specially without visual feedback it is very difficult. Figure 4.25 show that the mechanical properties of these two materials are very close.

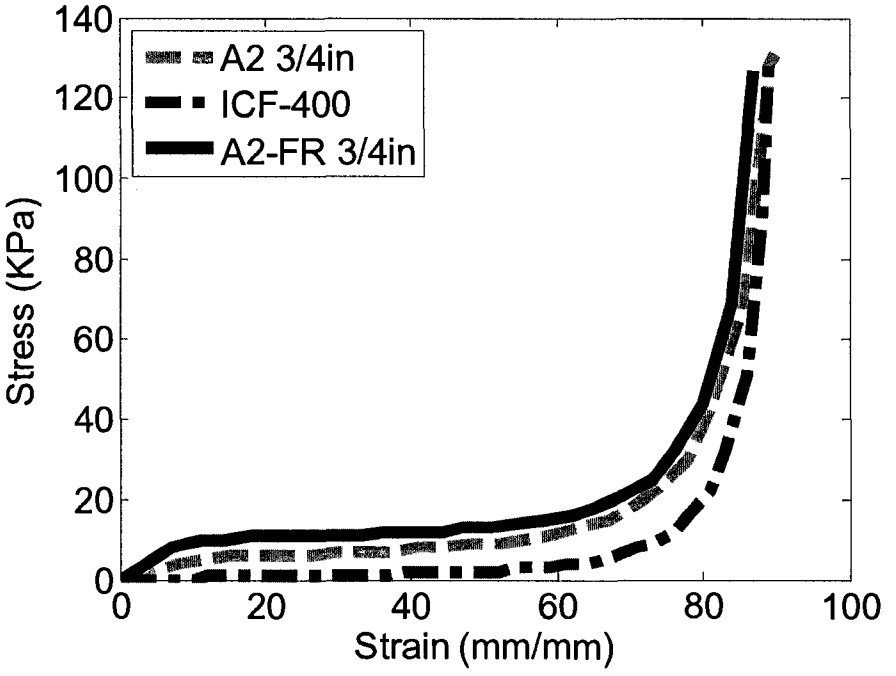

Figure 4.25. The material properties of the elastomers for the second experiment

4.11 Summary and Conclusion

A system for displaying the softness of different materials has been presented. The proposed system is comprised of a linear actuator, a force sensor, data acquisition

card and processing software. The system potentially could be used for telerobotic surgery and virtual reality.

Initially, the mechanical properties of the materials are characterized using mechanical compression tests. These data are saved and used by the processing software for reproducing the same properties by the tactile display. Having the dimension of the area over which the force is applied, these stress-strain data can be transformed to force-compression which is used by the processing software to actuate the display. The data are saved in lookup table in the processing software.

The processing software gathers information from the applied force to the shaft of a linear actuator and the position of the shaft. Having this information and using the lookup table, the response of the material to the applied force is extracted from the table and used as the input to a PID controller which prepares necessary commands to the linear actuator to move the shaft.

Experiments on the tactile display were conducted by human subjects and the results were registered. Different materials were simulated by the tactile display and compared to the real objects. The results showed that the developed tactile display can replicate the softness of materials very closely. It is proved to be a feasible technique with great potential use in robotic surgery and Minimally Invasive Surgery (MIS).

CHAPTER 5

SOFTNESS DETECTION USING SENSORIZED GRASPERS

In the MIS graspers, the information about the amplitude, waveform and frequency content of the load transferred to soft object is important in performing experimental tests. In addition, the response of all smart endoscopic graspers (MIS graspers equipped with tactile sensors) depends on the behavior and softness of the grasped object. To the best of authors' knowledge, no comprehensive work on the interaction between the soft tissue and the grasper is reported. This chapter investigates the characteristics of the dynamic load which is experienced by the soft object in a grasping action. The objective of the research is to obtain the profile of the load versus the time for the use in finite element analysis as well as experiments on the fabricated smart endoscopic graspers. A novel smart laparoscopic grasper is also presented and tested. The proposed smart grasper determines the softness of the grasped objects by measuring the grasper jaws angle and the force applied by the surgeon's hand.

5.1 Problem Definition

After the sensor is manufactured, in experimental testing stage of smart endoscopic graspers and to characterize and calibrate, we require applying dynamic forces to the sensorized graspers. These forces should be similar to the real forces that the grasped soft objects experience. But the question is that what these force profiles look like? Although the amplitude and the profile of the force depend on the geometry of the endoscopic grasper to some extent, we paid more attention to the influence of the soft object on the

grasper-object interaction in a typical MIS grasper. In the absence of the soft tissue, the elastomeric materials, which exhibit many of complexities of soft materials (e.g., material nonlinearity, and viscoelasticity), were tested. Figure 5.1 shows a typical grasper and the grasped soft object (i.e., elastomeric material). As shown in this figure, a force sensor was also used to measure the average force transmitted to the grasped object.

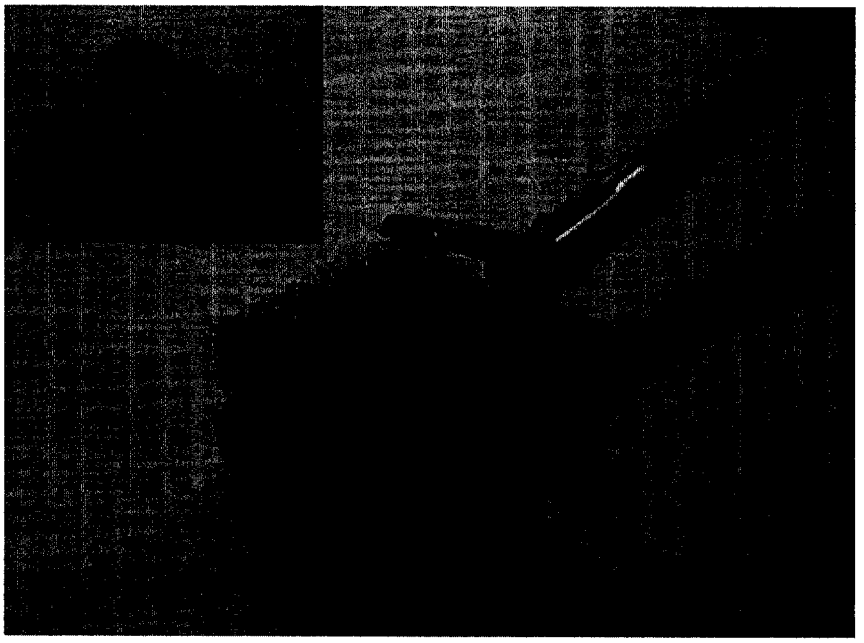

Figure 5.1. A typical grasper, an elastomeric material, and an FSR sensor.

5.2 Method

To measure the force experienced by the grasped object, a suitable force sensor was selected and inserted inside the grasped material. The selected sensor was very small in size, thin and flexible to minimize any unwanted effects caused by the sensor itself. The force sensitive resistor (FSR) sensor from Interlink Electronics is in fact a piezoresistive sensor in which the resistance is inversely proportional to the force applied to its surface.

For the experiments, as shown in Figure 5.2, an endoscopic grasper was equipped with three sensors; a potentiometer to measure the grasper jaws angle, a force sensor to measure the force applied by the hand to the grasper handle, and a force sensor inserted inside the test materials to measure the force applied to the material.

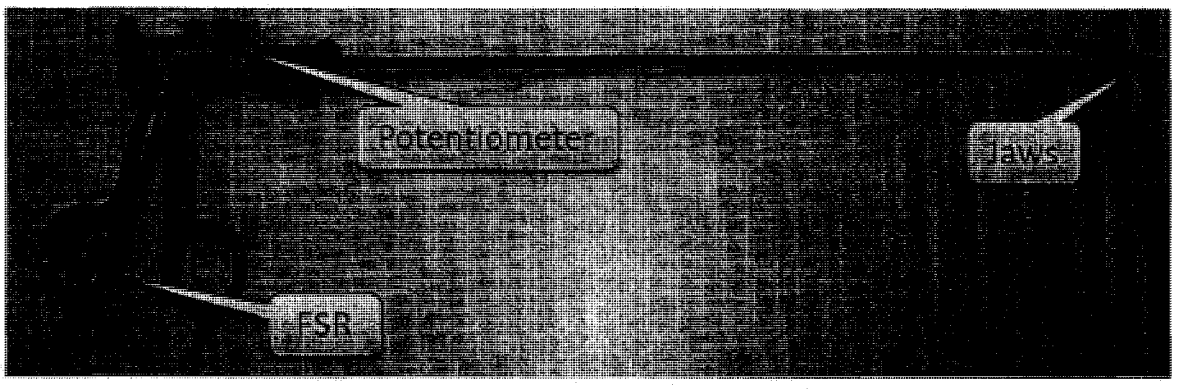

Figure 5.2. A picture taken from endoscopic grasper equipped with two FSR sensors and a linear potentiometer.

Two FSRs are used in the experiments. The first FSR is placed inside the grasped object (Figure 5.1), while the second FSR is placed on the handle of the grasper and measures the force applied by the hand to the grasper (Figure 5.2). The signals from the force sensors (Vo_1 and Vo_2), the signal from the potentiometer (Vp) and the supply voltage (V^+) were fed into the data acquisition card.

To examine the linearity of the FSR sensor and to obtain its calibration curve, an electric circuit as shown in Figure 5.3, was used.

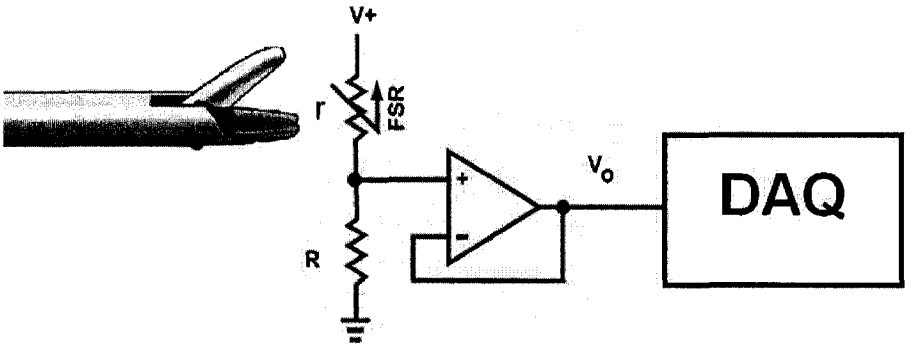

Figure 5.3. The electric circuit used for calibration and subsequent experiments.

The relationship between FSR conductance and the measured voltage, can be found in a similar manner to equation 4.2:

$$C = \frac{1}{r} = \frac{1}{(\frac{V^+}{V_o} - 1)R} \tag{5.1}$$

where, r is the variable resistance of FSR (force-dependent), R is a known biasing resistor (constant); V^+ is the known voltage of an external power supply. The symbol Vo represents the FSR voltage outputs. The signals from the FSR force sensors at the handle and tip of the grasper are denoted by Vo_1 and Vo_2, respectively. At the calibration step, by applying different standard forces ranged from 1 N to 9 N on FSR, nine data points as shown in Figure 5.4 were obtained. It was evident from the measured points that the force-conductance relationship of the FSR can be approximated by a line. The following expression was the result of a least square regression method.

$$C = \frac{1}{r} = a.f + b \tag{5.2}$$

where a=0.079 and b=0.016.

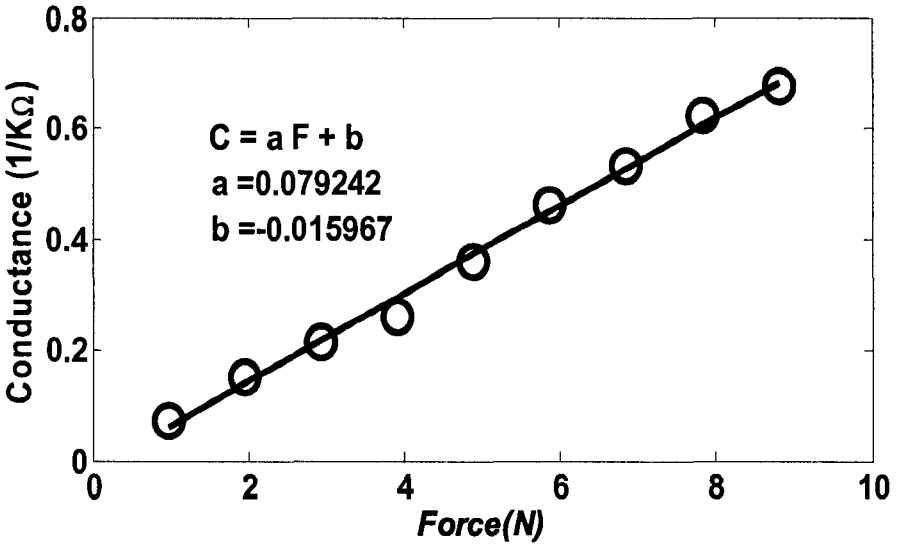

Figure 5.4. The conductance of the FSR versus applied force. A line was fitted to the measured data using least square fitting method.

As explained in section 4.3, the voltage- force relationship can be expressed as:

$$f = \frac{1}{(\frac{V^+}{V_o} - 1)R.a} - \frac{b}{a} \tag{5.3}$$

Using relation (5.3), the real applied force to the grasped objects can be found. As shown in Figure 5.2, a data acquisition system (DAQ) was used to analyze and record the measured data.

Figure 5.5 demonstrates the major blocks developed in LabView. The processing software calculated the applied force to the grasped object (using relationship 3), the handle and the angle of jaws.

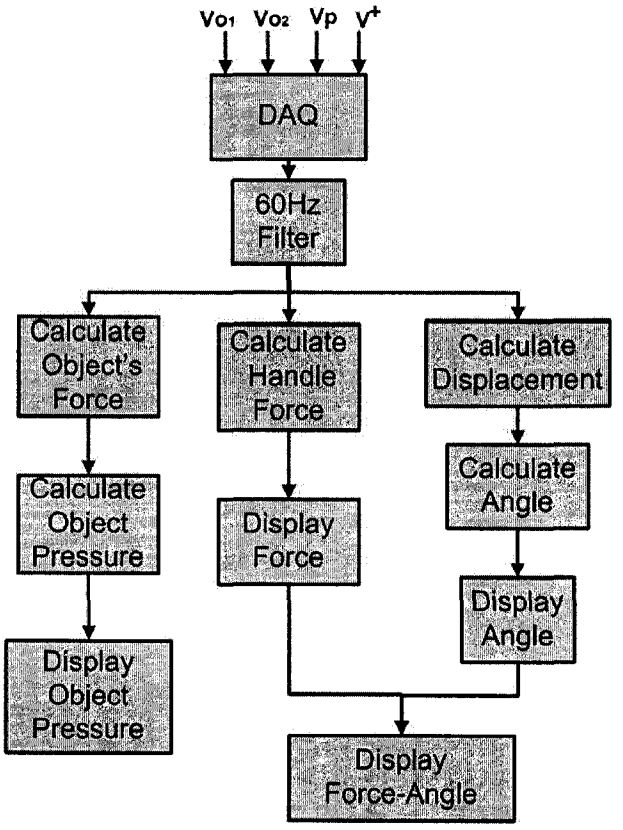

Figure 5.5. The block diagram of the program developed in Labview.

5.3 Experiments

To investigate the profile of the load transferred to different soft materials, initially several soft materials were prepared and their softness were measured using industrial durometers. The materials and their corresponding softness are presented in Table 5.1. The first four materials (supplied by 3M) are considered as very soft to soft materials. These materials were tested using durometer Shore OO which is suitable for very soft materials including soft tissue. The other four materials were different silicone rubbers selected from the standard type A (Shore A) test block kit (ASTM D2240, Instron Co.).

Table 5.1. The measured softness of five different materials used in the experiments

Material	Softness
ICF400	7 (Shore OO)
A2	10 (Shore OO)
EVA	45 (Shore OO)
B3	63 (Shore OO)
Silicone rubber-1(White)	32 (Shore A)
Silicone rubber-2(Blue)	52 (Shore A)
Silicone rubber-3(Red)	71 (Shore A)
Silicone rubber-4(Black)	89 (Shore A)

It should be noted that the materials are sorted from soft to hard (i.e., ICF 400 is the softest material in this group). The materials then were tested using the equipped grasper while an FSR sensor was inserted into the grasped object.

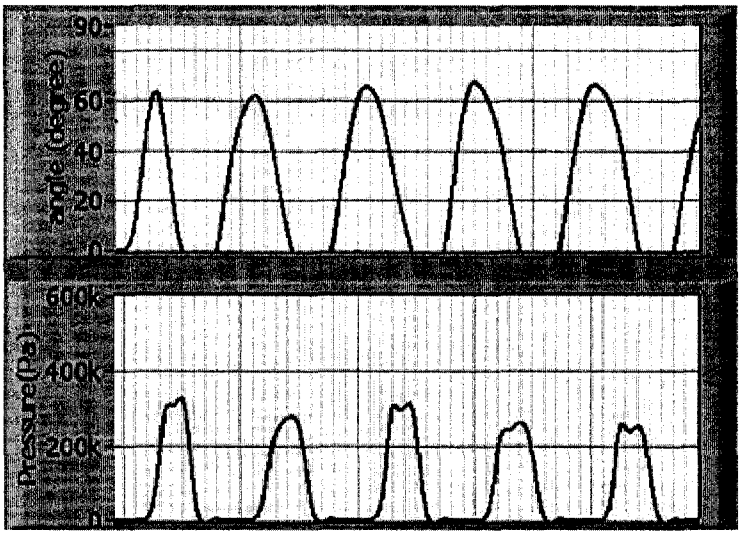

Figure 5.6. Samples of the recorded data. The angle of the grasper and registered pressure applied to the grasped soft object are shown. The pressure is expressed in kPa.

Having the force applied to the object and the dimensions of the force sensor, the average pressure was calculated. These parameters are then plotted in time domain. Figure 5.6 shows a sample of the plotted parameters.

The processing software also calculates and plots the relationship between the applied force and the jaws angle. Figure 5.7 shows the force-angle curve for an elastomer.

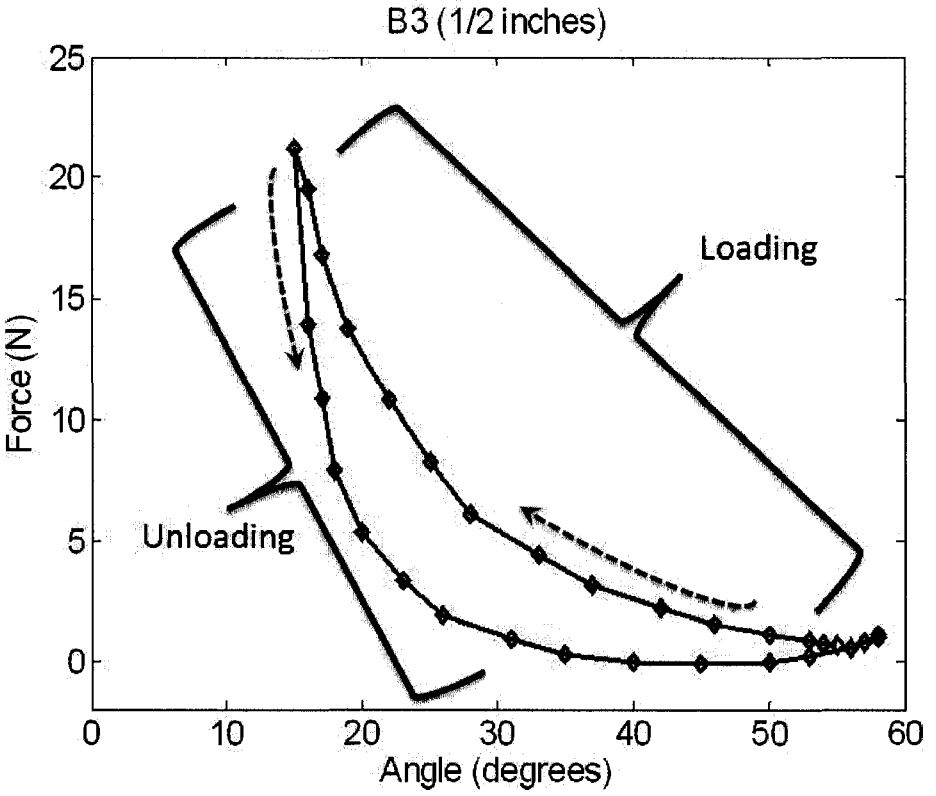

Figure 5.7. Force-angle curve for an elastomer (B3 ½ inches)

5.3.1 Loading vs. Unloading

Two separate phases can be seen in this curve. In the first phase (loading), the open grasper jaws start closing and simultaneously apply pressure on the material. The second phase (unloading) begins when the jaws start opening. In this phase the applied pressure is small. Most of the information of the material properties is in the first phase. The form of this graph depends on the properties of the test material and can give valuable information about these properties. It can be shown that the speed of grasping is

also an important parameter which can change the force-angle curve. However, in this research work we tried to use similar grasping speed for all test materials.

5.3.2 Energy and steepness

To distinguish force-angle curves of different materials, a criterion is required. In this work, average slope and energy are considered as the criteria.

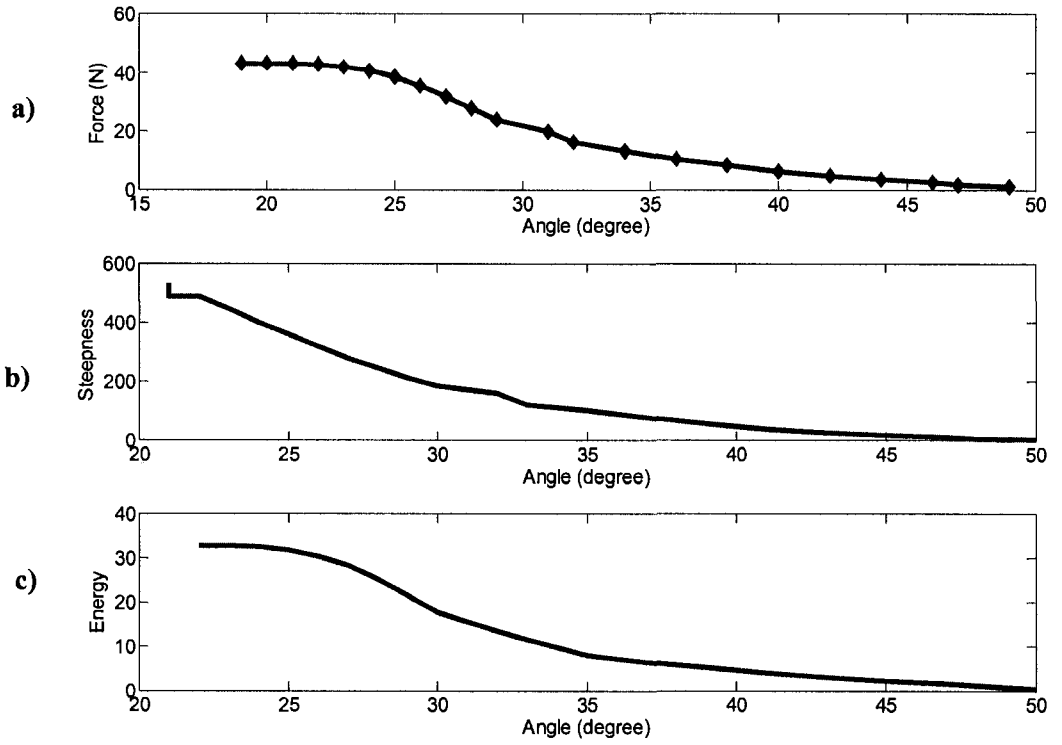

Figure 5.8. a) Force angle curve for a silicone rubber b) average steepness c) energy

The energy of the angle-force curve shown in Figure 5.8-a is defined as the surface surrounded by loading curve and the angle axis from the beginning of the loading phase to angle in which the energy is measured. The steepness is the slope of the angle force curve averaged over the angle axis, again from the beginning of the loading phase to the measuring angle. For example the steepness at 40 degrees is the slope averaged

from 50 degrees (the beginning of the loading phase) to 40 degrees. Figure 5.8 shows the experiment results for a silicone rubber. In Figure 5.8–b the steepness is plotted. Figure 5.8–c shows the energy. To compare the softness of the grasped objects, the engery or steepness of the obejct are compared in an arbitrary angle.

5.3.3 Calibrating the Grasper

The MIS grapser has several mechanical connections. These connections produce friction. The force which is used to overcome the frictions, can cause error in determining the softness of the objects, specially when the objects are soft. Because grabing soft objects need small amount of force which is comparable with the friction force.

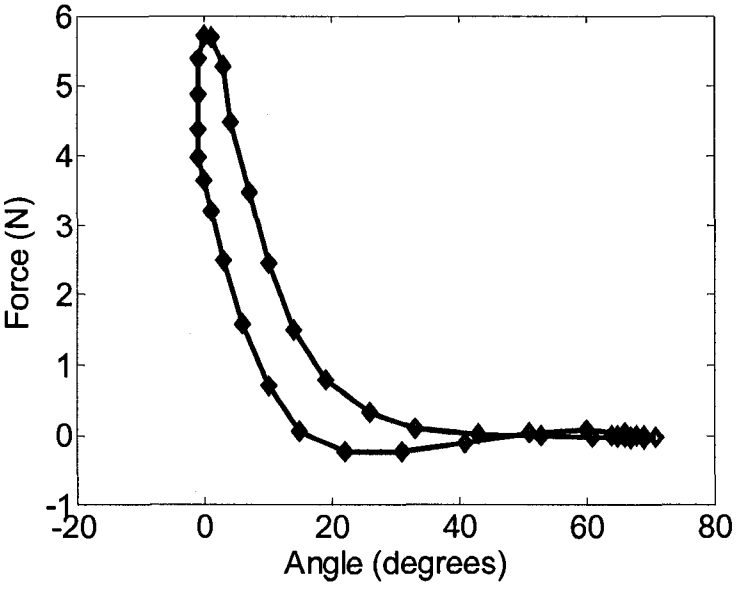

Figure 5.9. Experimental force-angle curve data for an empty grasper

Figure 5.9 shows the experimental force-angle curve data for an empty grapser. Both loading and unloading phase are shown in this figure. When an object is grabed by the grasper, to minimize the effect of the frictions, this extra force must be subtracted from

the real force applying to an object. To do so, a fomula is required to calculate the friction force in each angle. To find the formula, using least square error method, a curve is fitted on the experimental data.

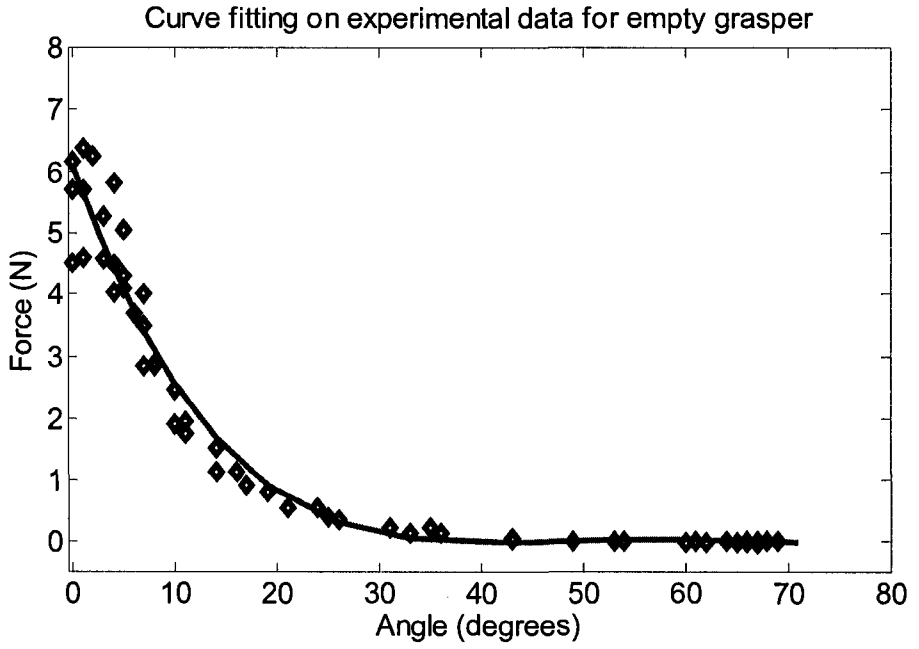

Figure 5.10 . Experimental data of several consecutive loading curves and the fitted curve

Figure 5.10 shows the experimetal data of several consequtive loading curve. The following forth order curve is fitted to the experimental data:

$$f = 6.9x10^{-7}\theta^4 - 1.5810^{-4}\theta^3 + 1.3110^{-2}\theta^2 - 0.47\theta + 6.11 \qquad (5.4)$$

The result of subtracting the friction force is shown in Figure 5.11. Figure 5.11-a shown a grasping action for the empty grasper. Figure 5.11-b shows the calculated force using relationship 5.4. Figure 5.11-c shows the compensated curve. In this figure it is shown that the effect of friction force is completely removed.

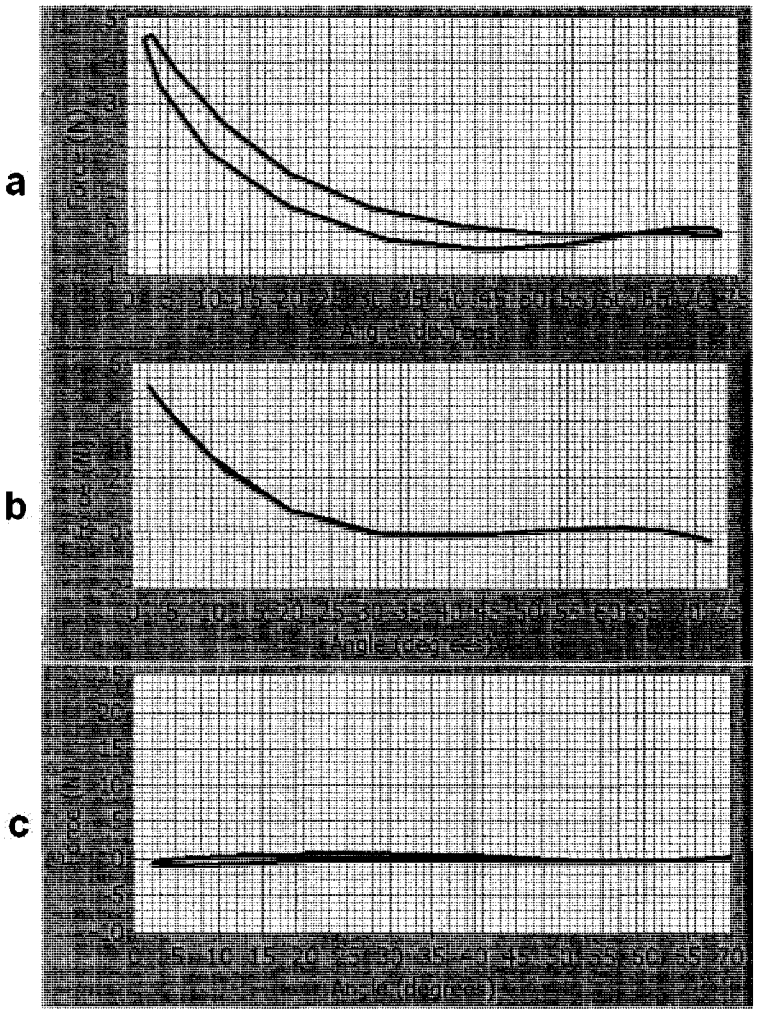

Figure 5.11. Subtracting the friction: a) grasping action for an empty grasper. b) calculated force using curve fitting formula. c) the compensated curve

5.4 Results and Discussion

The registered pressures which are transmitted to different soft materials are shown in Figure 5.12. As mentioned before, ICF400 (Figure 5.12-a) is very soft and silicone rubber-2 (blue) (Figure 5.12-e) is the hardest in this group. It can be concluded from

Figure 5.12 that as the material becomes harder, the transferred pressure to the material becomes larger.

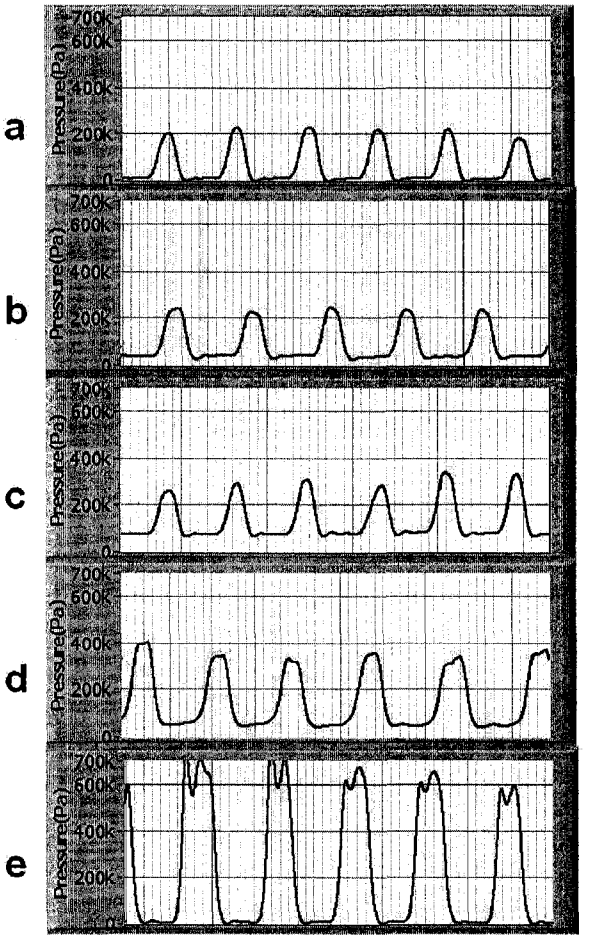

Figure 5.12. The force profile for five different soft materials: a) ICF400, b)A2FR, c)H1N, d) Silicone rubber-1, and e) Silicone rubber -2

For example, in ICF400 (with a softness of 7 in Shore OO) the maximum transferred pressure is 200kPa, and for silicone rubber-2 (with a softness of 60 in Shore A) the maximum pressure is more than 600kPa.

Another important conclusion drawn from Figure 5.12 is that the waveform of the transferred pressure also depends on the softness of the grasped material. For the soft

materials, the pressure has a half sinusoidal form. For the harder materials the pressure appears more like a pulse wave.

These force profiles can be associated with the response of soft materials in grasping in low frequencies. When a soft material is grasped, it is gradually compressed and the resistance against compression is increasing correspondingly. When the grasper starts to open, due to the same spring action, the soft material starts to expand so that it maintains its contact with the grasper jaws. This causes a smooth rise and fall in the force profile which is similar to a sinusoidal wave. In fact the frequency content of the force profile also shows that this force profile can be approximated with a sinusoidal wave. On the other hand, in the hard material grasping, once the grasper touches the object, the force soars rapidly without significantly changing the grasper angle. In the opening stage, due to the rigidity of the grasped object, the grasper is detached from the object quickly. This behavior causes a force profile which can be approximated by a pulse wave. This conclusion is particularly important for the experimental tests on smart graspers. This result confirms that the selection of sinusoidal waveform to test the fabricated MIS tactile sensor is the best alternative in a laboratory test setup. It is always argued that the surgeon does not apply the force to the grasper in a sinusoidal wave and the experiments using this waveform are questionable. But the latter conclusion shows that even if the surgeon does not apply the force in a sinusoidal wave, for the soft materials, the transferred load to the grasped object is almost sinusoidal.

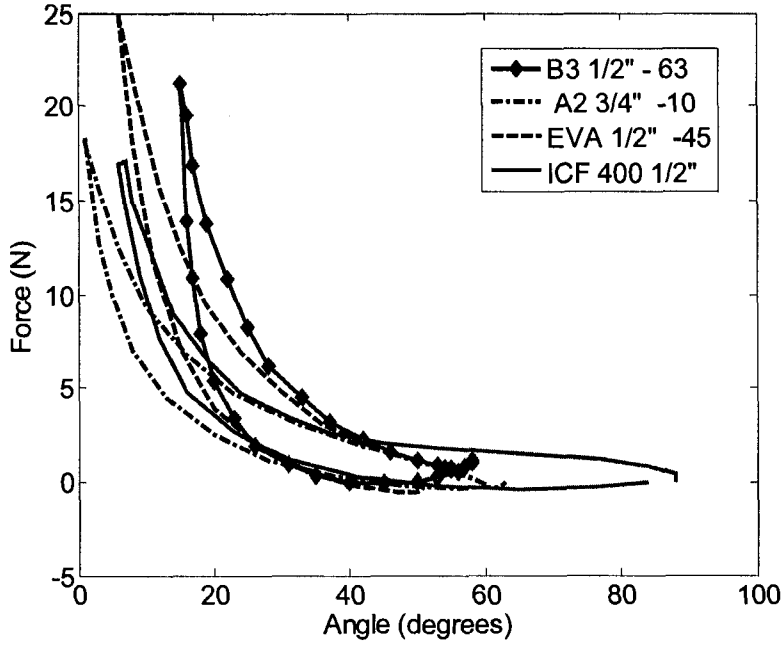

(a)

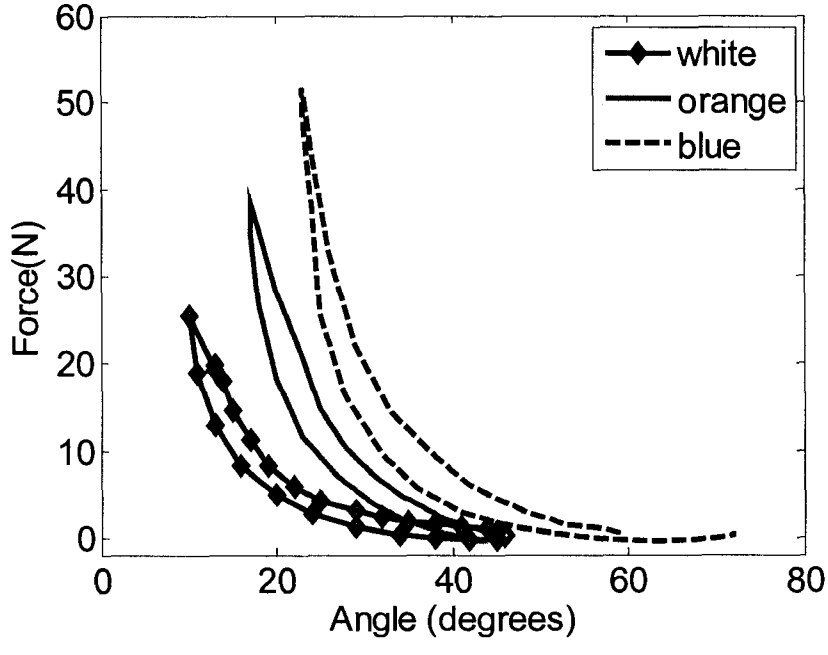

(b)

Figure 5.13. The force-angle curve for a) ICF400, EVA, B3, A2

b)silicone rubbers (white, orange, blue)

The force-angle curves, Figure 5.13-a and 5.13-b, demonstrate the force-angle relationship for different materials. In these graphs, the force represents the load that is applied to the handle of the grasper and angle is the angle between the grasper jaws. From Figure 5.13 it is found that in the loading phase of the curves, the average slope of the curve is proportional to the softness of the grasped material.

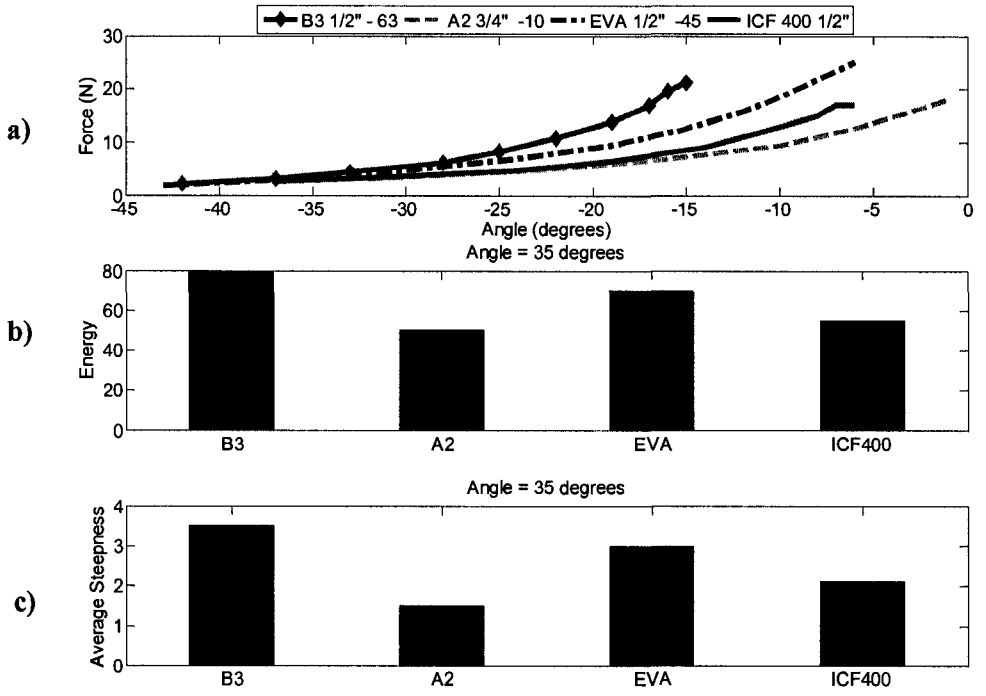

Figure 5.14. The force-angle curve. Energy and steepness measured at 45 degrees. b) energy c) steepness

For softer materials the average slope is smaller than that of the harder materials. Figure 5.14 shows the energy and steepness for four elastomers. Both energy ($E = \sum_{\theta_1}^{\theta_2} F(\theta).\Delta\theta$) and steepness ($S = \frac{1}{N}\sum_{\theta_1}^{\theta_2} \frac{F(\theta+\Delta\theta)-F(\theta)}{\Delta\theta}$) criteria plotted in Figures 5.14-b and 5.14-c

can easily be used to arrange the softness of these materials. It is evident that EVA, H1N, A2FR and ICF400 are arranged from hard to soft. Figure 5.15 shows the force-angle curves for the same materials, but the angle on which the energy and steepness are calculated based is 25 degrees. It shows that the result of applying the criteria is independent of the angle to which the criteria are applied.

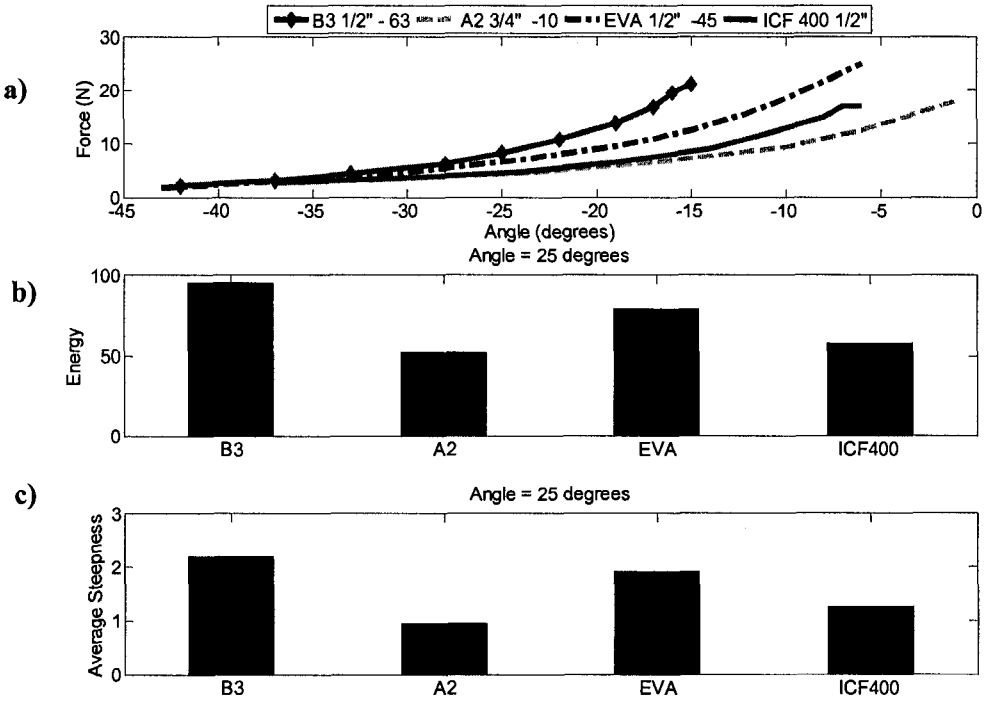

Figure 5.15. a) The force-angle curve. Energy and steepness measured at 45 degrees. b) energy c) steepness

Finally Figure 5.16 shows the force-angle curve of four silicone rubber samples. Figure 5.16-b and 5.16-c shows the energy and steepness of the curves and still it is possible to use them to arrange the softness of the silicones.

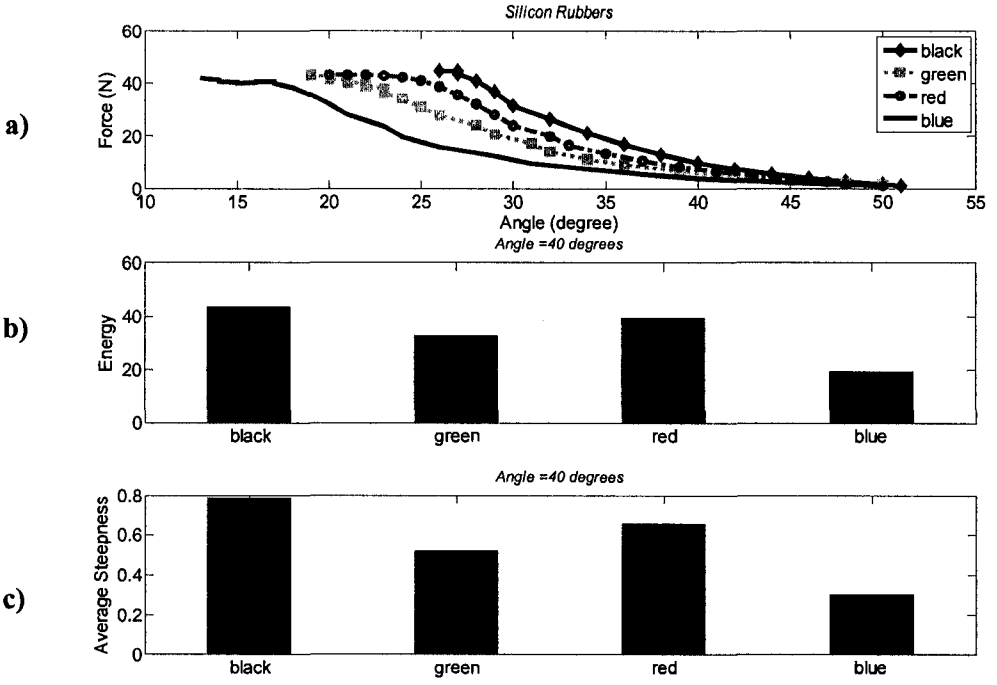

Figure 5.16 . a) Force angle curve for silicone rubbers b) energy) c) steepness

5.5 Summary and Conclusions

A system for characterization of force applied from the grasper jaws to the grasped objects is presented and corresponding experiments are performed. The proposed system is comprised of an endoscopic grasper equipped with force sensors, a potentiometer for measuring the jaws angle, and a signal processing unit. It is shown that this system potentially can be used for softness characterization of the grasped tissue in a laparoscopic surgery.

The test materials include three elastomers and two silicone rubbers. The experiment results show that for the soft materials the transferred force from the grasper to the material is sinusoidal. As the material becomes harder, the pressure waveform changes from sinus to pulse. Another conclusion is drawn that for harder materials the applied

load to the object becomes larger. Finally using the force-angle graphs plotted for the test materials, it is shown that the grasped materials can be differentiated from each other based on their softness.

CHAPTER 6

SUMMARY, CONCLUSIONS AND FURTHER WORKS

This Chapter concludes the thesis by providing a summary of results obtained in the preceding chapters, a description of the major contributions and conclusions drawn from those results, and suggestions of areas for future work.

6.1 Summary of Contributions

Research work is summarized as follows:

1. The fabricated array of sensors is integrated into the jaws of a laparoscopic grasper.
2. The feedback system and electric circuitry are designed and fabricated to transmit the signals from the sensor array to the DAQ.
3. The design and development of algorithms and software, which processes the sensor signals, is converted into color coded visual softness data that the surgeon views on a monitor. The visual display transfers the softness information to the surgeon in real time and is easily interpreted.
4. The developed visual softness representation system is calibrated and tested with different materials and elastomers.
5. The visual softness information is accompanied with a color-scale which can give the softness value in the scale of Shore to the surgeon
6. The sensor array for detecting embedded lumps within the soft tissue has been designed and fabricated.

7. Software has been designed and developed which processes signals from any lump detection array and produces a singular and two-dimensional image from within that tissue.
8. A physical softness tactile display, using linear actuator capable of reproducing the material characteristics of different materials, has been produced and a working sample fabricated.
9. The physical tactile display can successfully simulate the nonlinear characteristic curve of different material and simulate the same softness.
10. The force profile within the grasped objects in a laparoscopic grasper has been measured and characterized. This force profile is then related to the softness of the grasped object.
11. The laparoscopic grasper for soft objects has a very similar profile to a half sinusoidal signal and, for hard materials, is similar to a pulse.
12. A new tactile sensing system has been designed and developed integrated on the laparoscopic grasper that is capable of dynamically measuring the softness of grasped objects and applied force by the surgeon.

6.2 Conclusion

This thesis has described new methods of tactile display and sensing for MIS operation, teleoperation and robotic surgery. A visual tactile display shows the softness of the objects, the presence of the embedded lumps within the soft tissue, and its location and approximate size. A physical softness display capable of reproducing the characteristics of different materials was also presented. Finally, a tactile sensor was

developed specifically to measure local softness of the grasped tissue. Concepts for both display and sensor devices have been validated, in conjunction with initial experiments, that clearly show their potential and has shed new light on the softness transmission in teleoperation and robotic surgery.

6.3 Improvements and Extensions

As with most designs, one learns a great deal from each generation of prototypes. The devices presented in this thesis have evolved considerably since their conception. However, it is clear that many improvements can still be made and the following subsections outline suggested improvements and possible future work in these areas.

6.3.1 Visual Tactile Display

Increasing the number of sensors in an array improves the resolution of the display. When adding a PVDF layer underneath the sensor arrays, the force applied by the grasper under each sensor can be measured and the pressure distribution on both sides of the grasper jaws will be displayed in the visual display. It helps in measuring the force that is being applied to the tissue which is an important parameter for the surgeon.

6.3.2 Lumps Detection and Display

As the resolution of the lump display increases, estimating the size and exact location of the lump becomes more exacting. Therefore, to further enhance the resolution, it is necessary to add to the number of elements in the sensor array which is possible only by reducing the size of each sensor element. Microfabricating the sensor can be a solution to the problem.

Software can be developed to measure and automatically identify the size of embedded lumps in order to make it easier for the surgeon to recognize its existence. Estimating the softness of an embedded lump is also proposed which can give important information about the lump to the surgeon.

6.3.3 Physical Tactile Display

In order to feel the softness of a surface, the physical tactile display should be expanded to an array of at least 5x5. The errors can be significantly reduced by replacing the linear actuator with one of higher speed in order to increase the similarity in simulating softness.

6.3.4 Sensorized Endoscopic Grasper

A force sensor can be incorporated in the central bar of the laparoscopic grasper to measure the total force applied by the surgeon to the tissue. A higher quality force sensor can be replaced the FSR to increase the accuracy of the force measurement.

BIBLIOGRAPHY

1. Sheridan T. B., "Telerobotic, Automation, and Human Supervisory Control", Cambridge, MA: The MIT Press, 1992.
2. Dennerlein J. T., Millman P. A., Howe R. D., "Vibrotactile Feedback for Industrial Telemanipulators.", Proc. ASME Dynamic Systems and Control Division, Dallas, TX, USA, 1997.
3. Burdea G. C., "Force and Touch Feedback for Virtual Reality", New York, NY: John Wiley & Sons, Inc., 1996.
4. Hayashi K., Takahata M., " Objective Evaluation of Tactile Sensation for Tactile Communication" NTT DoCoMo Technical Journal, Vol. 7 No.3, pp.39-43, 2005.
5. Johansson R.S., "Tactile sensibility in man. A quantitative study of the population of mechanoreceptive units in the glabrous skin area of the hand", University Medical Dissertations, Umeå University, Umeå, Sweden, 1978.
6. Johansson R.S., Vallbo A.B., "Skin mechanoreceptors in the human hand: An inference of some population properties'', Sensory Functions of the Skin in Primates. Zotterman, Y. Ed., Pergamon Press., pp.185–99, 1976.
7. Johansson R.S., Vallbo A.B. "Tactile sensitivity in the human hand: relative and absolute densities of four types of mechanoreceptive units in glabrous skin", J. Physiology. Vol. 286, pp. 283–300, 1979.
8. Lindenblatt G., Silny J., "Evaluation and comparison of 50 Hz current threshold of electrocutaneous sensations using different methods", Journal of Zhejiang Univ SCIENCE B, Vol.7, No.12, pp.933-946, 2006.

9. Johansson R. S., Lundström R., " Lokala vibrationer och handens taktila känsel", Arbetarskyddsfondens sammafattningar, ASF rapport, proj. 79/104, Edited by 1983 Nr. 571, Liber, Stockholm.
10. Johansson R.S., Vallbo A.B.. "Tactile sensory coding in the glabrous skin of the human hand", Trends Neurosci, Vol. 6, pp. 27-31, 1983.
11. Vallbo A.B., Johansson R.S. ,"Tactile sensory innervation of the glabrous skin of the human hand", Active Touch, the Mechanism of Recognition of Objects by Manipulation, Edited by GORDON G, pp 29-54. Pergamon Press Ltd., Oxford, 1978.
12. Johansson R.S., Vallbo A.B.,"Tactile sensory cording in the glabrous skin of the human hand", Trends in Neurosciences, Vol. 6, pp. 27-32, 1983.
13. Kajimoto H., Kawakami N., Maeda T., Tachi S., "Electrocutaneous Display as an Interface to a Virtual TactileWorld", Proc. Virtual Reality Conference (VR.01), pp.289-290, 2001.
14. Edin B., Vallbo A. B. ,"Stretch sensitization of human muscle spindles", J. Physiology, Vol. 400, pp.101-111, 1988.
15. Edin B., Vallbo A. B., "Twitch contraction for identification of human muscle afferents". Acta Physiol Scand, Vol. 131, pp.:129-138, 1987.
16. Edin B., "Classification of muscle stretch receptor afferents in humans", Umeå University Medical Dissertations, New Series 209, UMEÅ, 1988
17. Edin B., Abbs J.H., "Finger movement responses of cutaneous mechanoreceptors in the dorsal skin of the human hand", J. Neurophysiol, Vol. 65, pp.657-670, 1991.

18. Jungmann M., Schlaak H. F., "Miniaturised Electrostatic Tactile Display with High Structural Compliance", Proc. Eurohaptics Conference, Edinburgh, U.K., 2002.

19. Schmidt R. F., Tews G., "Physiologie des Menschen", 23rd edition, Springer Verlag, Berlin, 1987.

20. Moy G., Singh U., Tan E., Fearing R. S., "Human psychophysics for teletaction system design", The Electronic Journal of Haptics Research, Vol. 1, No. 3, 2000.

21. Kurt A. Kaczmarek, "Electrotactile and vibrotactile displays for sensory substitution systems", IEEE Trans. on Biomed. Eng., Vol. 38, No. 1, pp. 1-16, 1991.

22. Hong Z. Tan, M. A. Srinivasan, B. Ebermann, B. Cheng, "Human factors for the design of force-reflecting haptic interfaces", ASME Dynamic Systems and Control, Vol. 55, No. 1, pp. 353-359, 1994.

23. Caldwell Darwin G., Tsagarakis N., Giesler C., "An integrated tactile/shear feedback array for stimulation of finger mechanoreceptor", Proc. 1999 IEEE Inter. Conf. on Robotics & Automation, Detroit, Michigan, pp. 187-192, 1999.

24. Tendick F., Sastry S.S., Fearing R.S. and Cohn M., "Applications of micromechatronics in minimal invasive surgery", IEEE Trans. Mechatron., Vol. 3, pp. 34-42, 1998.

25. Venkata Raghavaiah Chowdhary Kode , Master's thesis, Case Western Reserve University, January 2006.

26. Saleh J. W., "Laparoscopy", Saunders, Philadelphia, 1988.

27. NIH "NIH consensus conference – gallstones and laparascopic cholecystectomy". J. American Medical Association, Vol. 269, No. 8, pp. 1018-1024 , 1993.

28. Way L. W., Bhoyrul S., and Mori T., Eds., "Fundamentals of Laparoscopic Surgery," London, U.K.: Churchill Livingstone, 1995.

29. Graber J. N., Schultz L. S., Pietra_tta J. J., and Hickok D. F., "Laparoscopic Abdominal Surgery", McGraw-Hill, San Francisco, 1993.

30. Fred E. Silverstein and Guido N.J. Tytgat. Atlas of Gastrointestinal Endoscopy. Gower Medical, New York, 1991.

31. Semm K., "Operative Manual for Endoscopic Abdominal Surgery: Operative Pelviscopy", Operative Laparoscopy. Year Book Medical, Chicago, 1987.

32. Voges U, "Technology in laparoscopy- what to expect in the future", Urologe Ausgabe, Vol. 35, pp.205-214, 1996.

33. Tendick F., Jennings R., Tharp G., and Stark L., "Sensing and manipulation problems in endoscopic surgery: Experiment, analysis, and observation", Presence, Vol. 2, No. 1, pp.66-81, 1993.

34. Cohn M., Deno C., and Fuji J., "Hydraulic actuator, robot containing same, and method of producing same", U.S. Patent Application, 1993.

35. Wendlandt J. M., "Milli robotics for endoscopy", ERL technical report UCB/ERL M94/7, University of California at Berkeley, Department of EECS , 1994.

36. Wendlandt J. M. and Sastry S. S., "Design and control of a simpli_ed stewart platform for endoscopy", Proc. IEEE 33rd Conference on Decision and Control, Lake Buena Vista, FL, December 1994.

37. Suzumori K., Iikura S., and Tanaka H., "Development of exible microactuator and its application to robotic mechanisms", Proc. IEEE International Conference on Robotics and Automation, pp. 1622-1627, Sacramento, CA, April 1991.

38. Deno C., Murray R., Pister K., and Sastry S., "Finger-like biomechanical robots", ERL Technical Report, University of California at Berkeley, Department of EECS, 1992.

39. Cohn M., Lam M., and Fearing R. S., "Tactile feedback for teleoperation", In Telemanipulator Technology, SPIE Proc. 1833, pp. 240-254, Boston, November 1992.

40. Fearing R. S., "Tactile sensing mechanisms", International Journal of Robotics Research, Vol. 9, No. 3, pp.3-23, June 1990.

41. Pasquero J., "Survey on Communication through Touch" Technical Report: TR-CIM 06.04, Version 1: July 2006.

42. Pelrine R., Kornbluh R., Joseph J., Heydt R., Pei Q., Chiba S., "High-field deformation of elastomeric dielectrics for actuators", Materials Science and Engineering C, Vol. 11, pp.89–100, 2000.

43. Yamamoto A., Ishii T., and Higuchi T., "Electrostatic Tactile Display for Presenting Surface Roughness Sensation", Proc. ICIT-IEEE , Maribor, Slovenia pp.680-684, 2003.

44. Yamamoto A., Nagasawa S., Yamamoto H., Higuchi T., "Electrostatic Tactile Display with Thin Film Slider and Its Application to Tactile Tele-Presentation Systems", IEEE Trans. on Visualization & Computer Graphics, Vol. 12, No. 2, pp. 168-177, 2006.

45. Yamamoto A., Ishii T., Takasaki M., Yasui H., and Higuchi T., "Tactile Interface using Ultra-Thin Electrostatic Actuator", Proc. 32nd ISR(International Symposium on Robotics), 19-21 April 2001.

46. Winslow W.M., "Induced fibrillation of suspensions", J. Appl. Phys. Vol. 20 , pp. 1137–1140, 1949.

47. Weinberg B., Nikitczuk J., Fisch A. and Mavroidis C., "Development of electro-rheological fluidic resistive actuators for haptic vehicular instrument controls", Smart Mater. Struct., Vol. 14, pp.1107–1119, 2005.

48. Block H., Kelly J.P., " Electro-rheology ", J. Phys. D: Appl. Phys., Vol. 21, pp.1661, 1988.

49. Conrad H., " Properties and design of electrorheological suspensions", MRS Bull. Vol. 23, pp. 35–42, 1998.

50. Gast A.P., Zukoski C.F., "Electrorheological suspensions as colloidal suspensions", Adv. Colloid Interface Sci., Vol. 30, pp. 153, 1989.

51. Weiss K.D., Carlson D.J., Coulter J.P.," Material aspects of electrorheological systems", J. Intell. Mater. Syst. Struct., Vol. 5, pp. 13–34, 1993.

52. Wagner C. R., Lederman S. J., Howe R. D., "A Tactile Shape Display Using RC Servomotors", Proce. 10th Symposium On Haptic Interfaces For Virtual Environment And Teleoperator Systems, March 2002.

53. Ottermo M.V., Stavdahl O., Johansen T.A., "Palpation Instrument for Augmented Minimally Invasive Surgery ", Proc. 2004 IEEE/RSJ International Conference on Intelligent Robots and Systems, September 28.- October 2, Sendal, Japan, 2004.

54. Ottermo M.V., Stavdahl O., Johansen T.A., "Electromechanical Design of a Miniature Tactile Shape Display for Minimally Invasive Surgery", First Joint Eurohaptics Conference and Symposium on Haptic Interfaces for Virtual Environment and Teleoperator Systems (WHC'05) , pp 561-562, Pisa, Italy, 2005.

55. Ikuta K., "Micro/miniature shape memory alloy actuator", Procee. IEEE International Conference on Robotics and Automation. Cincinnati, pp. 2156-2161, 1990.

56. Ikuta K., Takamoto M., Hirose H.," Mathematical Model and Experimental Verification of Shape Memory alloy for Designing Micro Actuator", Proce. IEEE Micro Electro Mechanical Systems, pp.103- 108,1990.

57. D. Grant,V. Hayward, "Controller for a High Strain Shape Memory Alloy Actuator: Quenching of Limit Cycles", Proc. 1997 IEEE International Conference on Robotics and Automation. Albuquerque, New Mexico. 254 – 259, 1997.

58. Wellman P.S., Peine W.J., Favalora G. E., Howe R.D., "Mechanical Design and Control of a High-Bandwidth Shape Memory Alloy Tactile Display", International Symposium on Experimental Robotics, Barcelona, Spain. June 1997.

59. Nakatani M., Kajimoto H., Sekiguchi D., Kawakami N., Tachi S., "3D Form Display with Shape Memory Alloy", ICAT 2003, December 3-5, Tokyo, JAPAN.

60. Velázquez1 R., Pissaloux1 E., Hafez M., Szewczyk J., "A Low-Cost Highly-Portable Tactile Display Based on Shape Memory Alloy Micro-Actuators", Proceedins of the IEEE International Conference on Virtual Environments, Human-Computer Interfaces, and Measurement Systems Giardini Naxos, Italy, 18-20 July, 2005.

61. Kontarinis D.A., Son J.S., Peine W., Howe R. D., "A Tactile Shape Sensing and Display System for Teleoperated Manipulation", Proc. IEEE international Conference on Robotics and Automation, pp. 641-646, 1995.

62. Pasquero J., Hayward V., "STReSS: A Practical Tactile Display System with One Millimeter Spatial Resolution and 700 Hz Refresh Rate", Eurohaptics Proc., Dublin, pp. 94-110, July 2003.

63. Levesque J., Hayward V., "Experimental evidence of lateral skin strain during tactile exploration", Proc. Eurohaptics , pp. 261-275, Dublin, July 2003.

64. Hayward V., Cruz-Hernandez J. M., "Tactile Display Device using distributed lateral skin stretch", Proceedings of Haptic Interfaces for Virtual Environment and Teleoperator Systems Symposium, ASME/ IMECE 2000, Orlando, Florida, USA. Proc. ASME, Vol. DSC-69-2, pp.1309-1314, 2000.

65. Yun S.k., Kang S., Kwon D., Choi H., "Tactile Sensing to Display for Tangible Interface", Proce. 2006 IEEE/RSJ International Conference on Intelligent Robots and Systems, Beijing, China, October 9 - 15, 2006.

66. Kyung K. , Ahn M., Kwon D., Srinivasan M.A., "A compact planar distributed tactile display and effects of frequency on texture judgment" , Advanced Robotics, Vol. 20, No. 5, pp. 563–580, 2006.

67. Makino Y., Shinoda H., "Suction Pressure Tactile Display Using Dual Temporal Stimulation Modes" SICE Annual Conference 2005, in Okayama, Okayama University, Japan, August 8-10, 2005.

68. Makino Y., Asamura N., Shinoda H., "Multi Primitive Tactile Display Based on Suction Pressure Control", Proce. IEEE 12th International Symposium on Haptic

Interfaces for Virtual Environment and Teleoperator Systems (HAPTICS'04) pp. 90-97, 2004.

69. Makino Y., Asamura N., Shinoda H., "A Whole Palm Tactile Display Using Suction Pressure", Proc. IEEE International Conference on Robotics and Automation, New Orleans, LS, pp.1524-1529, April 2004.
70. Rai-Choudhury P. (Editor), "Handbook of Microlithography, Micromachining, and Microfabrication", Vol. 2: Micromachining and Microfabrication, SPIE Optical Engineering Press, 1997.
71. Verdú F. V., González R. N., "Thermopneumatic actuator for tactile displays", Proc. 18th Conf. Design of Circuits and Integrated Syst. DCIS 2003, pp. 629–633, 2003.
72. Lee J.S, Lucyszyn S., "A micromachined refreshable braille cell", Journal of Microelectromechanical Systems, Vol. 14, No. 4, pp. 673- 682, 2005.
73. http://robotics.eecs.berkeley.edu/~ronf/tactile.html
74. Moy G., Wagner C., Fearing R.S., "A Compliant Tactile Display for Teletaction", Proc. IEEE Int. Conf. on Robotics and Automation, April 2000. (ICRA '00). Vol. 4. , pp. 3409 – 3415, 2000.
75. Yamamoto A., Nagasawa S., Yamamoto H., Higuchi T., "Electrostatic Tactile Display with Thin Film Slider and Its Application to Tactile Tele-Presentation Systems" , IEEE Trans. on Visualization and Comp. Graph., Vol.12 , No.2 pp. 168 - 177 , 2006.

76. Kajimoto H., Kawakami N., Maeda T., Tachi S., "Tactile Feeling Display using Functional Electrical Stimulation" , Proce. Ninth International Conference on Artificial reality and Telexistence (ICAT'99), 1999.

77. Kajimoto H., Inami M., Kawakami N., Tachi S., "SmartTouch - Augmentation of Skin Sensation with Electrocutaneous Display", Proc. Haptic Symp. 2003, IEEE CS Press, 2003, pp. 40-46, 2003.

78. H. Takahashi, H. Kajimoto, N. Kawakami, S. Tachi, "Electro-Tactile Display with Localized High-Speed Switching", Proc. 12th Int. Conf. on Artificial Reality and Tele-Existence (ICAT2002), Tokyo, Japan, 2002.

79. Vos W.K., Buma D.G., Veltink P.H., "Towards the Optimisation of Spatial Electrocutaneous Display Parameters for Sensory Substitution" , Proc. 7th Annual Conf. of the International Functional Electrical Stimulation Society, Ljubljana, Slovenia, 2002, pp. 332-334.

80. Hayashi K., Takahata M., "Objective Evaluation of Tactile Sensation for Tactile Communication" ,NTT DoCoMo Technical Journal, Vol. 7 No.3, pp.39-43, 2005.

81. Takayuki I.. Hiroyuki S., "Tactile Display Using Acoustic Radiation Pressure Scanning", Trans. of the Virtual Reality Society of Japan, Vol.11, No..1, pp.77-86, 2006.

82. Stone R. J., "Haptic Feedback: A Potted History From Telepresence to Virtual Reality", Proc. Intl. Workshop on Haptic Human-Computer Interaction, pp. 1-7, August 2000.

83. Asamura N., Tomori N., Shinoda H., "A Tactile Feeling Display Based on Selective Stimulation to Skin Receptors", Proc. IEEE VRAIS, pp. 36-42, 1998.

84. Enikov E.T., Lazarov K.V., Gonzales G.R., "Microelectrical Mechanical Systems Actuator Array for Tactile Communication", Proc. Int. Conf. on Computers for Handicapped Persons, pp. 551-558, Austria, 2002.

85. Nara T., Takasaki M., Maeda T., Higuchi T., Ando S., Tachi S., "Surface Acoustic Wave (SAW) Tactile Display Based on Properties of Mechanoreceptors", Virtual Reality Conference, Yokohama Japan, 13-17 March, 2001.

86. Maucher T., Loose M., Meier K., Schemmel J., "The Heidelberg Tactile Vision Substitution System", ISAC, 2000.

87. Konyo M., Todokoro S., "Artificial Tactile Feel Display Using EAP Actuator", Worldwide ElectroActive Polymers, Artificial Muscles, Newsletter, Vol. 2, No. 1, July 2000.

88. Askins S. A., Book W. J., "Digital Clay: User Interaction Model for Control of a Fluidically Actuated Haptics Device", Proc of 1st Int. Conf. on Computational Methods in Fluid Power Technology, November 26-28, Melbourne, Australia, 2003.

89. Dargahi J., Najarian S., and Zheng X.Z., "Measurements and modeling of compliance using a novel multi-sensor endoscopic grasper device", Sensors and Materials, Vol. 17, No. 1, pp. 7-20, 2005.

90. Dargahi J. ,"An Endoscopic and Robotic Tooth-like Compliance and Roughness Tactile Sensor", Journal of Mechanical Design, Vol. 124, No.3, pp.576-582, September 2002.

91. Narayanan N. B., Bonakdar A., Dargahi J., Packirisamy M. and Bhat R., "Design and analysis of a micromachined piezoelectric sensor for measuring the viscoelastic properties of tissues in minimally invasive surgery," Smart Mater. Struct., Vol.15, No. 6, pp.1684–1690 , Dec. 2006

92. Wellman P.S., Howe R.D., " Extracting Features from Tactile maps", Proc. 2nd Inter. Conf. on Medical Image Computing and Computer-Assisted Intervention, pp1133-1142, 1999.

93. Lau C., Wagner C., Howe R.D., "Algorithms for Tactile Rendering in Compliant Environments", Haptics Symposium, pp 32-39, 2004.

94. Wellman P.S., Howe R.D., Dewagan N., Cundari M. A. , Dalton E., Kern K.A, "Tactile Imaging: A Method For Documenting Breast Masses", Proc. First Joint BMES/EMBS Conference, Atlanta, pp. 1131, Oct. 13-16, 1999.

95. Krouskop T.A., Wheeler T.M., Kallel F., Garra B. and Hall T., " The Elastic Moduli of Breast and Prostate Tissue Under Compression", Ultrasonic Imaging, Vol. 20, No 4, pp 260-274, 1998.

96. Sokhanvar S., PhD thesis, Concordia University, June 2007.

97. Sokhanvar S, Packirisamy M, Dargahi J, "A Novel PVDF Based Softness and Pulse Sensor for Minimally Invasive Surgery", The 3rd IEEE International Conference on Sensors, Austria, pp 24-27, 2004.

98. Geiger S.R. ed.," Handbook of Physiology Section 1: The Nervous System", American Physiological Society, 1984.

99. Wellman P.S., Dalton E.P.., Krag D., Kern K. , Howe R.D., "Tactile Imaging of Breast Masses", Arch. Surg. ,Vol. 136, pp204-208, Feb 2001.

100. Sokhanvar S., Dargahi J. and Packirisamy M., "Nonlinear Modelling and Testing of Soft Tissue Embedded Lump for MIS applications", Submitted to the Int. J. of Medical Robotics and Computer Assisted Surgery.

101. DAQ SCB-68, 68-Pin Shielded Connector Block User Manual, National Instruments, December 2002 Ed.

102. Boyd S., Barratt C., Norman S., "Linear Controller Design: Limits of Performance Via Convex Optimization", IEEE Proceedings, Vol.78, No. 3, pp. 529-574, March 1990.

103. Bode H. W., "Network Analysis and Feedback Amplifier Design", New Your, NY: Van Nostrand, 1945.

104. Horwitz I. M., "Synthesis of Feedback Systems", New York, NY: Academic Press, 1963.

105. Horowitz I., " Quantitative feedback theory:, IEE Proc., Vol. 129-D, pp. 215-226, Nov. 1982.

106. MacFarlane A. G. J. and Kouvaritakis B., "A design technique for linear multivariable feedback systems", Int. J. Control, Vol. 25, No. 6, pp. 875-883, 1977.

107. Bryson A. E., Ho Y. C., "Applied Optimal Control", New Your, NY: Hemisphere Publishing Co., 1975.

108. Kwakernaak H., Sivan R., "Linear Optimal Control Systems", New Youk, NY: Wiley, 1972.

109. Athans M., Falb P., "Optimal Control", New York: McGraw-Hill, 1966.

110. Ly U., Bryson A. E., and Cannon R. H., " Design of low-order compensators using parameter optimizatio", in Applications of Nonlinear Programming to Optimization and Control. Laxenburg, Austria: IFAC, 1983.

111. Makila P. M., Toivenen H. T., "Computational methods for parametric LQ minimization: A survey,", IEEE Trans. Aut. Control, vol. AC-32, pp. 658-671, Aug. 1987.

112. Gangsaas D., Bruce K., Blight J., and Ly U., "Application of modern synthesis to aircraft control: three case studies," IEEE Trans. Aut. Control,vol. AC-31, pp. 995-1014, Nov. 1986.

113. Polak E., Mayne D.Q., and Stimler D. M., "Control system design via semi-infinite optimization: A review," Proc. IEEE, Vol. 72, No.12, pp. 1777-1794, Dec. 1984.

114. Polak E., Siegel P., Wuu T., Nye W. T., and Mayne D. Q., "DELIGHT.MIMO: An interactive, optimization-based multivariable control system design package", in Computer-Aided Control Systems Engineering, M. Jamshidi and C. J. Herget, Eds. Amsterdam, The Netherlands: North-Holland, 1985. Reprinted from IEEE Cont. Sys. Mag., No. 4, (Dec. 1982).

115. Fan M. K. H., Wang L., Jonickx J., and Tits A., "Software package for optimization-based design with user-supplied simulators", IEEE Cont. Syst. Mag., Vol. 9, No. 1, pp. 66-71, 1989.

APPENDIX A

SPECIFICATIONS OF THE LINEAER ACTUATOR

Table A.1. The linear actuator specifications.

Specifications	PQ-12
Stroke	20mm
Rated force	6N at15mm/s
Max Power Point	7N at 13 mm/s
Max Speed	27 mm/s
Current draw	250 mA
Input voltage	5 Vdc
Feedback mode	2 kΩ linear potentiometer
Feedback potentiometer linearity	1%
Mass	75 g
Operating temperature	-10 to +50 °C
Actuator lifetime	100,000 cycles

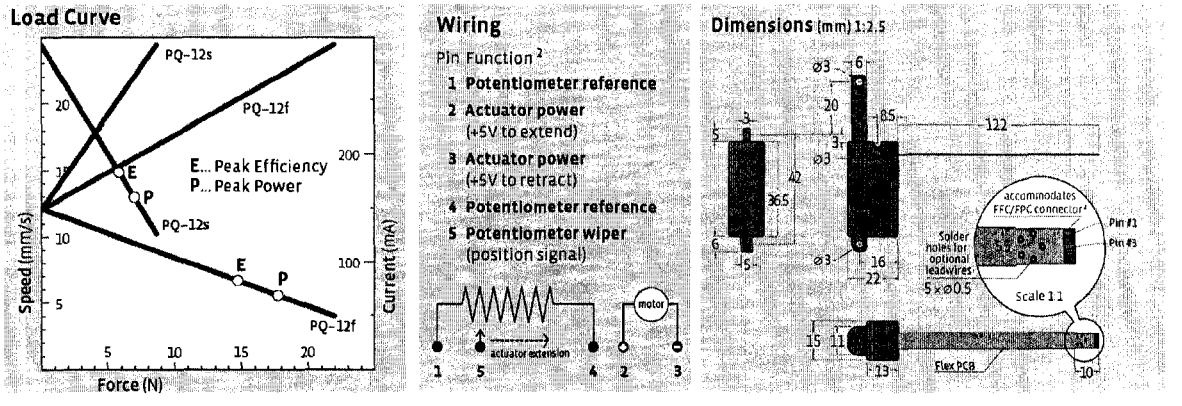

Figure A.1. The dimensions, load curve, and the electrical diagram of the actuator.

APPENDIX B

FORCE SENSITIVE RESISTOR

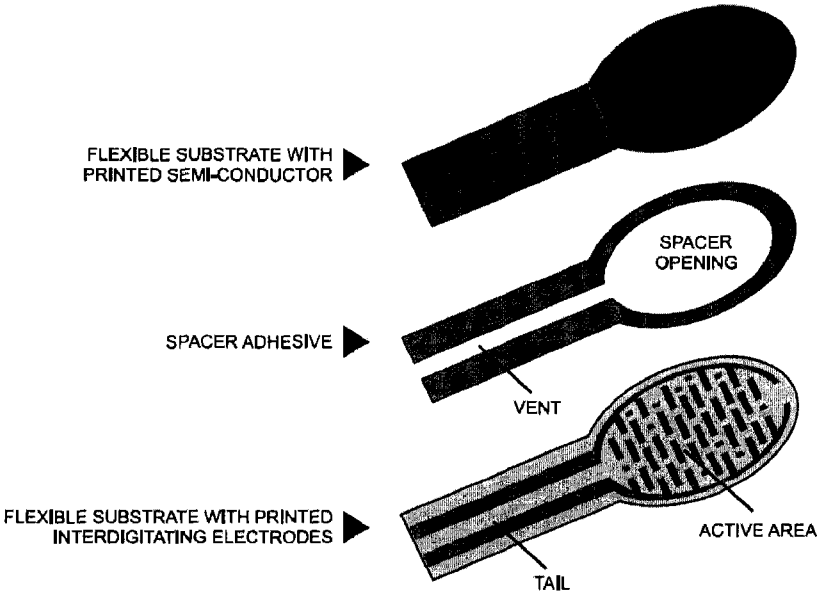

Figure B.1. The structure of the sensor and its different components

The force vs. resistance characteristic shown in Figure B.2 provides an overview of FSR typical response behavior. For interpretational convenience, the force vs. resistance data is plotted on a log/log format. These data are representative of a typical device, with this particular force-resistance characteristic being the response of evaluation part (0.5" [12.7 mm] diameter circular active area). In general, FSR response approximately follows an inverse power-law characteristic (roughly 1/R). Referring to Figure B.2, at the low force end of the force-resistance characteristic, a switch like response is evident. This turn-on threshold, or 'break force", that swings the resistance from greater than 100 kΩ to about 10 kΩ (the beginning of the dynamic range that follows a power-law) is determined by the substrate and overlay thickness and flexibility,

size and shape of the actuator, and spacer-adhesive thickness (the gap between the facing conductive elements).

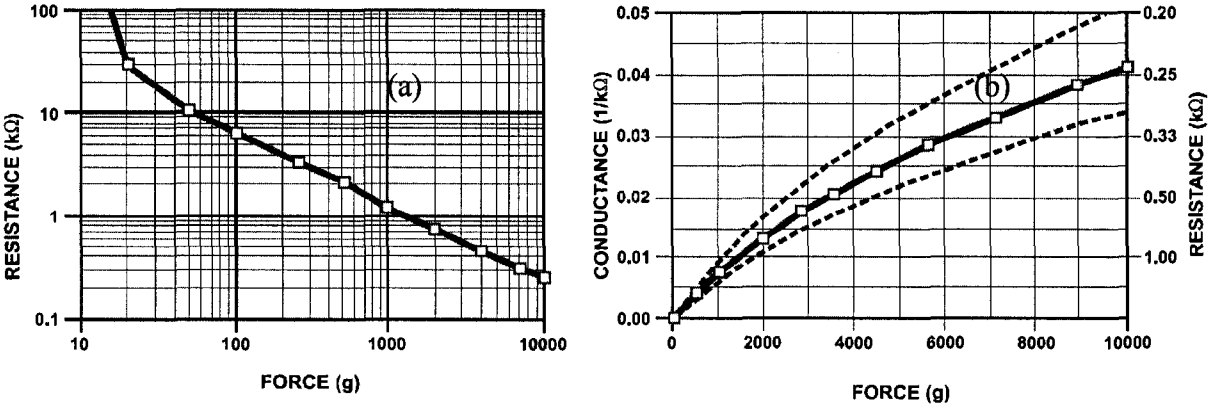

Figure B.2 . The force-resistance curve for FSR

At the high force end of the dynamic range, the response deviates from the power-law behavior, and eventually saturates to a point where increases in force yield little or no decrease in resistance. Under these conditions of Figure B.2, this saturation force is beyond 10 kg.

APPENDIX C

IDENTIFYING A SYSTEM FROM THE BODE PLOT

The general form of a second order system is:

$$G(s) = \frac{k\omega_n^2}{s^2 + 2\zeta\omega_n s + \omega_n^2}$$

DC GAIN - The DC Gain of a system can be calculated from the magnitude of the bode plot when s=0.

$$\text{DC Gain} = 10^{M(0)/20}$$

NATURAL FREQUENCY - The natural frequency of a second order system occurs when the phase of the response is -90 degrees relative to the phase of the input.

$$\omega_n = \omega_{-90^\circ}$$

where ω_{-90° is the frequency at which the phase plot is at -90 degrees.

DAMPING RATIO - The damping ratio of a system can be found with the DC Gain and the magnitude of the bode plot when the phase plot is -90 degrees.

$$\zeta = K / (2 * 10^{(M_{-90^\circ}/20)})$$

APPENDIX D

MATLAB CODE FOR PID OPTIMIZATION

```
function [Kp,Ki,Kd] = runm  %runtracklsq
% RUNTRACKLSQ demonstrates using LSQNONLIN with Simulink.
runm  %model1 %optsim                    % Load the model
pid0 = [0.91 0.105 0.1]; % Set initial values
a1 = 21.3; a2 = 1;          % Initialize plant variables in model
options = optimset('LargeScale','off','Display','iter',...
    'TolX',0.001,'TolFun',0.001);
pid = lsqnonlin(@tracklsq, pid0, [], [], options);
Kp = pid(1); Ki = pid(2); Kd = pid(3);
   function F = tracklsq(pid)
    % Track the output of optsim to a signal of 1
    % Variables a1 and a2 are needed by the model optsim.
    % They are shared with RUNTRACKLSQ so do not need to be
    % redefined here.
    Kp = pid(1);
    Ki = pid(2);
    Kd = pid(3);
    % Compute function value
    simopt = simset('solver','ode14x','SrcWorkspace','Current');
    % Initialize sim options
    [tout,xout,yout] = sim('runm',[0 10],simopt);
    F = yout-1;
```

```
   end
 Kp = pid(1)
Ki = pid(2)
Kd = pid(3)
%model1
end
```